Effective Operators and Long-Range Forces for Dark Matter

ROSTAGNI, GUILLAUME

Effective Operators and Long-Range Forces for Dark Matter

Guillaume Rostagni

A Thesis presented for the degree of
Doctor of Philosophy

Institute for Particle Physics Phenomenology
Department of Physics
Durham University
United Kingdom

May 2024

Effective Operators and Long-Range Forces for Dark Matter

Guillaume Rostagni

Submitted for the degree of Doctor of Philosophy

May 2024

Abstract: As successful as the Standard Model has proven to be, many unknowns cloud our understanding of the Universe; in particular, the nature of as much as 80% of matter remains mysterious, and the search for dark matter (DM) is one of the main areas of research in particle physics. In this thesis, we consider two approaches to help solve the DM problem. First, we consider axion-like particles and show how the addition of shift symmetry-breaking operators affects the phenomenology of the QCD axion. In particular, we show that potentials resulting from the exchange of a pair of virtual axions acquire a different scaling as we include some higher-order operators. We demonstrate how this result affects the sensitivity of searches for new long-range forces. Later, we study a shift-symmetry preserving, Z_2 invariant dimension-6 interaction term between an axion and the Higgs field. We compare constraints from Higgs-boson and meson decays, bounds from atomic spectroscopy searching for fifth forces, and astrophysical observables. In the other approach, we study the Stodolsky effect, a spin-dependent shift in the energy of a fermion sitting in a bath of neutrinos. We generalise this effect to DM candidates and give expressions for the induced energy shifts, considering all effective operators up to dimension-6. We consider two experimental setups, a torsion balance and a SQUID magnetometer, to place constraints on the parameter space for these candidates.

Contents

List of Figures

List of Tables

List of Abbreviations

1PI	One-Particle Irreducible
ABJ	Adler-Bell-Jackiw
ALP	Axion-Like Particle
BAO	Baryon Acoustic Oscillations
BBN	Big Bang Nucleosynthesis
BSM	Beyond the Standard Model
CKM	Cabbibo-Kobayashi-Maskawa
CL	Confidence level
CMB	Cosmic Microwave Background
CoM	Centre of Mass
CP	Charge-Parity
CνB	Cosmic Neutrino Background
DFSZ	Dine-Fischler-Srednicki-Zhitnitsky
DM	Dark Matter
d.o.f.	Degree of freedom
DSE	Dark Stodolsky Effect

EDM Electric Dipole Moment

EFT Effective Field Theory

EWSB Electroweak Symmetry Breaking

FI Freeze-In

FO Freeze-Out

FT Fourier Transform

GR General Relativity

IP Interaction Potential

KSVZ Kim-Shifman-Vainshtein-Zakharov

LHC Large Hadron Collider

MOND Modified Newtonian Dynamics

NLO Next-to-Leading Order

NR Non-Relativistic

OPE One-Pion Exchange

PMNS Pontecorvo-Maki-Nakagawa-Sakata

PNGB Pseudo Nambu-Goldstone Boson

PQ Peccei-Quinn

PV Passarino-Veltman

QCD Quantum Chromodynamics

QFT Quantum Field Theory

RGE Renormalisation Group Equation

RS Rarita-Schwinger

SM Standard Model

SQUID Superconducting Quantum Interference Device

SUSY Supersymmetry

UV Ultraviolet

VEV Vacuum Expectation Value

VM Vacuum Misalignment

WIMP Weakly-Interacting Massive Particle

ΛCDM Lambda-Cold Dark Matter

νSE Neutrino Stodolsky Effect

χPT Chiral Perturbation Theory

Declaration

The work in this thesis is based on research carried out in the Department of Physics at Durham University. No part of this thesis has been submitted elsewhere for any degree or qualification.

Research presented in this thesis is based on joint work:

- Chapter 3 is based on [1]: Martin Bauer and Guillaume Rostagni, *Fifth forces from QCD axions scale differently*, Physical Review Letters **132** (2024) 101802.
- Chapter 4 is based on [2]: Martin Bauer, Guillaume Rostagni, and Jonas Spinner, *The Axion-Higgs Portal*, Physical Review D **107** (2023) 015007.
- Chapter 5 is based on [3]: Guillaume Rostagni and Jack Shergold, *The dark Stodolsky effect: constraining effective dark matter operators with spin-dependent interactions*, Journal of Cosmology and Astroparticle Physics **07** (2023) 018.

Acknowledgements

First, I would like to thank my supervisor, Martin Bauer, who has helped me and supported me throughout my PhD. I would also like to mention the people I have worked with here in Durham, Martin of course, but also Jack S., Jonas, and Sreemanti.

My time at the IPPP has been memorable and I would like to thank all the people that made it a great place to be for four years. First and foremost, Joanne and Trudy, who make sure everything always runs smoothly here; then all the PhDs, postdocs, and visitors for the ever-riveting lunch conversations and for honouring the perennial tradition of pub-food-pub. Special mentions go to the members of Café 215 for being supportive at all times: Edwin, Henry, Jack F., James, Mălina, Mia, Peter, the people who were here for a few weeks and that I have forgotten (sorry), and of course our favourite squatter, Tommy. I am also grateful to Ansh, Jack F., Martin, and Sofie who have kindly agreed to proofread sections of this thesis.

I would also like to thank Jack and Tommy for the many laughs, hours of televised entertainment, endless moaning about the bus and the weather, and the hearing loss.

Pour finir, je souhaite remercier du fond du cœur toute ma famille, qui m'a toujours encouragé et soutenu, particulièrement dans les moments plus difficiles. Merci à maman, papa, et Caroline de toujours me faire sourire quand je rentre à la maison.

Altissimum regionis huius montem, hodierno die, sola videndi insignem loci altitudinem cupiditate ductus, ascendi.

— from *Epistolae Familiares* by Francesco Petrarca

Chapter 1

Introduction

When, in 2012, the Higgs boson was discovered at CERN, it closed a chapter in particle physics: the Standard Model of particle physics, our best description of the infinitely small, and the most precise theory ever written, was finally completed. Far from the end of the story, this discovery was meant to open up the next chapter, in which the next batch of particles that would fill in the many cracks that had appeared in this theory were just around the corner. And then nothing. The great particle colliders that had cemented the Standard Model refused to reveal anything beyond. From this crisis was reinforced the idea that the answer might be found, not deep underneath the French-Swiss border, but at ground level, in more modest laboratories, or higher, in the sky.

In truth, we did not wait for everyone to give up on SUSY to look elsewhere (nor did we abandon particle accelerators). From the electron and cosmic rays, to the muon's magnetic moment and gravitational waves, dozens of crucial discoveries have been made without the need to crash particles together with ever-increasing energies, and today, hopes of discovering physics beyond the Standard Model rely on a vast breadth of experiments. We will concern ourselves with a small subset of these which aim to measure low-energy observables, measurable on a tabletop experiment, with great precision. Long-range forces result from the exchange of virtual particles and manifest as a potential whose effect can theoretically be measured. Alternat-

ively, spin-dependent effects can cause precessions of the spins in a material, again measurable, as a torque or magnetisation of the material.

The focus of this thesis will be understanding how to use these experiments to place bounds on the parameter space new theories are allowed to stand in. In order to remain general, we will use an effective theory approach in which we will not make a choice for the underlying theory, but rather consider any effect it can have at the scale of the experiment. We will further contrast two approaches. In one, we consider a complete effective theory of a type of particle (axions), defined just below some symmetry breaking scale, and in the other we look at a basis of individual operators for a range of undetermined new particles as dark matter candidates.

The structure of this thesis is as follows. In Chapter 2 we will introduce some of the theoretical concepts we will use in later chapters. Specifically, we will give a short introduction to renormalisation in Quantum Field Theory (QFT), before moving on to a brief review of the contents of the Standard Model (SM); we will then give evidence for the existence of dark matter, and finally introduce the axion as a solution to the strong CP problem before generalising towards axion-like particles as dark matter candidates. In Chapter 3, we will develop a method to calculate long-range, non-relativistic interaction potentials, caused by the exchange of virtual particles; these so-called fifth forces will then be used to place phenomenological constraints on axion-like particles. Still within the context of these particles, we will spend some time in Chapter 4 on the properties of a particular dimension-6 operator describing an interaction between the SM Higgs boson and a scalar particle, preserving the Z_2 and shift symmetries of the latter. Later, in Chapter 5, we will introduce an analogue to the Stodolsky effect, proposed to detect the cosmic neutrino background, for dark matter, and develop a basis of effective dark matter operators to study this effect systematically. Finally, we will be concluding this thesis in Chapter 6.

Chapter 2

Background

Before diving into the content of this thesis, we need to introduce some concepts that will be useful for later discussion. This work assumes that the reader is familiar with group theory and quantum field theory, and concepts from these topics are not necessarily mentioned and used with detailed derivations from first principles. Most of this background information can be found in standard QFT textbooks such as [4, 5]. Natural units $\hbar = c = 1$ are used throughout this thesis. Unless specified otherwise, numerical values used in this work are taken from [6].

We will first introduce the concept of renormalisation and running couplings in Section 2.1, using scalar ϕ^4 theory in four dimensions as a toy model. Then, in Section 2.2, we give a brief review of the field content of the Standard Model, including the Higgs mechanism and SM beta functions. Despite its successes, we will argue that its shortcomings justify the dark matter hypothesis and give a short overview of the main production and detection methods in Section 2.3. Finally, in Section 2.4, we will introduce the QCD axion via the strong CP problem, move on to extend the definition of the axion to include axion-like particles as popular dark matter candidates, and give the formulation of a generic axion effective Lagrangian and its evolution across different energy scales.

2.1 Renormalisation

2.1.1 ϕ^4 Theory at Tree-level

We begin by introducing the concepts of renormalisation and running couplings appearing in many QFTs using a simpler theory. In fact, one of the simplest interacting theory one can write is the "ϕ^4 theory" describing a real scalar field ϕ of mass m with quartic self-interactions with strength λ, and a Lagrangian

$$\mathcal{L}_{\phi^4} = \frac{1}{2}(\partial_\mu \phi)(\partial^\mu \phi) - \frac{1}{2}m^2\phi^2 - \frac{\lambda}{4!}\phi^4 \,. \tag{2.1.1}$$

In this theory, interaction processes can be mathematically described by scattering amplitudes, written down as overlaps between an initial state i and a final state f,

$$\langle f|S|i\rangle \,, \tag{2.1.2}$$

where we call S the scattering matrix encoding all the interactions in the theory. In a free theory, there are no interactions and so S is simply the identity matrix $\mathbb{1}$. Bearing this in mind, in perturbation theory we write all interactions as a small perturbation away from the free theory and decompose the S-matrix as

$$S = \mathbb{1} + iT \,, \tag{2.1.3}$$

where we call T the transfer matrix. Explicitly enforcing momentum conservation, we finally define

$$\langle f|T|i\rangle = (2\pi)^4 \delta^{(4)} \left(\sum_i p_i - \sum_f p_f \right) \mathcal{M} \,, \tag{2.1.4}$$

where the sums run over all incoming and outgoing momenta p_i and p_f respectively. The quantity $\mathcal{M}$ contains the non-trivial interactions of the theory and is what we will focus our efforts on calculating. From now on, we will simply refer to $\mathcal{M}$ as the "matrix element".

Computing the matrix element can be done diagrammatically through the use of the so-called Feynman rules, themselves directly derived from the Lagrangian. The

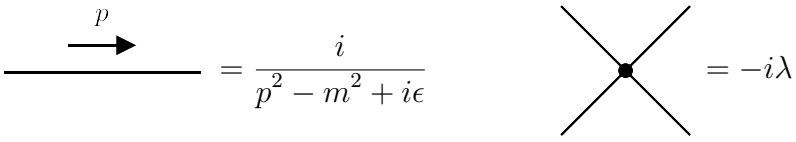

Figure 2.1: Momentum-space Feynman rules for the ϕ^4 theory.

matrix element for a process is given by writing down and summing over all possible diagrams describing this process. In our ϕ^4 theory, we assign to each element of a diagram the factors given in Figure 2.1[1]. Taking for example a $\phi\phi \to \phi\phi$ scattering process, at leading order in λ, the matrix element is simply

$$i\mathcal{M}\left(\phi(p_1)\phi(p_2) \to \phi(p_3)\phi(p_4)\right) = -i\lambda + O(\lambda^2)\,. \tag{2.1.5}$$

The matrix element $\mathcal{M}$ is not actually a physical quantity, the quantities we measure are the decay width $\mathrm{d}\Gamma$ for particle decays and differential cross-section $\mathrm{d}\sigma$ for scattering processes, both of which involve the squared matrix element $|\mathcal{M}|^2$. For non-scalar external states, we note that we also need to average over all initial and sum over all final state spins and polarisations. In the Centre of Mass (CoM) frame, for a $1 \to n$ decay and $2 \to n$ scattering, these will respectively take the forms

$$\mathrm{d}\Gamma = \frac{1}{2m_1}|\mathcal{M}|^2\mathrm{d}\Phi_n \quad \text{and} \quad \mathrm{d}\sigma = \frac{1}{4\sqrt{(p_1\cdot p_2)^2 - m_1^2 m_2^2}}|\mathcal{M}|^2\mathrm{d}\Phi_n\,, \tag{2.1.6}$$

where n is the number of particles in the final state, and we write the n particle Lorentz-invariant phase space

$$\mathrm{d}\Phi_n = (2\pi)^4\delta^{(4)}\left(\sum_i p_i - \sum_f p_f\right)\prod_{f=1}^{n}\frac{\mathrm{d}^3\boldsymbol{p}_f}{(2\pi)^3 2E_f}\,, \tag{2.1.7}$$

where the sum in the delta function runs over all incoming and outgoing momenta, and the product is only taken over all n *outgoing* momenta. For 2-body processes, the phase space is

$$\mathrm{d}\Phi_2 = (2\pi)^4\delta^{(4)}\left(W - p_3 - p_4\right)\frac{\mathrm{d}^3\boldsymbol{p}_3}{(2\pi)^3 2E_3}\frac{\mathrm{d}^3\boldsymbol{p}_4}{(2\pi)^3 2E_4}\,, \tag{2.1.8}$$

[1] All Feynman diagrams in this work were drawn using the FeynGame tool [7, 8]

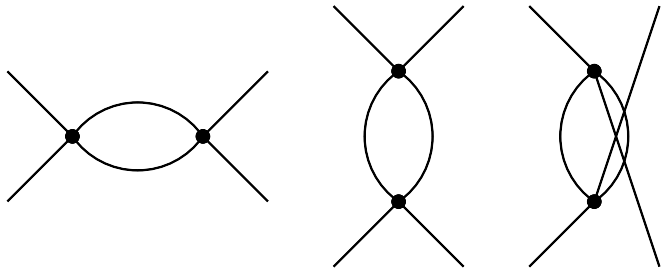

Figure 2.2: Diagrams contributing to the 1-loop corrections to the quartic vertex in ϕ^4 theory.

where we have defined $W \equiv p_1 + p_2$. In the CoM frame, we can write $W = (\sqrt{s}, \mathbf{0})$ and use the delta function to perform the integral over $\boldsymbol{p}_4$,

$$\mathrm{d}\Phi_2 = \frac{\pi}{2}\delta\left(\sqrt{s} - E_3 - E_4\right)\frac{1}{E_3 E_4}\frac{\mathrm{d}^3\boldsymbol{p}_f}{(2\pi)^3} \tag{2.1.9}$$

with $E_3 = \sqrt{m_3^2 + |\boldsymbol{p}_f|^2}$ and $E_4 = \sqrt{m_4^2 + |\boldsymbol{p}_f|^2}$. Finally, we can use the remaining delta function, and the identity

$$\delta\left[f(x)\right] = \sum_{x_i}\frac{\delta(x - x_i)}{\left|f'(x_i)\right|} \quad \text{for} \quad f(x_i) = 0\,, \tag{2.1.10}$$

to perform the $|\boldsymbol{p}_f|$ integral,

$$\mathrm{d}\Phi_2 = \frac{1}{8\pi}\frac{\sqrt{s - (m_3 + m_4)^2}\sqrt{s - (m_3 - m_4)^2}}{s}\frac{\mathrm{d}\Omega}{4\pi}\,. \tag{2.1.11}$$

Plugging this back into (2.1.6), we end up with the formula for the differential cross-section for a $2 \to 2$ process in the CoM frame,

$$\left.\frac{\mathrm{d}\sigma}{\mathrm{d}\Omega}\right|_{\mathrm{CoM}} = \frac{1}{64\pi^2}\frac{1}{s}\frac{\sqrt{s - (m_3 + m_4)^2}\sqrt{s - (m_3 - m_4)^2}}{\sqrt{s - (m_1 + m_2)^2}\sqrt{s - (m_1 - m_2)^2}}|\mathcal{M}|^2\,. \tag{2.1.12}$$

A similar, albeit more complex derivation can be used for the three-body phase space, the results of which can be found in [6].

2.1.2 Loop Integrals and UV Divergences

To compute higher-order corrections in λ, we need to include more complex diagrams involving loops. To deal with undetermined loop momenta k, we have to integrate

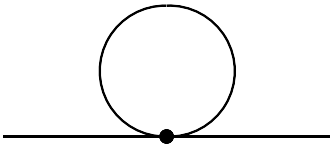

Figure 2.3: 1-loop self-energy diagram in ϕ^4 theory.

them over all possible values by including a factor $\int \frac{\mathrm{d}^4k}{(2\pi)^4}$. For example, 1-loop corrections to the four point vertex are given by the diagrams shown in Figure 2.2, the first of which gives an amplitude

$$i\mathcal{M}_{\text{1-loop},s} = \lambda^2 \int \frac{\mathrm{d}^4k}{(2\pi)^4} \frac{1}{k^2 - m^2 + i\epsilon} \frac{1}{(k + p_1 + p_2)^2 - m^2 + i\epsilon} \,. \tag{2.1.13}$$

The loop integral can be evaluated using the Feynman parameterisation technique [5, 9], which transforms it into an integral of the form

$$I_2 \equiv \lambda^2 \int \frac{\mathrm{d}^4k'}{(2\pi)^4} \frac{1}{[k'^2 - \Delta^2]^2} \longrightarrow \infty \,, \tag{2.1.14}$$

where Δ is a function of m, p_1 and p_2. This integral diverges as we integrate k' to infinity, and our first-order correction appears to create an infinitely strong interaction, which is obviously problematic. To regularise this divergence, we change the integration from 4-dimensions to $d = 4 - 2\epsilon$ dimensions[2], and take the $\epsilon \to 0$ limit to recover a result in 4-dimensions. In d-dimensions, the coupling constant λ has mass dimension $4 - d$, and so we define an explicitly dimensionless coupling constant $\bar{\lambda} \equiv \mu^{d-4}\lambda = \mu^{-2\epsilon}\lambda$ where μ is some arbitrary mass scale. It can be shown that the scalar integral I_2 is now equal to

$$I_2 \equiv \mu^{4\epsilon}\bar{\lambda}^2 \int \frac{\mathrm{d}^dk'}{(2\pi)^d} \frac{1}{[k'^2 - \Delta^2]^2} = \mu^{4\epsilon} \frac{i\bar{\lambda}^2}{(4\pi)^2} (4\pi)^\epsilon \left(\Delta^2\right)^{-\epsilon} \Gamma(\epsilon) \,. \tag{2.1.15}$$

The offending part comes from the $\Gamma(\epsilon)$ term which diverges as ϵ goes to zero (i.e. $d \to 4$). We expand I_2 in powers of ϵ to obtain

$$I_2 = \frac{i\mu^{2\epsilon}\bar{\lambda}^2}{16\pi^2} \left(\frac{1}{\epsilon} + \text{finite}\right) \,. \tag{2.1.16}$$

[2]This ϵ is not to be confused with the ϵ appearing in propagators. To simplify notation, the latter will be omitted from now on.

As it turns out, this problem also appears when considering corrections to the scalar propagator, drawn as the "self-energy" diagram shown in Figure 2.3, which translates as an infinitely large mass m for the scalar field. We call these types of divergences, *Ultraviolet (UV) divergences*. We note that another type of divergences appears when considering massless external states, these are known as *infrared divergences* but are not relevant for this work, and so will not be mentioned further.

2.1.3 Counterterms and Running Couplings

To solve this problem of infinite quantities appearing in calculations, we start by redefining all the fields and parameters appearing in (2.1.1) to explicitly separate the UV divergent parts from the finite parts. Relabelling the quantities appearing in (2.1.1) as *bare* parameters $\{\phi_B, m_B, \lambda_B\}$, we define the *renormalised* parameters $\{\phi_R, m_R, \lambda_R\}$ such that

$$\phi_B = \sqrt{Z_\phi}\phi_R\,, \qquad m_B = \sqrt{Z_m}m_R\,, \qquad \lambda_B = Z_\lambda \lambda_R\,, \tag{2.1.17}$$

where the Z_i are the renormalisation factors. The Lagrangian can then be written in terms of these renormalised quantities,

$$\mathcal{L}_{\phi^4} = \frac{1}{2}Z_\phi(\partial_\mu\phi_R)(\partial^\mu\phi_R) - \frac{1}{2}Z_\phi Z_m m_R^2\phi_R^2 - Z_\phi^2 Z_\lambda \frac{\lambda_R}{4!}\phi_R^4\,, \tag{2.1.18}$$

or alternatively,

$$\mathcal{L}_{\phi^4} = \frac{1}{2}\left(1+\delta_\phi\right)(\partial_\mu\phi_R)(\partial^\mu\phi_R) - \frac{1}{2}\left(1+\delta_m\right)m_R^2\phi_R^2 - \left(1+\delta_\lambda\right)\frac{\lambda_R}{4!}\phi_R^4\,, \tag{2.1.19}$$

where we have defined $\delta_\phi = Z_\phi - 1$, $\delta_m = Z_\phi Z_m - 1$, and $\delta_\lambda = Z_\phi^2 Z_\lambda - 1$, to explicitly show extra terms containing the renormalisation factors appearing in the Lagrangian separately. We call these counterterms, and we want to set the δ_i such that these counterterms exactly cancel out the UV divergences appearing in higher-order corrections; *i.e.* at 1-loop, a tree-level counterterm must cancel all 1-loop UV divergences.

We start by studying the effect of higher-order corrections on the scalar propagator $D(p)$. At leading order, this is simply $D(p) = D^0(p) = \frac{i}{p^2 - m^2}$, and corrections give

$D(p) =$ 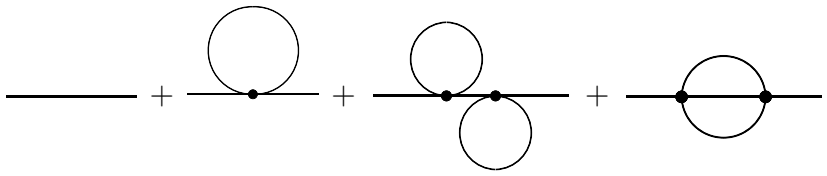 (2.1.20)

Grouping non-separable higher-order diagrams as One-Particle Irreducible (1PI) , such that all 1PI diagrams cannot be separated by cutting a single line, i.e. the second and fourth diagrams above are 1PI, and defining the sum of all 1PI diagrams as $i\Sigma$, we rewrite the propagator as

$D(p) =$ 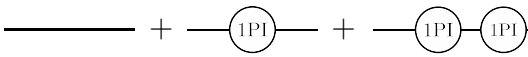

$$\begin{aligned} &= D^0(p) + D^0(p)(i\Sigma)D^0(p) + D^0(p)(i\Sigma)D^0(p)(i\Sigma)D^0(p) + ... \\ &= D^0(p)\left[\sum_{n=0}^{\infty}\left(i\Sigma D^0(p)\right)^n\right]. \end{aligned} \tag{2.1.21}$$

The term in brackets is known as a Dyson series, and for an expansion parameter sufficiently small, it converges to $\left(1 - i\Sigma D^0(p)\right)^{-1}$ and we can write

$$(D(p))^{-1} = \left(D^0(p)\right)^{-1}\left(1 - i\Sigma D^0(p)\right) = -i\left(p^2 - m^2 + \Sigma\right). \tag{2.1.22}$$

At 1-loop order, the only 1PI diagram contributing to Σ is the self-energy diagram shown in Figure 2.3, and we have

$$\begin{aligned} i\Sigma &= -i\mu^{2\epsilon}\bar{\lambda}\int\frac{\mathrm{d}^d k}{(2\pi)^d}\frac{i}{k^2 - m^2} \\ &= i\frac{\bar{\lambda}m^2}{16\pi^2}\left[\frac{1}{\epsilon} + 1 + \log 4\pi - \gamma_E + \log\frac{\mu^2}{m^2}\right], \end{aligned} \tag{2.1.23}$$

where γ_E is the Euler-Mascheroni constant. Plugging this into the propagator (2.1.22) and expressing the result in terms of renormalised quantities gives

$$i\left(D(p)\right)^{-1} = \left(1 + \delta_\phi\right)p^2 - \left(1 + \delta_m\right)m_R^2 + \frac{\bar{\lambda}_R m_R^2}{16\pi^2}\left[\frac{1}{\epsilon} + 1 + \log 4\pi - \gamma_E + \log\frac{\mu^2}{m_R^2}\right], \tag{2.1.24}$$

where to cancel out divergences we require

$$\delta_\phi = 0\,, \quad \text{and} \quad \delta_m = \frac{\bar{\lambda}_R}{16\pi^2}\frac{1}{\epsilon} + \text{finite}\,. \tag{2.1.25}$$

The finite part of δ_m can be chosen as desired and defines the renormalisation scheme. Two common choices are the minimal subtraction (MS) scheme where we set the finite part to 0, and the modified MS ($\overline{\text{MS}}$) scheme where we absorb the $(\log 4\pi - \gamma_E)$ term into δ_m. In $\overline{\text{MS}}$ then, the bare and renormalised masses are related by

$$m_R = \frac{1}{\sqrt{Z_\phi Z_m}} m_B = m_B\left[1 - \frac{\bar{\lambda}_R}{32\pi^2}\left(\frac{1}{\epsilon} + \log 4\pi - \gamma_E\right) + O\left(\bar{\lambda}_R^2\right)\right]\,. \tag{2.1.26}$$

As a result of this choice, the higher-order corrections to the renormalised mass m_R are now scheme-dependent.

We note that while we found $\delta_\phi = 0$ which implies that the bare field is identical to the renormalised field in ϕ^4 theory, this is not true in general, and the fields of the theory need to be renormalised as well.

We can treat the 1-loop corrections to the quartic coupling λ similarly. Up to one-loop, the four point vertex function is found by calculating the diagrams in Figure 2.2 and gives

$$-i\left(1 + \delta_\lambda\right)\lambda_R + 3\frac{i\lambda_R\bar{\lambda}_R}{16\pi^2}\left(\frac{1}{\epsilon} + \text{finite}\right)\,. \tag{2.1.27}$$

To cancel out divergences we require

$$\delta_\lambda = \frac{3\bar{\lambda}_R}{16\pi^2}\frac{1}{\epsilon} + \text{finite}\,. \tag{2.1.28}$$

An unintended consequence of renormalising our Lagrangian is that we have introduced dependencies on the renormalisation scale μ in our renormalised quantities, explicitly through the $\mu^{-2\epsilon}$ factor appearing in the definition of $\bar{\lambda}_R$, and implicitly through the presence of $\bar{\lambda}_R$ in the counterterms (2.1.25) and (2.1.28). In fact, since the bare quantities in the Lagrangian must be scale invariant, these dependencies of the physical renormalised quantities on the scale μ remain and must be taken into account when calculating observables. To see this, let us consider the bare quartic

coupling λ_B; we must have

$$0 \overset{!}{=} \frac{\mathrm{d}}{\mathrm{dlog}\,\mu}\lambda_B = \frac{\mathrm{d}}{\mathrm{dlog}\,\mu}\left(\mu^{2\epsilon}Z_\lambda\bar{\lambda}_R\right) = \mu^{2\epsilon}Z_\lambda\bar{\lambda}_R\left(2\epsilon + \frac{1}{Z_\lambda}\frac{\mathrm{d}Z_\lambda}{\mathrm{dlog}\,\mu} + \frac{1}{\bar{\lambda}_R}\frac{\mathrm{d}\bar{\lambda}_R}{\mathrm{dlog}\,\mu}\right). \tag{2.1.29}$$

At leading order in $\bar{\lambda}_R$, we have then $\frac{\mathrm{d}}{\mathrm{dlog}\,\mu}\bar{\lambda}_R = -2\epsilon\bar{\lambda}_R$, and at next-to-leading order,

$$\beta(\bar{\lambda}_R) \equiv \frac{\mathrm{d}}{\mathrm{dlog}\,\mu}\bar{\lambda}_R = -2\epsilon\bar{\lambda}_R + \frac{3\bar{\lambda}_R^2}{8\pi^2} + O\left(\bar{\lambda}_R^3\right), \tag{2.1.30}$$

where we have defined the 1-loop beta function $\beta(\bar{\lambda}_R)$ which describes the evolution of the coupling constant with respect to the mass scale μ.[3] Therefore, the physical coupling constant that we measure will change depending on the mass scale considered.

We can do a similar calculation with the renormalised field ϕ_R and mass m_R, which will also depend on the scale μ through $\bar{\lambda}_R$. We write

$$0 \overset{!}{=} \frac{\mathrm{d}}{\mathrm{dlog}\,\mu}\phi_B = \frac{\mathrm{d}}{\mathrm{dlog}\,\mu}\left(\sqrt{Z_\phi}\phi_R\right) = \sqrt{Z_\phi}\phi_R\left(\frac{1}{2Z_\phi}\frac{\mathrm{d}Z_\phi}{\mathrm{dlog}\,\mu} + \frac{1}{\phi_R}\frac{\mathrm{d}\phi_R}{\mathrm{dlog}\,\mu}\right), \tag{2.1.31a}$$

$$0 \overset{!}{=} \frac{\mathrm{d}}{\mathrm{dlog}\,\mu}m_B^2 = \frac{\mathrm{d}}{\mathrm{dlog}\,\mu}\left(Z_m m_R^2\right) = Z_m m_R^2\left(\frac{1}{Z_m}\frac{\mathrm{d}Z_m}{\mathrm{dlog}\,\mu} + \frac{1}{m_R^2}\frac{\mathrm{d}m_R^2}{\mathrm{dlog}\,\mu}\right), \tag{2.1.31b}$$

and further define the anomalous dimension $\gamma_\phi(\bar{\lambda}_R)$ and anomalous mass dimension $\gamma_m(\bar{\lambda}_R)$,

$$\gamma_\phi(\bar{\lambda}_R) \equiv \frac{1}{\phi_R}\frac{\mathrm{d}}{\mathrm{dlog}\,\mu}\phi_R = O\left(\bar{\lambda}_R^2\right), \tag{2.1.32a}$$

$$\gamma_m(\bar{\lambda}_R) \equiv \frac{1}{m_R^2}\frac{\mathrm{d}}{\mathrm{dlog}\,\mu}m_R^2 = \frac{\bar{\lambda}_R}{8\pi^2} + O\left(\bar{\lambda}_R^2\right). \tag{2.1.32b}$$

Together, the beta function (2.1.30) and anomalous dimensions (2.1.32) form the Renormalisation Group Equations (RGEs). They can be solved to determine the evolution, or running, of the parameters of a model with respect to a reference scale μ_0. For example, the beta function (2.1.30) gives

$$\bar{\lambda}_R(\mu) = \frac{\bar{\lambda}_0}{1 - \frac{3\bar{\lambda}_0}{8\pi^2}\log\frac{\mu}{\mu_0}}, \tag{2.1.33}$$

[3] Several conventions exist for defining $\beta(\lambda)$, notably $\beta(\lambda) = \mu^2\,\mathrm{d}\lambda/\mathrm{d}\mu^2$ which is related to the one we use by a factor 1/2.

with $\bar{\lambda}_0 = \bar{\lambda}_R(\mu_0)$, which allows us to obtain the value of the coupling at any scale given we know its value at the scale μ_0. This will be useful later when we define a model at a high UV scale and want to calculate the parameters of this model relevant in lower energy experiments.

2.2 The Standard Model

Somewhat stepping up from the simple ϕ^4 theory, we now take a look at the Standard Model. The SM is a QFT with the gauge symmetry group $\mathrm{SU}(3)_c \times \mathrm{SU}(2)_L \times \mathrm{U}(1)_Y$, respectively corresponding to the Quantum Chromodynamics (QCD), weak and hypercharge groups, and with the particle content described in Figure 2.4. Its Lagrangian can be written as [5, 6, 10]

$$\mathcal{L}_{\mathrm{SM}} = \mathcal{L}_{\mathrm{gauge}} + \mathcal{L}_{\mathrm{fermion}} + \mathcal{L}_{\mathrm{Higgs}} + \mathcal{L}_{\mathrm{Yukawa}} \tag{2.2.1}$$

where the four terms respectively describe the gauge fields corresponding to the symmetries, the fermionic content, dynamics of the Higgs scalar field, and the Yukawa interactions generating masses for the fermion fields.

We omit the gauge fixing and ghost Lagrangian terms, as they are not relevant for the content of this work. For a full discussion of these concepts, see for example [5].

2.2.1 The Gauge Lagrangian

The first ingredient is the gauge Lagrangian describing the gauge fields associated with each of the three symmetry groups of the SM. For a non-Abelian $\mathrm{SU}(N)$ group we define the field strength tensor

$$F^a_{\mu\nu} \equiv \partial_\mu A^a_\nu - \partial_\nu A^a_\mu + g f^{abc} A^b_\mu A^c_\nu \,, \tag{2.2.2}$$

where A^a_μ represent the $N^2 - 1$ gauge fields, g is the interaction coupling strength and f^{abc} the structure constants of $\mathrm{SU}(N)$ defined via the commutator of the generators

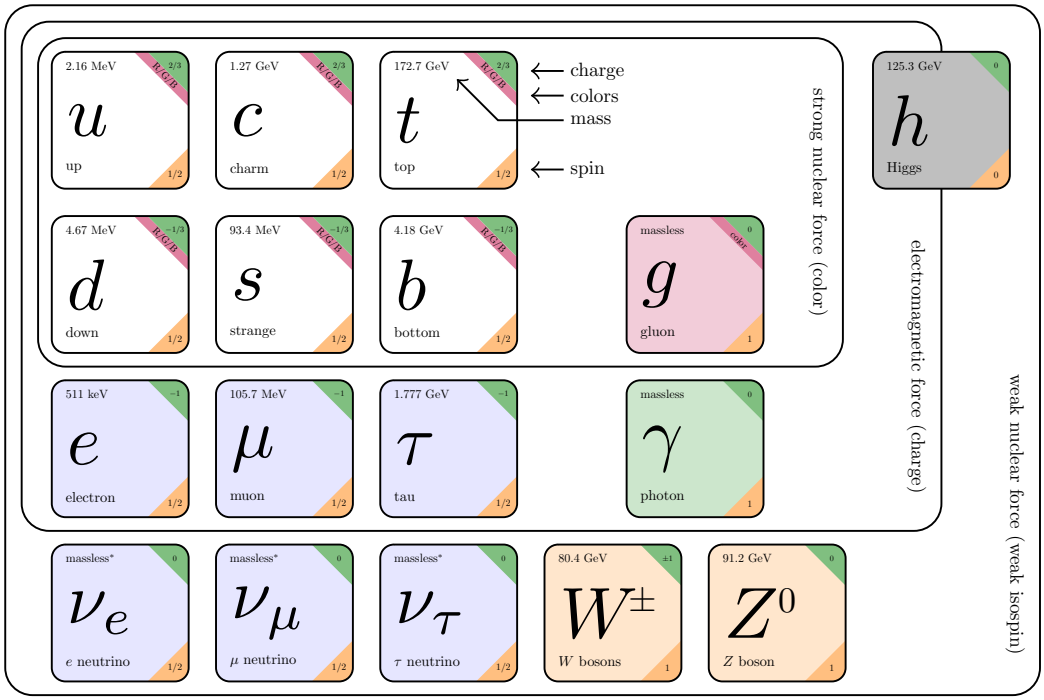

Figure 2.4: Particle content of the Standard Model below the EWSB scale. In the white boxes are the six quarks, interacting via the strong, electromagnetic, and weak forces. In the light blue boxes are the six leptons; in the topmost row are the charged leptons which interact via the electromagnetic and weak forces, and in the second row are the neutrinos which only interact with the weak force. Neutrinos are massless in the SM, but their masses are known to be non-zero from the measurement of neutrino oscillations. The gauge bosons are the gluon, photon, and weak W and Z bosons, mediating the strong, electromagnetic and weak interactions respectively. The Higgs boson responsible for the eponymous mechanism is the grey box. Figure adapted from [11] with updated values from [6].

of the group,

$$[t^a, t^b] = if^{abc}t^c\,. \tag{2.2.3}$$

The 8 generators of the SU(3) group are related to the Gell-Mann matrices $T^a = \lambda_a/2$; and SU(2) has 3 generators defined by $\tau^a = \sigma^a/2$ where σ^a are the Pauli Matrices. The generator of U(1) is simply the identity.

For the SM $\mathrm{SU}(3)_c$ group, there are 8 different gluons corresponding to the 8 generators of SU(3) and we call the coupling strength g_s. For the weak group $\mathrm{SU}(2)_L$, we have 3 weak bosons and the weak coupling is denoted g. Finally, for the Abelian $\mathrm{U}(1)_Y$, a similar definition is used with the structure constants set to 0, meaning the associated B boson does not self-interact, and we call its coupling g'. Overall, the gauge part of the SM Lagrangian can be written as

$$\mathcal{L}_{\text{gauge}} = -\frac{1}{4}G^a_{\mu\nu}G^{\mu\nu a} - \frac{1}{4}W^b_{\mu\nu}W^{\mu\nu b} - \frac{1}{4}B_{\mu\nu}B^{\mu\nu} \tag{2.2.4}$$

with integers a ranging from 1 to 8 and b from 1 to 3, and $G^a_{\mu\nu}$, $W^b_{\mu\nu}$ and $B_{\mu\nu}$ the field strength tensors of the three groups discussed.

Finally, we note that explicit mass terms of the form $m^2 A_\mu A^\mu$ are not gauge invariant and therefore forbidden. Combinations of the W^b and B bosons will acquire masses as the electroweak symmetry $\mathrm{SU}(2)_L \times \mathrm{U}(1)_Y$ is spontaneously broken by the Higgs mechanism introduced in Section 2.2.3.

2.2.2 The Fermion Lagrangian

The second part of the SM Lagrangian is the fermion Lagrangian; it contains the kinematic terms for all fermions in the SM. We differentiate between left- and right-handed chiral components of a fermion field ψ by defining $\psi_L \equiv P_L\psi$ and $\psi_R \equiv P_R\psi$ where we have used the left- and right-handed chiral projectors $P_{L,R} = \frac{1}{2}(1 \mp \gamma^5)$ with γ^5 the fifth gamma matrix. There are then three generations of fermions, each of which contains four left-handed and three right-handed fields.

The up- and down-type quarks u and d are charged under $\mathrm{SU}(3)_c$ and each transform as triplets in the fundamental representation of the strong group; all other fermions are uncharged and transform trivially under SU(3). Chiral components of the fermion fields transform differently under the weak $\mathrm{SU}(2)_L$ group, as such they are commonly grouped into five multiplets: the left-handed quark and lepton doublets $q_L = (u_L, d_L)$ and $l_L = (\nu_L, e_L)$, and the right-handed up- and down-type quark u_R and d_R and charged lepton e_R singlets which transform trivially under $\mathrm{SU}(2)_L$. There are no right-handed neutral leptons ν_R in the SM. Each of these multiplets transforms under $\mathrm{U}(1)_Y$ with a given hypercharge Y, while the quantum number associated with $\mathrm{SU}(2)_L$ is the weak isospin τ^3. The left-handed "up-type" fields u_L and ν_L have $\tau^3 = \frac{1}{2}$, while the "down-type" d_L and e_L have $\tau^3 = -\frac{1}{2}$; all right-handed fields have $\tau^3 = 0$.

For each generation, the up-type quarks are named up u, charm c and top t, the down-type quarks are down d, strange s and bottom b. Similarly, the charged leptons are the electron e, muon μ and tau τ, along with their corresponding neutrinos ν_e, ν_μ and ν_τ. We sum up the gauge transformation properties of each SM field, along with their composition, in Table 2.1.

Following these transformation properties, we define the gauge covariant derivative D_μ such that the fermion kinetic terms remain gauge invariant under SU(3), SU(2) and U(1) transformations. Recalling the generators for each of these groups given earlier we write

$$D_\mu = \partial_\mu - ig_s T^a G^a_\mu - ig\tau^b W^b_\mu - ig' Y B_\mu \,. \tag{2.2.5}$$

Finally, we write the fermion SM Lagrangian,

$$\mathcal{L}_{\text{fermion}} = \bar{q}_L i \not{D} q_L + \bar{u}_R i \not{D} u_R + \bar{d}_R i \not{D} d_R + \bar{l}_L i \not{D} l_L + \bar{e}_R i \not{D} e_R \,, \tag{2.2.6}$$

where we implicitly sum over all three generations, and we have used the Feynman slash notation $\not{D} \equiv \gamma^\mu D_\mu$ and defined the adjoint fermion field $\bar{\psi} \equiv \psi^\dagger \gamma^0$, with γ^μ the gamma matrices.

Field	Composition	$\mathrm{SU}(3)_c$	$\mathrm{SU}(2)_L$	τ^3	Y
G^a	$a = 1, ..., 8$	**8**	**1**		0
W^b	$b = 1, 2, 3$	**1**	**3**		0
B		**1**	**1**		0
q_L	$\begin{pmatrix} u_L \\ d_L \end{pmatrix}, \begin{pmatrix} c_L \\ s_L \end{pmatrix}, \begin{pmatrix} t_L \\ b_L \end{pmatrix}$	**3**	**2**	$\begin{pmatrix} \frac{1}{2} \\ -\frac{1}{2} \end{pmatrix}$	$\frac{1}{6}$
u_R	u_R, c_R, t_R	**3**	**1**	0	$\frac{2}{3}$
d_R	d_R, s_R, b_R	**3**	**1**	0	$-\frac{1}{3}$
l_L	$\begin{pmatrix} \nu_{eL} \\ e_L \end{pmatrix}, \begin{pmatrix} \nu_{\mu L} \\ \mu_L \end{pmatrix}, \begin{pmatrix} \nu_{\tau L} \\ \tau_L \end{pmatrix}$	**1**	**2**	$\begin{pmatrix} \frac{1}{2} \\ -\frac{1}{2} \end{pmatrix}$	$-\frac{1}{2}$
e_R	e_R, μ_R, τ_R	**1**	**1**	0	-1
Φ		**1**	**2**	$\begin{pmatrix} \frac{1}{2} \\ -\frac{1}{2} \end{pmatrix}$	$\frac{1}{2}$

Table 2.1: Transformation properties of each SM field multiplet under $\mathrm{SU}(3)_c$ and $\mathrm{SU}(2)_L$, along with their $\mathrm{U}(1)_Y$ hypercharge Y. The gauge bosons G, W and B transform in the adjoint representation of their respective groups, while the fermions and the Higgs Φ transform in the fundamental representation.

We note the absence of explicit mass terms for any of the SM fermions. Such terms would be written as

$$m\bar{\psi}\psi = m\bar{\psi}_L\psi_R + m\bar{\psi}_R\psi_L\,, \tag{2.2.7}$$

and are not gauge invariant in the presence of chiral gauge interactions. The masses for the fermions will be generated in the Yukawa part of the Lagrangian via the Higgs mechanism introduced in the following section.

2.2.3 The Higgs Mechanism

The final ingredient in the SM is the Higgs boson, and the associated Higgs mechanism responsible for the masses of (nearly) all SM particles. We introduce the Higgs field as a complex scalar $\mathrm{SU}(2)_L$ doublet,

$$\Phi = \frac{1}{\sqrt{2}}\begin{pmatrix}\phi_1 + i\phi_2 \\ \phi_3 + i\phi_4\end{pmatrix}\,, \tag{2.2.8}$$

which is uncharged under $\mathrm{SU}(3)_c$, and with hypercharge $Y = \frac{1}{2}$. We write the associated Lagrangian,

$$\mathcal{L}_{\text{Higgs}} = (D^\mu\Phi)^\dagger(D_\mu\Phi) + \mu^2\Phi^\dagger\Phi - \lambda\left(\Phi^\dagger\Phi\right)^2\,, \tag{2.2.9}$$

where the final two terms make up the Higgs potential. If $\mu^2 > 0$ then the Higgs potential minimum is displaced from zero and the Higgs fields acquires a Vacuum Expectation Value (VEV) at

$$v \equiv \langle\Phi\rangle = \sqrt{\frac{\mu^2}{\lambda}}\,. \tag{2.2.10}$$

This non-zero VEV spontaneously breaks the electroweak $\mathrm{SU}(2)_L\times\mathrm{U}(1)_Y$ symmetry into the electromagnetic $\mathrm{U}(1)_Q$ symmetry; we call this the Electroweak Symmetry Breaking (EWSB).

Of the four massless weak and hypercharge gauge bosons, we then expect a single one, associated with the new unbroken $\mathrm{U}(1)_Q$ symmetry, to remain massless, while the

other three will gain masses as three Goldstone bosons associated with the broken symmetry are absorbed through the gauge choice. To see this, we re-parameterise the Higgs field in the unitary gauge, effectively setting $\phi_1 = \phi_2 = \phi_4 = 0$ and $\phi_3 = v + h$, such that

$$\Phi = \frac{1}{\sqrt{2}} \begin{pmatrix} 0 \\ v + h \end{pmatrix} , \tag{2.2.11}$$

where h is a new real scalar with $\langle h \rangle = 0$; we identify it as the physical Higgs boson, and the fields that were gauged away are the Goldstone bosons whose degrees of freedom (d.o.f.) have been absorbed into the masses of the gauge bosons. In this convention, recalling the definition of the covariant derivative (2.2.5), the kinetic term of (2.2.9) can be expanded as

$$\begin{aligned}(D^\mu \Phi)^\dagger (D_\mu \Phi) = \frac{g^2}{8}(h+v)^2 \left(W^{1\mu} - iW^{2\mu}\right)\left(W^1_\mu + iW^2_\mu\right) \\ + \frac{1}{2}(h+v)^2 \left|\partial_\mu + i\frac{g}{2}W^3_\mu - i\frac{g'}{2}B_\mu\right|^2 .\end{aligned} \tag{2.2.12}$$

Focusing on the $O(v^2)$ terms for now, we identify them as mass terms of new gauge bosons of the broken symmetry and $\mathrm{U}(1)_Q$. We make these new fields explicit by diagonalising these mass terms in the fields. We define the $W^\pm$ and Z bosons via

$$W^\pm_\mu \equiv \frac{1}{\sqrt{2}}\left(W^1_\mu \mp iW^2_\mu\right) \qquad \text{and} \qquad Z_\mu \equiv \frac{1}{\sqrt{g^2 + g'^2}}\left(gW^3_\mu - g'B_\mu\right) , \tag{2.2.13}$$

and identify their masses from (2.2.12) as

$$m_W = \frac{gv}{2} \qquad \text{and} \qquad m_Z = \frac{v}{2}\sqrt{g^2 + g'^2} . \tag{2.2.14}$$

With these definitions, we can rewrite (2.2.9) as

$$\begin{aligned}\mathcal{L}_{\text{Higgs}} = \frac{1}{2}(\partial^\mu h)(\partial_\mu h) - \frac{1}{2}m_h h^2 - g\frac{m_h^2}{4m_W}h^3 - g^2\frac{m_h^2}{32m_W^2}h^4 \\ + m_W^2\left(1 + \frac{h}{v}\right)^2 W^{+\mu}W^-_\mu + \frac{1}{2}m_Z^2\left(1 + \frac{h}{v}\right)^2 Z^\mu Z_\mu ,\end{aligned} \tag{2.2.15}$$

where we have further identified the Higgs boson mass $m_h^2 = 2\lambda v^2$. Finally, recognising that the Z boson was obtained by rotating the W^3_μ and B_μ fields by an angle

$\tan\theta_w \equiv g'/g$, we formally define the massive Z boson and the massless photon A_μ via the rotation

$$\begin{pmatrix} Z_\mu \\ A_\mu \end{pmatrix} \equiv \frac{1}{\sqrt{g^2+g'^2}} \begin{pmatrix} g & -g' \\ g' & g \end{pmatrix} \begin{pmatrix} W_\mu^3 \\ B_\mu \end{pmatrix} . \tag{2.2.16}$$

This rotation angle θ_w is known as the weak angle, or Weinberg angle, and we define the shorthands $c_w \equiv \cos\theta_w = \frac{g}{\sqrt{g^2+g'^2}}$ and $s_w \equiv \sin\theta_w = \frac{g'}{\sqrt{g^2+g'^2}}$. To complete the rotation of the SM Lagrangian to the gauge bosons mass basis, we transform (2.2.5) accordingly,

$$D_\mu = \partial_\mu - ig_s T^a G_\mu^a - i\frac{g}{\sqrt{2}}\left(\tau^+ W_\mu^+ + \tau^- W_\mu^-\right) - i\frac{g}{c_w}\left(\tau^3 - s_w^2 Q\right) Z_\mu \\ - ieQA_\mu \,, \tag{2.2.17}$$

where we have identified the unit of the $\mathrm{U}(1)_Q$ charge, the electric charge, via

$$e \equiv \frac{gg'}{\sqrt{g^2+g'^2}} = g'c_w = gs_w \,, \tag{2.2.18}$$

the corresponding charge operator $Q = \tau^3 + Y$, and the weak operators $\tau^\pm = \tau^1 \pm i\tau^2$.

The derivation of the gauge mass eigenstates can be reproduced in a generic gauge, leading to identical mass terms, but additional interactions between the gauge, Higgs, and Goldstone bosons remaining. In generic gauge, the Higgs doublet is written as

$$\Phi = \begin{pmatrix} \varphi^+ \\ \frac{1}{\sqrt{2}}\left(v + h + i\varphi_Z\right) \end{pmatrix} , \tag{2.2.19}$$

with a complex scalar $\varphi^\pm \equiv \frac{1}{\sqrt{2}}(\phi_1 \pm i\phi_2)$ and a real scalar $\varphi_Z \equiv \phi_4$. Relevant interaction terms and Feynman rules can be found in [10].

As we saw earlier, explicit mass terms for fermions are forbidden, however the Higgs VEV v allows us to generate masses through the Yukawa Lagrangian,

$$\mathcal{L}_{\text{Yukawa}} = -\bar{q}_L \boldsymbol{Y}_u u_R \tilde{\Phi} - \bar{q}_L \boldsymbol{Y}_d d_R \Phi - \bar{l}_L \boldsymbol{Y}_e e_R \Phi + \text{h.c.} \tag{2.2.20}$$

where we have defined $\tilde{\Phi} \equiv i\sigma^2 \Phi^\dagger$ to make the term involving the up-type quarks gauge-invariant, and where $\boldsymbol{Y}_u$, $\boldsymbol{Y}_d$ and $\boldsymbol{Y}_e$ are the three complex Yukawa matrices.

These matrices are arbitrary but can be diagonalised by defining

$$\boldsymbol{Y}_f = \boldsymbol{U}_f \boldsymbol{M}_f \boldsymbol{K}_f^\dagger = \boldsymbol{U}_f \begin{pmatrix} y_{1f} & 0 & 0 \\ 0 & y_{2f} & 0 \\ 0 & 0 & y_{3f} \end{pmatrix} \boldsymbol{K}_f^\dagger \,, \tag{2.2.21}$$

where $\boldsymbol{U}_f$ and $\boldsymbol{K}_f$ are two unitary matrices and $\boldsymbol{M}_f$ a diagonal matrix with real coefficients y_i. Setting the Higgs field to its VEV in (2.2.20), we find the fermion mass terms,

$$\mathcal{L}_{\text{Yukawa}} = -\frac{v}{\sqrt{2}} \left(y_u \bar{u}_L \boldsymbol{U}_u \boldsymbol{K}_u^\dagger u_R + y_d \bar{d}_L \boldsymbol{U}_d \boldsymbol{K}_d^\dagger d_R + y_l \bar{e}_L \boldsymbol{U}_e \boldsymbol{K}_e^\dagger e_R + \text{h.c.} \right) + O(h) \,, \tag{2.2.22}$$

with the $O(h)$ terms describing all interactions between the fermions and the Higgs boson. We finally redefine our fermion fields into the mass basis using the chiral rotations

$$u_L \to \boldsymbol{U}_u u_L \,,\; u_R \to \boldsymbol{K}_u u_R \,,\; d_L \to \boldsymbol{U}_d d_L \,,\; d_R \to \boldsymbol{K}_d d_R \,,\; e_L \to \boldsymbol{U}_e e_L \,,\; e_R \to \boldsymbol{K}_e e_R \tag{2.2.23}$$

to obtain the fermion mass terms,

$$\mathcal{L}_{\text{Yukawa}} = -m_u \bar{u}_L u_R - m_d \bar{d}_L d_R - m_e \bar{e}_L e_R + \text{h.c.} + O(h) \,, \tag{2.2.24}$$

with $m_f \equiv y_f v/\sqrt{2}$. Thus, we have obtained non-zero masses for the quarks and charged leptons. Due to the absence of right-handed neutrinos, neutrinos remain massless through the Higgs mechanism and can be freely rotated to set $\boldsymbol{Y}_e$ diagonal.[4]

This rotation into the mass basis however has consequences for quarks. When expanding the terms in the fermion Lagrangian (2.2.6), only the $\boldsymbol{U}_u$ and $\boldsymbol{U}_d$ matrices remain, in the terms involving interactions between the $W^\pm$ bosons and quarks,

$$\mathcal{L}_{\text{fermion}} \supset \frac{g}{\sqrt{2}} \left(W_\mu^+ \bar{u}_L \gamma^\mu \boldsymbol{U}_u^\dagger \boldsymbol{U}_d d_L + W_\mu^- \bar{d}_L \gamma^\mu \boldsymbol{U}_d^\dagger \boldsymbol{U}_u u_L \right) . \tag{2.2.25}$$

As the combination $\boldsymbol{U}_u^\dagger \boldsymbol{U}_d$ needs not be diagonal, these terms cause explicit mix-

[4] In contradiction with the SM, neutrinos are now known to have non-zero masses through observations of neutrino oscillations [12, 13].

ing between quarks of different generations. We define a single matrix parameterising these flavour violating effects $\boldsymbol{V} \equiv \boldsymbol{U}_u^\dagger \boldsymbol{U}_d$, known as the Cabbibo-Kobayashi-Maskawa (CKM) matrix.

2.2.4 The Running of the SM

As we demonstrated in Section 2.1, renormalisation causes physical constants to acquire a dependency on the energy scale μ. This is also the case for the SM, and all parameters used, such as masses and couplings, have to be carefully evaluated at the relevant energy scale. Here we give the beta functions, as defined in (2.1.30), for the couplings of each interaction, defining $\alpha_s \equiv \frac{g_s^2}{4\pi}$, $\alpha_2 \equiv \frac{g^2}{4\pi}$ and $\alpha_1 \equiv \frac{g'^2}{4\pi}$ above the EWSB scale, and $\alpha \equiv \frac{e^2}{4\pi}$ below; as well as the running of the top quark mass m_t. For further details, we refer to [14–16] evaluating the complete set of SM RGEs up to 2-loop order.

Up to 2-loops, the QCD beta function is given by

$$\beta(\alpha_s) = -\frac{33 - 2n_q}{3}\frac{\alpha_s^2}{2\pi} - \frac{153 - 19n_q}{3}\frac{\alpha_s^3}{4\pi^2}\,, \tag{2.2.26}$$

with n_q the number of quarks d.o.f. available at a given energy scale. [6]

At 1-loop, the running for the $\mathrm{SU}(2)_L$ and $\mathrm{U}(1)_Y$ couplings above the EWSB scale are

$$\beta(\alpha_2) = -\frac{19}{6}\frac{\alpha_2^2}{2\pi} \qquad \text{and} \qquad \beta(\alpha_1) = \frac{41}{6}\frac{\alpha_1^2}{2\pi}\,, \tag{2.2.27}$$

while below this scale, the QED beta function for the $\mathrm{U}(1)_Q$ coupling is

$$\beta(\alpha) = \frac{4}{3}\sum_f N_c^f Q_f^2 \frac{\alpha^2}{2\pi} \tag{2.2.28}$$

where the sum over f runs over all fermions available at a given energy scale, with N_c the number of colours (3 for quarks, 1 for leptons) and Q_f the electric charge for each fermion. [17]

Finally, neglecting the effect of electroweak interactions, the running of the top quark

mass is described via the running of the top Yukawa coupling with $\alpha_t \equiv \frac{y_t^2}{4\pi}$, [18]

$$\beta(\alpha_t) = \left(\frac{9}{2}\alpha_t - 8\alpha_s\right)\frac{\alpha_t}{2\pi}\,. \tag{2.2.29}$$

2.3 The Case for Dark Matter

Despite its many successes and its ubiquity, the SM suffers from a number of shortcomings. The wide range of masses of its components [6], the absence of Charge-Parity (CP) symmetry violation in QCD [19], its failure to predict neutrino oscillations (and therefore masses) [12, 13], the problematic value of the muon's magnetic moment [20], recent discrepancies in the measured mass of the W boson [21], inconsistencies in the measurement of the proton radius [22], and the absence of gravity altogether form only some of the overwhelming evidence that there must be something beyond. Extensions of the SM are designated under the moniker of "Beyond the Standard Model (BSM) physics". Interestingly, one of the greatest flaws in our model of the infinitely small comes from the study of the infinitely large. As early as the 1930s, with F. Zwicky's work on the Coma cluster [23], astronomers started noticing that galaxies did not rotate as expected: stars in the outer reaches of galaxies all move at similar speeds, despite Keplerian dynamics suggesting their velocity should fall with increasing distance to the centre. [24, 25] Increasingly numerous and precise observations of this phenomenon [26–28] led astronomers to postulate the existence of invisible matter surrounding the visible galaxy, accounting for as much as 4/5 of its total mass on average. Thus was popularised the idea of *Dark Matter (DM)*[5].

Now, it would be disingenuous to introduce the hypothesis of DM without mentioning its alternatives. A class of theories, known collectively as modified gravity theories (see [31] for a review), postulate that General Relativity (GR) inaccurately describes gravity at the largest scales, and that the anomalous rotation of galaxies

[5]The term "dark matter" itself was coined as early as 1906 by Henri Poincaré, as "matière obscure" [29]. For a review on the history of dark matter, see [30].

can be explained with a framework superseding GR. The most famous of these being Modified Newtonian Dynamics (MOND) [32]. As we will see below, evidence for DM spreads far beyond rotation curves, and minimal modified gravity theories are unable to reproduce this evidence [33–36], necessitating more intricate models which forfeit the elegant simplicity of the MOND hypothesis. Henceforth, and following the consensus of the particle physics community, we will only consider the hypothesis of particulate DM as a solution to the DM problem, cemented in the Cosmological Standard Model, better known as ΛCDM.

Since the discovery of the galactic rotation curves, there have been numerous astronomical and cosmological observations that challenge the SM as a standalone explanation for the content of the Universe. Imaging of the infamous Bullet Cluster's mass distribution [33], surveys of weak gravitational lensing [37], mapping of the large-scale structure of the Universe, through Baryon Acoustic Oscillations (BAO) [38] or weak lensing [39], the shape of the Cosmic Microwave Background (CMB) power spectrum [40], and calculations of the yields of light elements from Big Bang Nucleosynthesis (BBN) [41] are only some of the observations which overwhelmingly favour the DM hypothesis. In spite of its own shortcomings [42], ΛCDM is the most successful cosmological model to date, and predicts a Universe made of $\sim 5\%$ visible matter, $\sim 26\%$ dark matter, and $\sim 70\%$ dark energy[6]. [40]

All evidence of DM's existence so far have been through its gravitational interactions with visible matter. The few known (or at least supposed) properties of DM can be inferred from fairly straightforward arguments. First, BBN simulations and measurements of the CMB suggest that not more than a few percent of the Universe's total energy could have formed as ordinary, baryonic matter; DM must then be non-baryonic, hence the need for exotic candidates. Secondly, the lack of measured interactions between dark and visible matters means that it must be at most very feebly coupled to SM interactions. Similarly, objects such as the Bullet Cluster sug-

[6]Dark energy, the Λ in ΛCDM, is a parameter needed to account for the accelerating expansion of the Universe.

gest that DM is nearly collisionless, placing stringent bounds on its self-interactions. Then, the sizes of the smallest DM haloes give indications that it must move slowly enough to be gravitationally bound; this translates into lower bounds for DM mass, through the Compton wavelength for bosonic DM, or Fermi pressure for fermionic DM. Combined with simulations of structure formation, this also indicates that DM must have been non-relativistic (cold) in the early Universe as well.[7] Finally, observations of the effects of DM at various epochs suggest that its abundance must have been roughly constant throughout the evolution of the Universe, meaning that it must have a lifetime at least equal to the age of the Universe. In order for new fields to be considered suitable DM candidates, it is then sufficient that they fulfil these five requirements. This leaves an overwhelmingly large range of possible DM candidate theories, an exhaustive list of which is beyond the scope of the reader's time (see [45] for a review of some of the more popular candidates).

2.3.1 Dark Matter Production

The various models attempting to describe DM must all predict the correct DM density observed in the Universe today. This so-called *relic abundance* is often expressed as a fraction of the total Universe energy density, $\Omega_{\rm DM}h^2 = 0.12$ [40][8] with $h = H_0/100$ the reduced Hubble constant, while DM production mechanisms output a comoving number density, or *yield* $Y \equiv n_{\rm DM}/s$, with $n_{\rm DM}$ the DM number density and s the Universe entropy density. The value of the yield corresponding to the correct relic abundance is given by

$$Y = \frac{\rho_c}{m_{\rm DM} s h^2}(\Omega_{\rm DM}h^2) \approx 4 \times 10^{-10} \left(\frac{1\,\text{GeV}}{m_{\rm DM}}\right), \tag{2.3.1}$$

with $\rho_c = 3H_0^2/8\pi G_N$ the critical density of the Universe, and $m_{\rm DM}$ the mass of the DM particle. Depending on the model and DM mass, there are three popular scenari

[7] We note that the cold DM paradigm can cause discrepancies in simulated and measured halo profiles for dwarf galaxies, this is known as the *cusp-core problem* [43, 44].

[8] Not to be confused with the much larger local DM density $\rho_{\rm DM} \approx 0.4\,\text{GeV}\,\text{cm}^{-3}$ describing the density of the Milky Way's DM halo.

for DM production: thermal freeze-out, freeze-in, and vacuum misalignment.

In the Freeze-Out (FO) scenario, DM particles are originally abundant and in thermal equilibrium with the Universe plasma, and creation and annihilation processes, schematically $\mathrm{DM} + \mathrm{DM} \leftrightarrow \mathrm{SM} + \mathrm{SM}$, are balanced out. As the temperature of the plasma drops below the DM mass, $x \equiv m_{\mathrm{DM}}/T \gtrsim 1$, the rate of DM creation processes diminishes and the DM abundance falls as annihilation processes become energetically favoured. When DM becomes sparse enough, mainly through annihilation processes, the rate of DM annihilation processes drops to zero, and the DM abundance is "frozen-out" of equilibrium at the relic abundance. The critical density at which DM decouples, and therefore the relic abundance, is inversely proportional to the DM annihilation cross-section $\langle \sigma v \rangle$. To reproduce the correct relic density, we require a cross-section $\langle \sigma v \rangle \sim G_F^2 m_{\mathrm{DM}}^2$, with G_F the Fermi constant and $m_{\mathrm{DM}} \sim m_W$. In other words, particles with masses of $O(100\,\mathrm{GeV})$ interacting with strength comparable to the weak interaction can reproduce the relic density; this coincidence is known as the *WIMP miracle* and motivates an especially popular class of DM candidates known as Weakly-Interacting Massive Particles (WIMPs).

In contrast, Freeze-In (FI) requires the initial abundance of DM to be very small, such that the DM is thermally decoupled from the plasma. Creation processes slowly increase the DM density until they become disfavoured at $x \gtrsim 1$. At this point, smaller couplings than that in the FO scenario guarantee that annihilation processes never become common enough to reduce the DM abundance, and it is then "frozen into" its relic abundance. As opposed to FO, the FI yield increases with the DM interaction cross-section. A schematic evolution of the yield Y as a function of the parameter x for both FI and FO mechanisms is shown in Figure 2.5.

Finally, in the case where DM-SM couplings are too small for either FO or FI, the relic abundance can still be generated via the Vacuum Misalignment (VM) mechanism. VM occurs when, at some temperature T_1, the potential of a field $V(\phi)$ is displaced away from its minimum by a small value $\phi_1 = \phi(T_1)$ (*e.g.* through non-perturbative effects shifting the minimum of the potential, or through ϕ simply

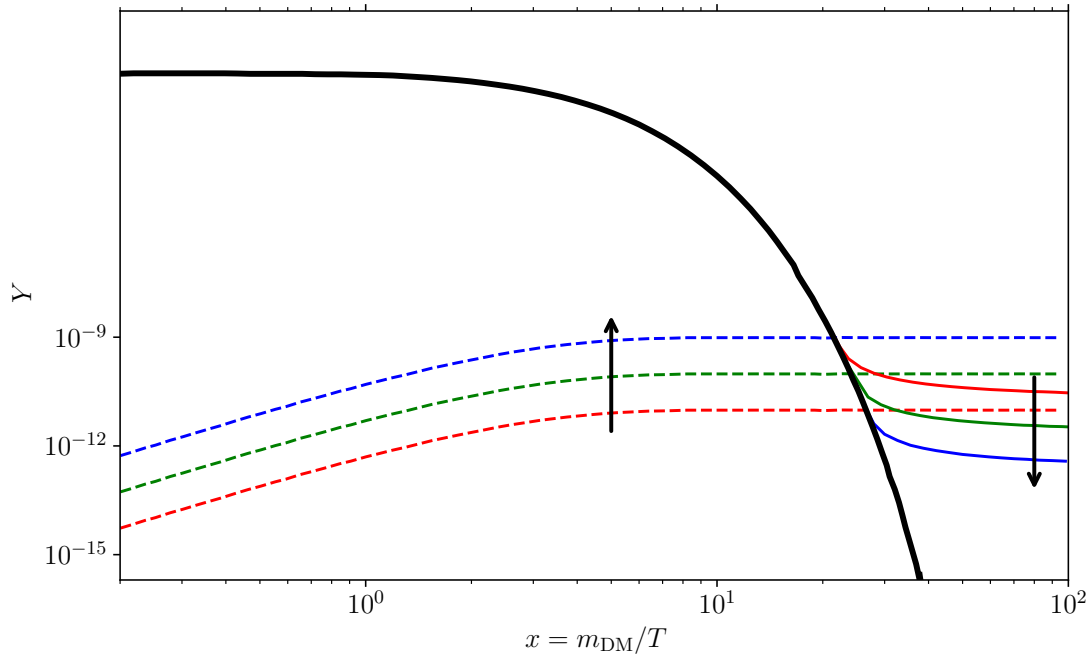

Figure 2.5: Schematic evolution of the DM yields for thermal freeze-out (solid coloured) and freeze-in (dashed coloured) as a function of $x = m_{\rm DM}/T$. The black solid line indicates the yield assuming equilibrium is maintained, while the arrows indicate the effect of increasing the cross-section $\langle \sigma v \rangle$ for the two processes. Figure reproduced from [46].

being created at a random value away from the minimum). The evolution of the field ϕ can be described by the equation of motions in an expanding Universe; using the Friedmann-Lemaître-Robertson-Walker metric, it reads

$$\ddot{\phi} + 3H\dot{\phi} + m_\phi^2 \phi = 0\,, \tag{2.3.2}$$

where we recognise the equation for a damped harmonic oscillator. If the misalignment occurs at a temperature high enough that the Hubble constant $H(T_1)$ is much greater than the field mass $m_\phi(T_1)$, then the field behaves like an overdamped oscillator and is prevented from rolling down to its minimum. As the Universe cools down, if H drops below the critical value $3H(T_{\rm osc}) = m_\phi(T_{\rm osc})$, the field begins to oscillate around its minimum with an energy density

$$\rho(T_{\rm osc}) = \frac{1}{2} m_\phi(T_{\rm osc})^2 \phi_{\rm osc}^2\,, \tag{2.3.3}$$

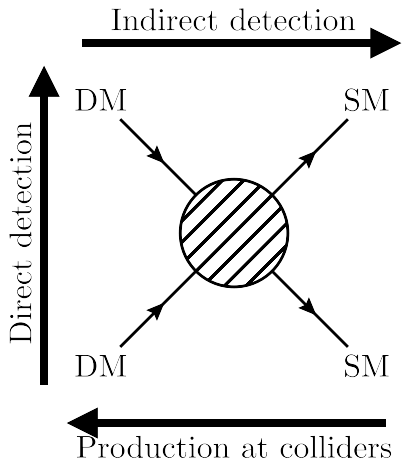

Figure 2.6: Diagram illustrating the main dark matter detection directions.

where $\phi_{\rm osc} = \phi(T_{\rm osc}) \sim \phi_1$ is the value that the field reached by slowly rolling down from ϕ_1. The relic density can be extracted by redshifting the density $\rho(T)$ from $T_{\rm osc}$ down to the current temperature of the Universe $T_0 = 2.7\,\mathrm{K}$; the details of this procedure depend on the functional form of $m_\phi(T)$, and therefore the model considered.

2.3.2 Dark Matter Detection

Now that we have argued for the existence of DM, given some of its basic properties, and outlined three production mechanisms, all that remains is to find it. All methods to detect DM rely on its unknown non-gravitational interactions with SM fields, and it is helpful to orient them along three main avenues, as illustrated in Figure 2.6. There are of course experiments that do not quite fit in these categories, such as those using coherent interactions with the DM field, especially used for light bosonic DM; but they are sufficient to give an overview of the field of DM detection.

Direct detection relies on DM particles scattering against SM particles, presumably situated inside a detector, and transferring some energy that can be measured, signalling the passage of the DM. The exact process through which the detection occurs depends on the nature of the candidate. An especially popular method for WIMPs

are experiments based on nuclear recoil [47–50]. Beyond particle-particle scattering, we also mention methods where the DM field interacts coherently with the detector material, preferred for ultralight DM, such as axion haloscopes [51–53] or atom interferometers [54–56]. Several reviews exist on the topic, see for example [57] to mention just one.

On the other hand, indirect detection experiments rely on DM particles from astronomical sources annihilating into SM particles that can then be detected in telescopes. X-ray and gamma telescopes directly measure high-energy photons or cosmic rays from astrophysical sources [58–61], while Cherenkov detectors measure Cherenkov radiation emitted as a cosmic ray passes through the detector material [62, 63]. At cosmological scales, DM can be detected through its imprint on the CMB [40, 64], or via baryon acoustic oscillations [38, 65]. Finally, measurements of neutrino fluxes from the Sun or nuclear reactors can also be used to infer the presence of DM [66–69]. Some reviews on indirect DM detection are [70, 71].

Finally, the third DM detection direction is to produce SM particles in colliders and measure their outgoing momentum, with the hope that missing momentum in the final state can be interpreted as DM particles escaping the detector. Searches have been and are being conducted, notably by the ATLAS [72, 73] and CMS [74, 75] detectors at the LHC. For a review on collider searches of DM, specifically at the LHC, see [76].

2.4 Axions and the Like

2.4.1 The Strong CP Problem

One of the more interesting candidates for DM originates from an *a priori* unrelated issue in the QCD sector. The so-called *strong CP problem* states that despite the CP violating angle $\bar{\theta}$ allowed in the QCD Lagrangian being free in the theory, and

therefore expected to be $O(1)$ from naturalness arguments, measurements of the neutron Electric Dipole Moment (EDM) constrain it to $|\bar{\theta}| \lesssim 10^{-10}$ [77].

To see where the CP violating term arises from, let us start by considering a simple model with a quark field with Lagrangian density

$$\mathcal{L} = \bar{\psi}\left(i\not{D} - m\right)\psi\,, \tag{2.4.1}$$

with an associated gauge field A_μ under which the quark field has charge g. Under the chiral rotation of the quark fields, defined by $\psi \to e^{i\gamma^5\alpha}\psi$ (or alternatively $\psi_L \to e^{-i\alpha}\psi_L$ and $\psi_R \to e^{i\alpha}\psi_R$), this Lagrangian transforms as

$$\mathcal{L} \to \mathcal{L} - 2im\alpha\bar{\psi}\gamma^5\psi + O(\alpha^2)\,, \tag{2.4.2}$$

and is only invariant in the massless limit. Alternatively, we can use the equations of motions to show that the associated axial current $j_5^\mu \equiv \bar{\psi}\gamma^\mu\gamma^5\psi$ is only conserved if $m \to 0$ as

$$\partial_\mu j_5^\mu = 2im\bar{\psi}\gamma^5\psi\,. \tag{2.4.3}$$

We have however omitted an important aspect in this reasoning by considering only the Lagrangian density: the path integral formulation of QFT tells us that the object to consider is instead the functional integral

$$Z = \int \mathcal{D}\psi\mathcal{D}\bar{\psi}\exp\left[i\int \mathrm{d}^4x\ \bar{\psi}\left(i\not{D} - m\right)\psi\right]\,. \tag{2.4.4}$$

Now, performing the chiral rotation not only involves acting on the fields in the Lagrangian, but also carefully transforming the path integral measure $\mathcal{D}\psi\mathcal{D}\bar{\psi}$ [78,79]. A full derivation of this transformation is shown in Section 19.2 of [4], we only state the final result,

$$Z \to \int \mathcal{D}\psi\mathcal{D}\bar{\psi}\exp\left\{i\int \mathrm{d}^4x\left[\bar{\psi}\left(i\not{D} - m\right)\psi + \alpha\left(\partial_\mu j_5^\mu + \frac{g^2}{8\pi^2}F_{\mu\nu}\tilde{F}^{\mu\nu}\right)\right]\right\}\,, \tag{2.4.5}$$

with $F_{\mu\nu}$ the field strength tensor of A_μ and we have defined the dual of a field strength tensor $\tilde{F}^{\mu\nu} \equiv \frac{1}{2}\varepsilon^{\mu\nu\alpha\beta}F_{\alpha\beta}$ with ε the Levi-Civita symbol. The chiral symmetry, despite being conserved in the Lagrangian, is broken in the functional integ-

ral; we then call it an *anomalous symmetry*. This anomaly in the chiral symmetry is known as the chiral anomaly, axial anomaly, or Adler-Bell-Jackiw (ABJ) anomaly [80, 81].

Another piece of the puzzle comes when realising that there exists an additional term allowed in the SM Lagrangian that we have omitted so far,

$$\mathcal{L}_{\text{SM}} \supset \theta \frac{g_s^2}{32\pi^2} G^a_{\mu\nu} \tilde{G}^{\mu\nu a} \,, \tag{2.4.6}$$

known as the CP violating *theta term*. Clearly, there then exists some interplay in the SM between chiral rotations of the quarks, the chiral anomaly, and this theta term generated by the former two. Recalling the chiral rotations used to diagonalise the Yukawa matrices (2.2.21) and (2.2.23), without loss of generality we rewrite the Yukawa matrices as [5]

$$\boldsymbol{Y}_f = \boldsymbol{U}_f \boldsymbol{M}_f \boldsymbol{U}_f^\dagger \boldsymbol{K}_f^\dagger \,, \tag{2.4.7}$$

which we can diagonalise by performing chiral rotations on the right-handed fields $u_R \to \boldsymbol{K}_u u_R$ and $d_R \to \boldsymbol{K}_d d_R$ only and then non-chiral rotations $u \to \boldsymbol{U}_u u$ and $d \to \boldsymbol{U}_d d$. These chiral rotations will induce a phase [5]

$$\eta = \arg\left[\det\left(\boldsymbol{K}_d \boldsymbol{K}_u\right)\right] = -\arg\left[\det\left(\boldsymbol{Y}_d \boldsymbol{Y}_u\right)\right] \,, \tag{2.4.8}$$

and the CP violating theta term becomes

$$\mathcal{L}_{\text{SM}} \supset \bar{\theta} \frac{g_s^2}{32\pi^2} G^a_{\mu\nu} \tilde{G}^{\mu\nu a} \,, \tag{2.4.9}$$

with $\bar{\theta} \equiv \theta - 2\eta$. Chiral rotations by an angle α then just move the phase between θ and η, such that $\eta \to \eta + \alpha$ and $\theta \to \theta + 2\alpha$, leaving $\bar{\theta}$ unchanged. The angle $\bar{\theta}$ is then a free parameter, and a measurable physical quantity known as the *strong CP phase* or *angle*.

There is however a reason why we did not include the theta term when writing down the Lagrangian of the SM in Section 2.2: by manipulating the structure in the theta

term, one can show that it can be written as

$$G^a_{\mu\nu}\tilde{G}^{\mu\nu a} = \partial_\mu K^\mu\,, \quad \text{with} \quad K^\mu \equiv \varepsilon^{\mu\nu\alpha\beta}\left(G^a_\nu G^a_{\alpha\beta} - \frac{g}{3}f^{abc}G^a_\nu G^b_\alpha G^c_\beta\right)\,, \tag{2.4.10}$$

where K^μ is known as a Chern-Simons current. In other words, the theta term is a total derivative and will therefore be unable to contribute to any process in perturbation theory. There may nonetheless be physical consequences through non-perturbative effects.

It turns out that in Chiral Perturbation Theory (χPT), $\bar{\theta}$ generates a CP violating coupling between the nucleon doublet and the pion.[9] This coupling takes the form $\bar{g}_{\pi NN} = -\bar{\theta}\frac{c_+\mu}{f_\pi}$ where $c_+ = c_1 + c_2 \approx 1.7\,\text{GeV}^{-1}$ [85], $\mu \equiv \frac{m_u m_d}{m_u+m_d}$, and f_π is the pion decay constant. [84] Then, evaluating loop diagrams such as the one shown in Figure 2.7 and casting the result onto an effective neutron EDM operator,

$$\mathcal{O}_{\text{EDM}} = d_n F_{\mu\nu}\bar{n}i\sigma^{\mu\nu}\gamma^5 n\,, \tag{2.4.11}$$

with $\sigma^{\mu\nu} \equiv \frac{i}{2}[\gamma^\mu, \gamma^\nu]$ the commutator of gamma matrices, we find

$$d_n = \bar{\theta}\frac{e g_A c_+ \mu}{8\pi^2 f_\pi^2}\log\frac{\Lambda^2}{m_\pi^2} \approx 3\times 10^{-16}\bar{\theta}\; e\,\text{cm}\,, \tag{2.4.12}$$

with the isovector coupling $g_A = 1.2754(13)$ [6], and where we set a UV cutoff at $\Lambda = 4\pi f_\pi$. Current experimental results place bounds on the neutron EDM at $d_n \lesssim 10^{-26}\; e\,\text{cm}$ [86, 87], leading to a maximal value for the strong CP angle, $\bar{\theta} \lesssim 10^{-10}$.

A simple solution to the strong CP problem would be having one (or more) quarks be massless at some mass scale, $m_q = 0$. In this case, (2.4.8) does not hold and θ could simply be rotated away from the Lagrangian by redefining the quark field q. As the theory is run from the high scale to a lower scale, instanton effects would actually be able to generate masses at a low scale comparable to current estimates [82], however the fine-tuning problem is shifted from making $\bar{\theta}$ small to making m_q small, and one

[9] See [82–84] for more detailed reviews of the strong CP problem and its links to the neutron EDM.

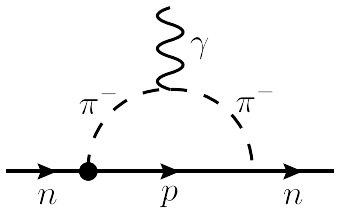

Figure 2.7: 1-loop diagram contributing to the neutron EDM through CP violating couplings between nucleons and pions. The bullet represents the CP violating coupling.

still need to find a suitable explanation for this.

Alternatively, if the high-scale theory superseding the SM is CP conserving, then a bare θ parameter, and so the theta term (2.4.6), would be forbidden in the UV theory. In this theory, CP violation must arise spontaneously, somehow without generating an explicit theta term while still reproducing the observed CP violation in the weak sector. Such theories include Nelson-Barr models [88, 89], as well as other models based on string theory and/or supersymmetry (see e.g. Refs. [26–31] from the review by A. Hook [84]).

2.4.2 The QCD Axion

A third, and currently the most popular, solution to the strong CP problem is the so-called *QCD axion* [90, 91]. The basic idea consists in adding a new anomalous U(1) symmetry we call the Peccei-Quinn (PQ) symmetry. This symmetry is spontaneously broken at a high energy scale $\Lambda_{\rm PQ}$ by an additional term associated with a new Goldstone boson a,[10]

$$\mathcal{L}_a = \left(\bar{\theta} + \frac{a}{f}\right) \frac{g_s^2}{32\pi^2} G^a_{\mu\nu} \tilde{G}^{\mu\nu a} + \text{kin.}\,, \tag{2.4.13}$$

with the rest of the SM Lagrangian obeying the shift symmetry $a \to a + \alpha$. The effective CP phase of this theory is then $\theta_{\rm eff} = \bar{\theta} + \frac{a}{f}$. Then, by a shift in a, we can eliminate this effective strong CP angle and solve the strong CP problem. In fact,

[10] Not to be confused with the $\mathrm{SU}(3)_c$ index a which only appears in the $G\tilde{G}$ structure.

one can write the vacuum energy as a function of $\bar{\theta}$ and a as [5]

$$E(\bar{\theta}) = -m_\pi^2 f_\pi^2 \cos\left(\bar{\theta} + \frac{a}{f}\right) . \tag{2.4.14}$$

Then, shifting a to eliminate θ_{eff} corresponds to giving a a VEV at $\langle a \rangle = -\bar{\theta} f$; the vacuum energy potential then has a minimum at $\theta_{\text{eff}} = 0$ and excitations around this minimum are axion particles. We call a the axion field and $f \sim \Lambda_{\text{PQ}}$ the axion decay constant. Expanding (2.4.14) in a/f, one finds an estimate for the mass of the axion $m_a \sim \frac{m_\pi f_\pi}{f}$, which for the minimal $\text{U}(1)_{\text{PQ}}$ model gives $m_a \sim 10 - 100\,\text{keV}$ [92, 93].

As a brief aside, we mention the so-called axion quality problem, or whether it is justified that the QCD contribution to the axion potential dominates over other contributions that may arise as a result of the PQ symmetry breaking at a high scale [94–97]. This theoretical issue is not directly relevant for this work and we will not discuss it further.

This new light and long-lived particle is an attractive candidate for DM, and while the PQ model was quickly ruled out [98], several more complex models opened up the parameter space for an axion to solve both the CP and DM problems [99]. UV completions for the QCD axion are often grouped into two categories:

- Kim-Shifman-Vainshtein-Zakharov (KSVZ) models [100, 101], in which one introduces one or several new heavy quark fields Q charged under the $\text{U}(1)_{\text{PQ}}$ symmetry, generating (2.4.13) through the anomalous symmetry, and any other couplings at loop-level.

- Dine-Fischler-Srednicki-Zhitnitsky (DFSZ) models [102, 103], in which one adds at least one new Higgs scalar doublet and charges the SM fermions under $\text{U}(1)_{\text{PQ}}$, in addition to (2.4.13), axion-fermion couplings may therefore occur at tree level.

In this work, we will treat the axion model as an effective theory and not consider specific UV completions unless necessary. See [104] for an extensive review of several types of axion models.

Owing to the popularity of the DM problem over the strong CP problem, many axion models have been written to make suitable candidates for DM, sometimes at the cost of their ability to solve the problem they were created for. While literature often refers to "axions" ambiguously, we will emphasize this distinction and call "QCD axions" particles that solve the strong CP problem through a variant of the PQ mechanism, and with a mass $m_a \sim \frac{m_\pi f_\pi}{f}$. The term "Axion-Like Particle (ALP)", or "axion" without any qualifier, will refer to more generic DM candidates with pseudoscalar and anomalous couplings similar to that of the QCD axion, that need not solve the strong CP problem.

2.4.3 Axions at Different Scales

In order to study ALPs generally, without restricting ourselves to a specific model, we use an Effective Field Theory (EFT) approach. EFTs are a class of theories in which one considers all or specific operators defined at a low energy scale, whereby the UV behaviour of the theory has been integrated out and is only present through calculable coefficients scaling the operators, called *Wilson coefficients*. The SM can be treated as an EFT where effects of unknown high-energy phenomena determine the values of its many parameters [105]; alternatively, the archetype of an EFT is the Standard Model Effective Field Theory, or SMEFT [106–108], in which all possible operators involving SM fields are considered.[11] We treat here the ALP similarly: by writing down all its interactions below a new physics scale Λ with Wilson coefficients for couplings.

The most generic effective ALP Lagrangian above the EWSB scale that one can write up to dimension-5 reads [17]

$$\mathcal{L}_a^{(5)} = \frac{1}{2}(\partial_\mu a)(\partial^\mu a) - \frac{1}{2}m_{a,0}^2 a^2 + \frac{\partial_\mu a}{f}\sum_\psi \bar{\psi}\mathbf{c}_\psi\gamma^\mu\psi$$

[11] The SMEFT assumes an SM Higgs doublet of the form (2.2.8); relaxing this assumption yields what is known as Higgs Effective Field Theory, or HEFT. A discussion of both theories is included in [105].

$$+ c_{GG}\frac{\alpha_s}{4\pi}\frac{a}{f}G^a_{\mu\nu}\tilde{G}^{\mu\nu a} + c_{WW}\frac{\alpha_2}{4\pi}\frac{a}{f}W^b_{\mu\nu}\tilde{W}^{\mu\nu b} + c_{BB}\frac{\alpha_1}{4\pi}\frac{a}{f}B_{\mu\nu}\tilde{B}^{\mu\nu}\,. \quad (2.4.15)$$

Here, the sum extends over the SM fermion fields $\psi \in \{u, d, e, \nu\}$ and the $\boldsymbol{c}_\psi$ are Hermitian coupling matrices. The axion decay constant f is related to the new physics scale $\Lambda = 4\pi f$, assumed to be well above the weak scale. Finally, $m_{a,0}$ is the bare axion mass, taken to be zero when considering the QCD axion as the Goldstone boson of the broken $\mathrm{U}(1)_{\mathrm{PQ}}$ symmetry.

We note the omission of an additional term describing ALP couplings to the Higgs doublet Φ [109]

$$\mathcal{O}^{(5)}_{a\Phi} = \frac{\partial_\mu a}{f}\left(\Phi^\dagger i D^\mu \Phi + \mathrm{h.c.}\right)\,. \quad (2.4.16)$$

This operator can be shown to be redundant, as it can be reduced to the fermionic operators in (2.4.15) using field redefinitions of the Higgs doublet Φ and the chiral fermions ψ. [110]

As the Lagrangian (2.4.15) is defined well above any scale that can be probed in an experiment, we want to obtain a form of it that is relevant at lower energies, that is, below the EWSB scale and even below the QCD scale. In this section, we will outline the steps followed in [17] to derive the effects of running on the axion couplings, as well as the matching conditions at the weak and QCD scales.

We start by noting that the axion-gauge couplings c_{GG}, c_{WW} and c_{BB} as defined in (2.4.15) are scale independent up to 2-loop order, that is

$$\beta\left(c_{VV}(\mu)\right) = 0\,, \quad (2.4.17)$$

with $V = G, W, B$. [111] The Wilson coefficient matrices $\boldsymbol{c}_\psi$ do run however, and their evolution is described by Equations (18) in [17] in the flavour basis, and neglecting all Yukawa coefficients except y_t. One can alternatively redefine the quark fields ψ by rotating them into the mass basis via the chiral rotations (2.2.23); the matrices $\boldsymbol{c}_\psi$ are then also redefined in this mass basis and now follow the RGEs in (24) of [17], or (A.2) in the case of the axion-top coupling defined as $c_{tt} = [\boldsymbol{c}_u]_{33} - [\boldsymbol{c}_q]_{33}$. At this

point it is useful to define the modified axion-gauge couplings,

$$\tilde{c}_{GG} \equiv c_{GG} + \frac{1}{2}\,\mathrm{Tr}\left[\boldsymbol{c}_u + \boldsymbol{c}_d - 2\boldsymbol{c}_q\right] , \tag{2.4.18a}$$

$$\tilde{c}_{WW} \equiv c_{WW} - \frac{1}{2}\,\mathrm{Tr}\left[3\boldsymbol{c}_q + \boldsymbol{c}_l\right] , \tag{2.4.18b}$$

$$\tilde{c}_{BB} \equiv c_{BB} + \mathrm{Tr}\left[\frac{4}{3}\boldsymbol{c}_u + \frac{1}{3}\boldsymbol{c}_d - \frac{1}{6}\boldsymbol{c}_q + \boldsymbol{c}_e - \frac{1}{2}\boldsymbol{c}_l\right] , \tag{2.4.18c}$$

which appear in the RGEs for the axion-fermion couplings, as well as the calculations for several processes where they encapsulate fermion loop corrections to the axion-gauge couplings. These modified axion-gauge couplings are now scale dependent through the presence of the scale dependent $\boldsymbol{c}_\psi$; their evolution at 2-loops is given in Equation (A.1) of [17].

Upon running down to the weak scale $\mu_w \approx m_t$, we express the Lagrangian (2.4.15) in terms of the gauge fields generated by the Higgs mechanism as well as the mass-basis fermion fields,

$$\begin{aligned}\mathcal{L}_a^{(5)}(\mu_w) = \frac{1}{2}(\partial_\mu a)(\partial^\mu a) - \frac{1}{2}m_{a,0}^2 a^2 + \frac{\partial_\mu a}{f}\sum_\psi \left(\bar{\psi}_R \boldsymbol{k}_{\psi_R}\gamma^\mu\psi_R + \bar{\psi}_L \boldsymbol{k}_{\psi_L}\gamma^\mu\psi_L\right) \\ + c_{GG}\frac{\alpha_s}{4\pi}\frac{a}{f}G^a_{\mu\nu}\tilde{G}^{\mu\nu a} + c_{\gamma\gamma}\frac{\alpha}{4\pi}\frac{a}{f}F_{\mu\nu}\tilde{F}^{\mu\nu} \\ + c_{\gamma Z}\frac{\alpha}{2\pi s_w c_w}\frac{a}{f}F_{\mu\nu}\tilde{Z}^{\mu\nu} + c_{ZZ}\frac{\alpha}{4\pi s_w^2 c_w^2}\frac{a}{f}Z_{\mu\nu}\tilde{Z}^{\mu\nu} + c_{WW}\frac{\alpha}{2\pi s_w^2}\frac{a}{f}W^+_{\mu\nu}\tilde{W}^{\mu\nu-} ,\end{aligned} \tag{2.4.19}$$

where we now sum over left- and right-handed fermion fields independently, with the new coupling matrices,[12]

$$\boldsymbol{k}_{u_L} = \boldsymbol{c}_q\,, \quad \boldsymbol{k}_{d_L} = \boldsymbol{V}^\dagger \boldsymbol{c}_q \boldsymbol{V}\,, \quad \boldsymbol{k}_{e_L} = \boldsymbol{k}_{\nu_L} = \boldsymbol{c}_l\,, \quad \boldsymbol{k}_{u_R,d_R,e_R} = \boldsymbol{c}_{u,d,e} \tag{2.4.20}$$

with $\boldsymbol{V}$ the CKM matrix, and the axion-boson couplings defined at the weak scale,

$$c_{\gamma\gamma} = c_{WW} + c_{BB}\,, \quad c_{\gamma Z} = c_w^2 c_{WW} - s_w^2 c_{BB}\,, \quad c_{ZZ} = c_w^4 c_{WW} + s_w^4 c_{BB}\,. \tag{2.4.21}$$

We further define the diagonal axion-fermion couplings by generalising the earlier

[12] Note the different convention, u_L, d_L, e_L, ν_L in this work correspond to U, D, E, ν in [17], and u_R, d_R, e_R correspond to u, d, e.

definition for c_{tt},

$$c_{\psi_i\psi_i} = \left[\boldsymbol{k}_{\psi_R}\right]_{ii} - \left[\boldsymbol{k}_{\psi_L}\right]_{ii} . \tag{2.4.22}$$

The scale evolution for these axion-fermion couplings can directly be obtained from that of the $\boldsymbol{c}_\psi$ couplings mentioned earlier.

As the energy scale drops below the weak scale $\mu \lesssim \mu_w$, approximating $\mu_w \approx m_t \approx m_W \approx m_Z$, we integrate out the $W^\pm$ and Z bosons and the top quark. The resulting Lagrangian will contain the first two lines of (2.4.19) with the t_L and t_R fields omitted from the sum over fermions,

$$\begin{aligned}\mathcal{L}_a^{(5)}(\mu \lesssim \mu_w) = \frac{1}{2}(\partial_\mu a)(\partial^\mu a) - \frac{1}{2}m_{a,0}^2 a^2 + \frac{\partial_\mu a}{f}\sum_{\psi\neq t}\left(\bar{\psi}_R \boldsymbol{k}_{\psi_R}\gamma^\mu\psi_R + \bar{\psi}_L\boldsymbol{k}_{\psi_L}\gamma^\mu\psi_L\right) \\ + c_{GG}\frac{\alpha_s}{4\pi}\frac{a}{f}G^a_{\mu\nu}\tilde{G}^{\mu\nu a} + c_{\gamma\gamma}\frac{\alpha}{4\pi}\frac{a}{f}F_{\mu\nu}\tilde{F}^{\mu\nu} .\end{aligned} \tag{2.4.23}$$

Integrating out these fields then causes matching corrections as loop diagrams such as the ones in Figure 2.8 are absorbed into new effective axion-photon or axion-gluon couplings. Assuming a light ALP and neglecting terms of order $m_a^2/m_{t,W}^2$, these matching corrections at the weak scale are given by

$$\Delta\tilde{c}_{GG}(\mu_w) = -\frac{1}{2}c_{tt}(\mu_w) , \qquad \Delta\tilde{c}_{\gamma\gamma}(\mu_w) = -\frac{4}{3}c_{tt}(\mu_w) , \tag{2.4.24}$$

such that $\tilde{c}_{VV}(\mu \lesssim \mu_w) = \tilde{c}_{VV}(\mu_w) + \Delta\tilde{c}_{VV}(\mu_w)$. Recalling the definitions of the modified axion-gauge couplings (2.4.18), we obtain

$$\tilde{c}_{GG}(\mu \lesssim \mu_w) = c_{GG} + \frac{1}{2}\sum_q c_{qq}(\mu) + \Delta\tilde{c}_{GG}(\mu_w) = c_{GG} + \frac{1}{2}\sum_{q\neq t} c_{qq}(\mu) , \tag{2.4.25a}$$

$$\tilde{c}_{\gamma\gamma}(\mu \lesssim \mu_w) = c_{\gamma\gamma} + \sum_\psi N_c^\psi Q_\psi^2 c_{\psi\psi}(\mu) + \Delta\tilde{c}_{\gamma\gamma}(\mu_w) = c_{\gamma\gamma} + \sum_{\psi\neq t} N_c^\psi Q_\psi^2 c_{\psi\psi}(\mu) , \tag{2.4.25b}$$

where the sum over q (ψ) indicates summing over all quarks (fermions), and note that the matching condition at the weak scale amounts to removing the contribution from the integrated out top quark from the definitions of $\tilde{c}_{VV}$. This matching correction will also apply at lighter fermion mass thresholds. Matching corrections

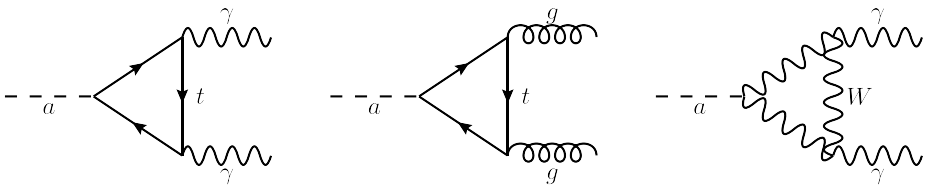

Figure 2.8: Diagrams responsible for the 1-loop matching corrections to the axion-gauge couplings when integrating out the top quark and W boson below the weak scale. Figure reproduced from [17].

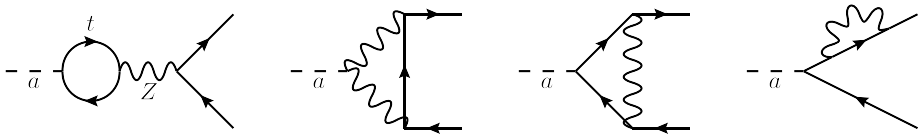

Figure 2.9: Diagrams responsible for the 1-loop matching corrections to the axion-fermion couplings when integrating out the top quark and W and Z bosons below the weak scale. In the second diagram, the boson lines can be WW, ZZ, $Z\gamma$, or γZ; in the third and fourth diagrams, the boson line can be a W or a Z. Figure reproduced from [17].

also occur for the axion-fermion couplings, caused by diagrams such as the ones shown in Figure 2.9. The matching coefficients $\Delta\boldsymbol{k}_{\psi_L}(\mu_w)$ and $\Delta\boldsymbol{k}_{\psi_R}(\mu_w)$ are given in Equation (59) of [17], with an additional CKM dependent coefficient $\hat{\Delta}\boldsymbol{k}_{d_L}(\mu_w)$ given in (60).

The fermion part of the ALP Lagrangian below the weak scale (2.4.23) can be rewritten in terms of non-chiral fermion fields and vector and axial currents. Recalling the definition of the left- and right-handed projectors $P_{L,R}$ we can write

$$\bar{\psi}_R \boldsymbol{k}_{\psi_R} \gamma^\mu \psi_R + \bar{\psi}_L \boldsymbol{k}_{\psi_L} \gamma^\mu \psi_L = \frac{1}{2}\bar{\psi}\left(\boldsymbol{k}_{\psi_R} + \boldsymbol{k}_{\psi_L}\right)\gamma^\mu \psi + \frac{1}{2}\bar{\psi}\left(\boldsymbol{k}_{\psi_R} - \boldsymbol{k}_{\psi_L}\right)\gamma^\mu\gamma^5\psi\,. \tag{2.4.26}$$

Focusing on the diagonal couplings, and remembering that the vector currents are conserved below the weak scale, *i.e.* $\bar{\psi}\gamma^\mu\psi \to 0$, we can rewrite the axion-fermion interactions in terms of the diagonal couplings (2.4.22),

$$\mathcal{L}_a^{(5)}(\mu \lesssim \mu_w) \supset \frac{\partial_\mu a}{f} \sum_{\psi \neq t} \frac{c_{\psi\psi}}{2} \bar{\psi}\gamma^\mu\gamma^5\psi\,, \tag{2.4.27}$$

where we sum over non-chiral fields.

Below the weak scale, the RGEs for the axion-gauge couplings and axion-fermion couplings are greatly simplified. The scale dependence of the coefficients $\tilde{c}_{\gamma\gamma}$ and $\tilde{c}_{GG}$ only arises at 2-loop order below the weak scale and is therefore very weak; at next-to-leading logarithmic order, it can be neglected and the axion-gauge couplings taken to be scale-independent. We nevertheless reiterate the matching procedure as the energy scale crosses various fermion mass thresholds, and generalise (2.4.25),

$$\tilde{c}_{GG}(\mu) = c_{GG} + \frac{1}{2}\sum_q c_{qq}(\mu)\,\Theta(\mu - m_q)\,, \tag{2.4.28a}$$

$$\tilde{c}_{\gamma\gamma}(\mu) = c_{\gamma\gamma} + \sum_\psi N_c^\psi Q_\psi^2 c_{\psi\psi}(\mu)\,\Theta(\mu - m_\psi)\,, \tag{2.4.28b}$$

where $\Theta(x)$ is the Heaviside step function. The evolution for the axion-fermion couplings can now only be built from diagrams involving gluon and photon loops (still setting the light quark Yukawas to zero), and must therefore be flavour diagonal. The RGEs for the axion-fermion coupling matrices $\boldsymbol{k}_\psi$ are given in Equation (75) of [17], and are indeed diagonal in flavour space. Then, the flavour changing couplings can be taken to be scale-independent, while only the flavour diagonal couplings $c_{\psi_i\psi_i}$ will run.

The final step of the matching procedure involves matching the theory onto the χPT Lagrangian as the energy scale reaches the QCD scale $\mu = \Lambda_{\rm QCD}$. The detail of the procedure is beyond the scope of this work but is discussed at length in Section 7 of [17]. We nevertheless quote the result for the physical ALP mass, given by the explicit mass parameter $m_{a,0}$ and a contribution from the chiral Lagrangian [101, 112, 113], such that

$$m_a^2 = m_{a,0}^2\left[1 + \frac{f_\pi^2}{8f^2}\frac{m_\pi^2 m_{a,0}^2}{\left(m_\pi^2 - m_{a,0}^2\right)}\left(\Delta c_{ud}\right)^2\right] + c_{GG}^2\frac{f_\pi^2 m_\pi^2}{f^2}\frac{2m_u m_d}{\left(m_u + m_d\right)^2} + O\left(\frac{f_\pi^4}{f^4}\right)\,, \tag{2.4.29}$$

with m_π the neutral pion π^0 mass and the parameter

$$\Delta c_{ud} = c_{uu} - c_{dd} + 2c_{GG}\frac{m_d - m_u}{m_d + m_u}\,. \tag{2.4.30}$$

We additionally quote the resulting axion-nucleon axial couplings, [114]

$$g_p = g_0 \left(c_{uu} + c_{dd} + 2c_{GG}\right) + g_A \frac{m_\pi^2}{m_\pi^2 - m_a^2} \Delta c_{ud} \,, \tag{2.4.31a}$$

$$g_n = g_0 \left(c_{uu} + c_{dd} + 2c_{GG}\right) - g_A \frac{m_\pi^2}{m_\pi^2 - m_a^2} \Delta c_{ud} \,, \tag{2.4.31b}$$

for an interaction of the form $\frac{g_N}{4} \frac{\partial_\mu a}{f} \bar{N} \gamma^\mu \gamma^5 N$, with the isovector $g_0 = 0.440(44)$ [115, 116] and isoscalar g_A couplings. All parameters involved in these definitions are evaluated at the QCD scale Λ_{QCD}. Further details on the chiral Lagrangian in the presence of an ALP field are given as necessary in Section 3.2.

Chapter 3

Fifth Forces

The methods for DM detection described in Section 2.3.2 rely on the presence of DM particles as an external background state, either through its relic abundance, or through production via an external source. Another indirect detection method uses the scattering of two SM particles via the exchange of virtual particles. Such processes form the macroscopic forces corresponding to each fundamental interaction, the most common example being that of the electromagnetic Coulomb force originating from exchanges of virtual photons. These forces can be mediated by any particle, with a characteristic range dependent on the mediator's mass. In the case of BSM particles, we call these *fifth forces*. We emphasize however, that since the BSM states are purely virtual, fifth forces are not sensitive to a DM background[1], and are not strictly purely DM detection tools.

Fifth forces are parameterised by a potential derived from the S-matrix element of the interaction pictured in Figure 3.1. These potentials are functions of the separation r between the two interacting SM particles and are calculated by taking the Fourier Transform (FT) of the scattering amplitude

$$V(r) = \int \frac{\mathrm{d}^3\boldsymbol{q}}{(2\pi)^3}\mathcal{A}(q)e^{i\boldsymbol{q}\cdot\boldsymbol{r}}\,, \tag{3.0.1}$$

[1]Breaking the loop with external thermal propagators can yield a modified force that is sensitive to thebackground density, see for example [117–119].

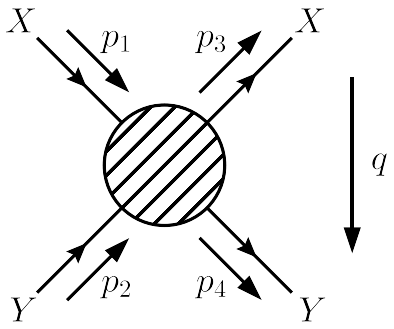

Figure 3.1: Generic $XY \to XY$ diagram responsible for fifth forces interactions. The momentum convention shown here is the one used all throughout this work.

with $\mathcal{A}$ the Non-Relativistic (NR) limit of the matrix element $\mathcal{M}$, and q the transferred momentum. To avoid confusion with quantum field potentials appearing in QFT, we will call these *Interaction Potentials (IPs)*.

3.1 Interaction Potentials

3.1.1 The One-Pion Exchange Potential

The simplest type of IP is the Yukawa potential, arising from the exchange of a single scalar particle. To keep things interesting, we will instead derive the form of the slightly more complicated One-Pion Exchange (OPE) IP, which arises as the main component of the residual nuclear force binding atomic nuclei [120]. We consider an effective interaction between a neutral pseudoscalar π^0 and two nucleons N,

$$\mathcal{O}_{\pi N} = g\frac{\partial_\mu \pi^0}{f}\bar{N}\gamma^\mu\gamma^5 N\,, \tag{3.1.1}$$

with f the energy scale of the effective interaction. The diagram responsible for the four-nucleon scattering via exchange of a single neutral pion is shown in Figure 3.2. The corresponding matrix amplitude is then

$$i\mathcal{M} = -i\frac{g^2}{f^2}\left[\bar{u}(p_2)\gamma^\mu\gamma^5 u(p_1)\right]\frac{q_\mu q_\nu}{q^2 - m_\pi^2}\left[\bar{u}(p_4)\gamma^\nu\gamma^5 u(p_3)\right]\,, \tag{3.1.2}$$

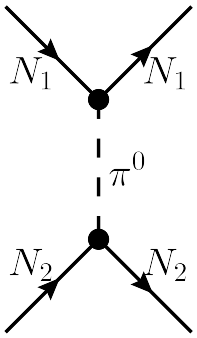

Figure 3.2: Interaction responsible for the OPE potential.

with the transferred momentum $q \equiv p_1 - p_2 = p_4 - p_3$. Plugging in one of the NR spinor identities given in Appendix A and taking out the relativistic normalisation factor $4m_N^2$ gives the NR amplitude

$$\mathcal{A} = \frac{g^2}{f^2} \frac{(\boldsymbol{q} \cdot \boldsymbol{\sigma}_1)(\boldsymbol{q} \cdot \boldsymbol{\sigma}_2)}{|\boldsymbol{q}|^2 + m_\pi^2} \,. \tag{3.1.3}$$

Plugging this amplitude into the FT defined in (3.0.1) and evaluating it using the basis defined in [121] for spin-dependent IPs gives the OPE potential

$$\begin{aligned} V_{\mathrm{OPE}}(r) &= -\frac{g^2}{f^2} \frac{1}{4\pi r^3} e^{-m_\pi r} \\ &\quad \times \left[(1 + m_\pi r) \, (\boldsymbol{\sigma}_1 \cdot \boldsymbol{\sigma}_2) - \left(3 + 3m_\pi r + (m_\pi r)^2 \right) (\hat{\boldsymbol{r}} \cdot \boldsymbol{\sigma}_1) \, (\hat{\boldsymbol{r}} \cdot \boldsymbol{\sigma}_2) \right] \\ &= \frac{g^2}{4\pi} \frac{m_\pi^2}{f^2} \frac{1}{3} m_\pi \left[\frac{e^{-m_\pi r}}{m_\pi r} \, (\boldsymbol{\sigma}_1 \cdot \boldsymbol{\sigma}_2) + \left(1 + \frac{3}{m_\pi r} + \frac{3}{(m_\pi r)^2} \right) \frac{e^{-m_\pi r}}{m_\pi r} S_{12} \right] , \end{aligned} \tag{3.1.4}$$

where in the second line we have defined $S_{ij} \equiv 3(\hat{\boldsymbol{r}} \cdot \boldsymbol{\sigma}_i)(\hat{\boldsymbol{r}} \cdot \boldsymbol{\sigma}_j) - \boldsymbol{\sigma}_i \cdot \boldsymbol{\sigma}_j$. This result is exactly the form of the OPE IP given in [120] and showcases the general process to obtain IPs.

3.1.2 Potentials from Pair Exchange

As we saw in the previous section, the exchange of a single pseudoscalar particle yields a spin-dependent potential. To obtain a spin-independent IP, we must consider the next order in perturbation theory: the exchange of two particles via a

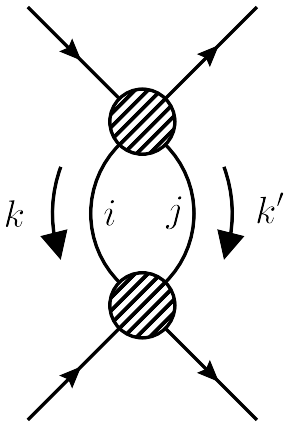

Figure 3.3: Generic 1-loop diagram responsible for pair exchange IPs.

loop, such as the one shown in Figure 3.3. Furthermore, in other cases such as an interaction with a fermion mediator, pair exchange is the leading order process that generates an IP. We must therefore extend the method we used to calculate IPs from single particle exchanges to pair exchanges.

Naively taking the FT of a loop amplitude is impossible for any case of interest, and so most, if not all, methods of calculations for IPs rely on using some variation of the optical theorem and discontinuities of the amplitude. [122–127] For our calculation, we will follow the method from [123] where they show, using Cauchy's theorem, that an IP can be calculated via

$$V(r) = \frac{1}{4\pi^2 r}\int_{(m_i+m_j)^2}^{\infty} \mathrm{d}t\ \rho(s,t)e^{-\sqrt{t}r}\,, \tag{3.1.5}$$

with $\rho(s,t)$ the spectral density function, defined as $\rho(s,t) \equiv [\mathcal{M}]_t/2i$, where

$$[\mathcal{M}(s,t)]_t \equiv \mathcal{M}(s,t+i\epsilon) - \mathcal{M}(s,t-i\epsilon) \tag{3.1.6}$$

is the discontinuity of the amplitude $\mathcal{M}$ along the t branch cut.

To compute the discontinuity for a given process, we can use Cutkosky's theorem [128], which states that the discontinuity along t of an amplitude can be found by

replacing the propagators running along t by their own discontinuity

$$\frac{1}{k^2 - m^2 + i\epsilon} \to (-2\pi i)\Theta\left(k^0\right)\delta\left(k^2 - m^2\right) , \tag{3.1.7}$$

where $\Theta(x)$ is the Heaviside step function as before. For example, a diagram like the one in Figure 3.3 will yield a scalar loop integral of the form

$$I_s(\mathcal{P}) = \int \frac{\mathrm{d}^4k}{(2\pi)^4}\frac{\mathrm{d}^4k'}{(2\pi)^4}\frac{1}{k^2 - m_i^2}\frac{1}{k'^2 - m_j^2}\,\mathcal{P}(q,k,k';p_i)\;(2\pi)^4\delta^{(4)}\left(q - k - k'\right) \tag{3.1.8}$$

where $\mathcal{P}$ is a generic function of any momentum involved; its discontinuity along t is then given by

$$\begin{aligned}[I_s(\mathcal{P})]_t = -\frac{1}{4\pi^2}\int \mathrm{d}^4k\,\mathrm{d}^4k'\;\mathcal{P}(q,k,k';p_i)\;\delta^{(4)}\left(Q - k - k'\right)\\ \times\Theta\left(k^0\right)\delta\left(k^2 - m_i^2\right)\Theta\left(k'^0\right)\delta\left(k'^2 - m_j^2\right) .\end{aligned} \tag{3.1.9}$$

Six of the eight integrals above can be trivially computed using the delta functions available. To perform these, we use the "q rest frame" where we set $q = (q^0, \mathbf{0})$, and start by expanding $k = (E_k, \boldsymbol{k})$ and $k' = (E'_k, \boldsymbol{k}')$ in terms of their components to obtain

$$\begin{aligned}[I_s(\mathcal{P})]_t = -\frac{1}{4\pi^2}\int \mathrm{d}E_k\mathrm{d}^3\boldsymbol{k}\,\mathrm{d}E'_k\mathrm{d}^3\boldsymbol{k}'\;\mathcal{P}(q,k,k';p_i)\;\delta\left(q^0 - E_k - E'_k\right)\delta^{(3)}\left(\boldsymbol{k} + \boldsymbol{k}'\right)\\ \times\Theta\left(E_k\right)\delta\left(E_k^2 - |\boldsymbol{k}|^2 - m_i^2\right)\Theta\left(E'_k\right)\delta\left(E_k'^2 - |\boldsymbol{k}'|^2 - m_j^2\right) .\end{aligned} \tag{3.1.10}$$

The E_k and E'_k integrals can be computed via the delta-function identity (2.1.10), using the step functions to select the positive solution. The $\boldsymbol{k}'$ integral is performed using the 3-dimensional delta function, leaving

$$\begin{aligned}[I_s(\mathcal{P})]_t = -\frac{1}{16\pi^2}\int \mathrm{d}^3\boldsymbol{k}\;\frac{1}{\sqrt{|\boldsymbol{k}|^2 + m_i^2}\sqrt{|\boldsymbol{k}|^2 + m_j^2}}\,\mathcal{P}(q,k,k';p_i)\\ \times\delta\left(q^0 - \sqrt{|\boldsymbol{k}|^2 + m_i^2} - \sqrt{|\boldsymbol{k}|^2 + m_j^2}\right) .\end{aligned} \tag{3.1.11}$$

Again using the identity (2.1.10), we can perform the integral over the $|\boldsymbol{k}|$ component of the $\boldsymbol{k}$ vector integral, leaving only an angular integral over the function of

momenta $\mathcal{P}$,

$$[I_s(\mathcal{P})]_t = -\frac{1}{8\pi}\frac{\sqrt{\tau}}{\sqrt{t}}\frac{\sqrt{t-\delta m^2}}{\sqrt{t}}\int\frac{\mathrm{d}^2\Omega}{4\pi}\,\mathcal{P}(q,k,k';p_i)\,, \tag{3.1.12}$$

where we have defined the mass difference $\delta m \equiv m_i - m_j$ and the parameter $\tau \equiv t-(m_i+m_j)^2$, and used the Mandelstam variable $t \equiv q^2 = \left(q^0\right)^2$ to express the result in terms of Lorentz invariant quantities.

The above derivation and result are very similar to the derivation of the two-particle phase space done earlier in Section 2.1.1. This similarity can be understood via the optical theorem: it states that the imaginary part of a loop amplitude $XY \to \{Z_i\} \to XY$ can be related to the cut amplitude $XY \to \{Z_i\}$, where $\{Z_i\}$ represents an n-particle state [5]. In other words, it allows us to transform a loop integral into an n-body phase space integration such as (2.1.7), which is precisely what we have done above.

All angular dependence in (3.1.12) will come from the 3-momenta $\boldsymbol{k}$, $\boldsymbol{p}$ and $\boldsymbol{p}'$ appearing via dot products in various momentum contractions (see Appendix B.1). The resulting angular integrals are analytically solvable but not trivial; we define a basis of functions

$$\mathcal{I}^{(a,b)} = \int\frac{\mathrm{d}^2\Omega}{4\pi}\,\left(Y+Z\hat{\boldsymbol{k}}\cdot\hat{\boldsymbol{p}}\right)^a\left(Y'+Z'\hat{\boldsymbol{k}}\cdot\hat{\boldsymbol{p}}'\right)^b\,, \tag{3.1.13}$$

with $a,b\in\mathbb{Z}$, based on the one used in [129]. The solutions of the most common of these angular integrals are given in Appendix B.2; additional solutions may be found in the reference above. In these solutions appears the parameter y defined as

$$y \equiv \hat{\boldsymbol{p}}\cdot\hat{\boldsymbol{p}}' = -\frac{2s+\frac{1}{2}(\tau_1+\tau_2)}{\sqrt{\tau_1}\sqrt{\tau_2}}\,, \tag{3.1.14}$$

with $\tau_{1,2} \equiv t - 4M_{1,2}^2$ where M_1 and M_2 are the external fermion masses.

This method to solve for the discontinuities of scalar integrals is easily extendable to vector I^μ and tensor $I^{\mu\nu}$ integrals using Passarino-Veltman (PV) reduction [130]. We generate several scalar integrals by considering all possible contractions of the vector/tensor integral with the external momenta entering $\mathcal{P}(p)$, and then solve

these using the method described above. Since there are 3 independent external momenta, we will have to solve at most 3 or 10 contractions for vector and tensor integrals respectively.

The final step of the calculation is to plug the result for the NR amplitude discontinuity $\mathcal{A}$ into (3.1.5) and perform the t integration. Unfortunately, the most general case, an arbitrary function of t, $m_{i,j}$ and $M_{1,2}$, is not solvable analytically. However, there exists a useful case when both particles in the loop have the same mass $m_i = m_j = m$ (*i.e.* we take $\delta m = 0$): if we can write the amplitude as a polynomial in t and $\tau = t - 4m^2$ then, using the definition of the modified Bessel functions of the second kind $K_\nu(x)$ [131], we can show that

$$\int_{4m^2}^{\infty} \mathrm{d}t \, \frac{\sqrt{\tau}}{\sqrt{t}} \, t^k \tau^l e^{-r\sqrt{t}} = \frac{2}{\sqrt{\pi}} \left(\frac{4m}{r}\right)^{k+l+1} \sum_{i=0}^{k} \binom{k}{i} \Gamma\left(l + i + \frac{3}{2}\right) (mr)^{k-i} \, K_{l+i+1}(2mr) \,, \quad (3.1.15)$$

with $k \geq 0$ and $l \geq -1$ integers, $\binom{k}{i}$ the binomial coefficient k choose i, and $\Gamma(x)$ the gamma function.

3.1.3 The Neutrino IP

We illustrate the method described by computing the potential between two fermions arising from the exchange of a pair of neutrinos. The relevant interaction term is Fermi's 4-fermion interaction,

$$\mathcal{O}_{\text{Fermi}} = \frac{G_F}{2\sqrt{2}} \left[\bar{\nu}_i \gamma^\mu (1 - \gamma^5) \nu_j\right] \left[\bar{\psi} \gamma_\mu \left(g_{ij}^V - g_{ij}^A \gamma^5\right) \psi\right] \quad (3.1.16)$$

for Dirac neutrinos. Here G_F is the Fermi constant and $i, j \in \{1, 2, 3\}$ denote the neutrino mass eigenstates. For quarks, the couplings g_{ij}^V and g_{ij}^A are simply the vector and axial couplings, respectively

$$\left[g_{ij}^V\right]_q = \delta_{ij} g_q^V \quad \text{and} \quad \left[g_{ij}^A\right]_q = \delta_{ij} g_q^A \,. \quad (3.1.17)$$

For leptons, operators of the type $(\bar{\nu}l)(\bar{l}\nu)$ arising from charged-current interactions can be recast onto the form (3.1.16) via a Fierz transformation, giving the effective couplings

$$\left[g_{ij}^V\right]_l = \delta_{ij} g_l^V + U_{li}^* U_{lj} \quad \text{and} \quad \left[g_{ij}^A\right]_l = \delta_{ij} g_l^A + U_{li}^* U_{lj}\,, \tag{3.1.18}$$

where U_{li} are entries of the Pontecorvo-Maki-Nakagawa-Sakata (PMNS) matrix describing neutrino-sector flavour violation. The vector and axial fermion couplings are given by

$$g_f^V = \frac{1}{2}\tau_f^3 - Q_f s_w^2 \quad \text{and} \quad g_f^A = \frac{1}{2}\tau_f^3\,. \tag{3.1.19}$$

The matrix element corresponding to the exchange can be written

$$i\mathcal{M}_{ij} = G_F^2 \left[\bar{u}(p_3)\gamma_\mu \left(g_{ij}^V - g_{ij}^A\gamma^5\right) u(p_1)\right] \left[\bar{u}(p_4)\gamma_\nu \left(g_{ij}^V - g_{ij}^A\gamma^5\right) u(p_2)\right] \cdot I^{\mu\nu}\,, \tag{3.1.20}$$

with

$$I^{\mu\nu} = \int \frac{\mathrm{d}^4k}{(2\pi)^4}\frac{\mathrm{d}^4k'}{(2\pi)^4} \frac{g^{\mu\nu}k\cdot k' - k'^\mu k^\nu - k^\mu k'^\nu + i\varepsilon^{\mu\nu\alpha\beta}k_\alpha k'_\beta}{(k^2 - m_i^2)(k'^2 - m_j^2)} (2\pi)^4\delta^{(4)}\left(q - k - k'\right)\,. \tag{3.1.21}$$

The only external momentum entering $I^{\mu\nu}$ is q, therefore using PV reduction we can write $I^{\mu\nu} = I_{qq}q^\mu q^\nu + I_g g^{\mu\nu}$, with

$$I_{qq} = \frac{4q_\mu q_\nu I^{\mu\nu} - t g_{\mu\nu}I^{\mu\nu}}{3t^2} \quad \text{and} \quad I_g = \frac{t g_{\mu\nu}I^{\mu\nu} - q_\mu q_\nu I^{\mu\nu}}{3t}\,, \tag{3.1.22}$$

where the two contractions entering the scalar integrals are

$$q_\mu q_\nu I^{\mu\nu} = \int \frac{\mathrm{d}^4k}{(2\pi)^4}\frac{\mathrm{d}^4k'}{(2\pi)^4} \frac{tk\cdot k' - 2(q\cdot k)(q\cdot k')}{(k^2 - m_i^2)(k'^2 - m_j^2)} (2\pi)^4\delta^{(4)}\left(q - k - k'\right)\,, \tag{3.1.23}$$

$$g_{\mu\nu}I^{\mu\nu} = \int \frac{\mathrm{d}^4k}{(2\pi)^4}\frac{\mathrm{d}^4k'}{(2\pi)^4} \frac{2k\cdot k'}{(k^2 - m_i^2)(k'^2 - m_j^2)} (2\pi)^4\delta^{(4)}\left(q - k - k'\right)\,. \tag{3.1.24}$$

We take the discontinuities of these integrals using (3.1.12), evaluate the scalar products using the components given in Appendix B.1, and solve for $I^{\mu\nu}$ to obtain

$$\begin{aligned}\left[I^{\mu\nu}\right]_t = \frac{1}{16\pi}\frac{\sqrt{\tau}}{\sqrt{t}}\frac{\sqrt{\tau_\delta}}{\sqrt{t}}\left(\frac{\tau}{t} + \frac{\tau_\delta}{t} - \frac{4}{3}\frac{\tau\tau_\delta}{t^2}\right) q^\mu q^\nu \\ - \frac{1}{32\pi}\frac{\sqrt{\tau}}{\sqrt{t}}\frac{\sqrt{\tau_\delta}}{\sqrt{t}}\left(\tau + \tau_\delta - \frac{2}{3}\frac{\tau\tau_\delta}{t}\right) g^{\mu\nu}\,,\end{aligned} \tag{3.1.25}$$

where we have defined $\tau_\delta = t - (\delta m)^2$. The integral in (3.1.5) is not solvable analytically for the corresponding general matrix element $\mathcal{M}_{ij}$; however, we can consider the diagonal elements $\mathcal{M}_{ii}$ such that $m_j = m_i$ and $\tau_\delta = t$. In the NR limit, using the spinor contractions from Appendix A, we find the diagonal amplitude

$$\mathcal{A}_{ii} = -\frac{G_F^2}{16\pi i}\left[\left(g_1^V\right)_{ii}\delta^0_\mu - \left(g_1^A\right)_{ii}\delta^j_\mu\sigma_{1j}\right]\left[\left(g_2^V\right)_{ii}\delta^0_\nu - \left(g_2^A\right)_{ii}\delta^k_\nu\sigma_{2k}\right] \times \frac{\sqrt{\tau}}{\sqrt{t}}\left[\frac{1}{2}\left(t+\frac{1}{3}\tau\right)g^{\mu\nu} - \left(\frac{2}{3}+\frac{4}{3}\frac{m_i^2}{t}\right)q^\mu q^\nu\right]. \quad (3.1.26)$$

Finally, using (3.1.15) to perform the integrals and identifying $\boldsymbol{q} \to -i\nabla$ in the Fourier transform, we obtain

$$V_{ii}(r) = \frac{G_F^2}{16\pi^3}\Bigg(\left(g_1^V\right)_{ii}\left(g_2^V\right)_{ii}\frac{1}{r^5}\left[(m_i r)^3 K_3(2m_i r)\right] + \left(g_1^A\right)_{ii}\left(g_2^A\right)_{ii}\Bigg\{-(\boldsymbol{\sigma}_1\cdot\boldsymbol{\sigma}_2)\frac{1}{r^5}\left[(m_i r)^3 K_3(2m_i r)\right] + (\boldsymbol{\sigma}_1\cdot\nabla)(\boldsymbol{\sigma}_2\cdot\nabla)\left(\frac{1}{6r^3}\left[2m_i r K_1(2m_i r)\right] + \frac{1}{3r}m_i^2 F(2m_i r)\right)\Bigg\}\Bigg), \quad (3.1.27)$$

where we have used recurrence relations of Bessel functions to simplify the result, defined

$$F(x) \equiv \int_1^\infty \mathrm{d}y\, \frac{\sqrt{y^2-1}}{y^2}e^{-xy}, \quad (3.1.28)$$

and normalised the result such that the quantities in square brackets tend to 1 in the massless neutrino limit. As such, in this limit, the spin-independent term of the potential exactly matches the well-known result [132,133]. The full result, including mass dependency and spin-dependent terms, agrees with that in [134], up to the term containing the $F(x)$ function.

3.2 Fifth Forces for ALPs

Fifth forces have been identified as potential probes for axions very early on [135]. The early focus was on spin-dependent interactions, which are the consequence of the exchange of a single light CP odd scalar, such as the pion in the OPE potential seen in Section 3.1.1. The leading contribution to a spin-independent long-range

force mediated by axions is generated by axion-pair exchange at one loop [136] and therefore similarly suppressed as the neutrino IP seen earlier. The potential corresponding to the exchange of a pair of neutrinos scales as $V(r) \sim 1/r^5$, as does the potential generated by the exchange of pairs of massless axions [136, 137]. In contrast, the exchange of pairs of pseudoscalars scales as $V(r) \sim 1/r^3$, whereas the potential for the axion-Higgs portal we will introduce in Chapter 4 scales as $V(r) \sim 1/r^7$ [138]. The difference between the potentials induced by pseudoscalars and axions is a consequence of the manifest shift-symmetry that protects all linear axion interactions and has been discussed in the case of the pion in very early literature [139–142].

3.2.1 Derivative vs. Mass Bases

We recall the general form of the Lagrangian for an interaction between an ALP and a SM fermion below the weak scale from (2.4.27), and write the relevant terms of the ALP Lagrangian (2.4.23),

$$\mathcal{L}_a^{(5)} \supset \frac{1}{2}\bar{\psi} i \overleftrightarrow{\partial\!\!\!/} \psi + \frac{1}{2}(\partial_\mu a)(\partial^\mu a) - M_\psi \bar{\psi}\psi - \frac{1}{2} m_a^2 a^2 + \frac{\partial_\mu a}{f}\frac{c_\psi}{2}\bar{\psi}\gamma^\mu\gamma^5\psi\,, \tag{3.2.1}$$

that we wrote in terms of the physical axion mass m_a defined in (2.4.29), and we sum over any fermion d.o.f.

We can use a chiral rotation to rescale the fermion fields by $\psi \to e^{ic_\psi a\gamma^5/f}\psi$ as defined earlier (we will ignore the anomalous $F\tilde{F}$ terms for this section). This allows us to absorb the axion-fermion coupling into the fermion kinetic term, at the cost of creating an axion dependency in the mass term,

$$\mathcal{L}_a^{(5)} \supset \frac{1}{2}\bar{\psi} i \overleftrightarrow{\partial\!\!\!/} \psi + \frac{1}{2}(\partial_\mu a)(\partial^\mu a) - M_\psi \bar{\psi} e^{2ic_\psi a\gamma^5/f}\psi - \frac{1}{2} m_a^2 a^2\,. \tag{3.2.2}$$

Equating the two forms of the Lagrangian and expanding in $1/f$ we obtain two equivalent forms for the axion-fermion interaction operator,

$$\frac{c_\psi}{2}\frac{\partial_\mu a}{f}\bar{\psi}\gamma^\mu\gamma^5\psi = -i m_\psi c_\psi \frac{a}{f}\bar{\psi}\gamma^5\psi + 2 m_\psi c_\psi^2 \frac{a^2}{2f^2}\bar{\psi}\psi + O\left(\frac{a^3}{f^3}\right)\,. \tag{3.2.3}$$

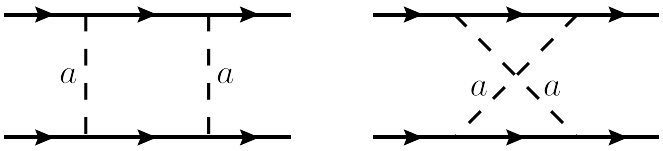

Figure 3.4: Box-type diagrams responsible for the axion IP.

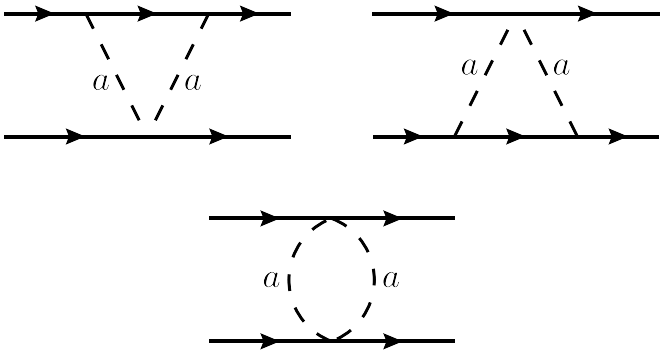

Figure 3.5: Triangle- and bubble-type diagrams appearing as extra contributions to the 1-loop IP when including the quartic vertex appearing in the mass basis.

Naively, we expect the terms linear in a/f on both sides of the equation above to be equivalent, however they lead to contradicting results for processes with more than one axion involved. The reason for this is that the divergence of the axial-vector current, or equivalently the equations of motions for the axion only capture terms up to linear order in the fields. A consistent rescaling of the fermion fields generates the higher order terms in a/f seen on the right-hand side of (3.2.3) that precisely account for the difference between results obtained from the two $O(1/f)$ terms. Notably, the axion pair exchange, which is order $O(1/f^4)$, is represented by the box diagrams in Figure 3.4 when only allowing interactions linear in the axion field; however, when including contributions from the term quadratic in a, bubble and triangle type diagrams as shown in Figure 3.5 will be generated.

For discussions involving this type of interaction, we will designate the interaction operator on the left-hand side of (3.2.3) as the "derivative basis", and the operators in the expansion on the right-hand side as the "mass basis".

3.2.2 Deriving the Axion IP

We now present the derivation of the spin-independent axion pair exchange IP. This will closely follow the similar derivation of pseudoscalar IPs presented in [143], but includes non-zero axion mass effects.

For the vector and tensor integrals that we will encounter in triangle- and box-type diagrams from Figures 3.5 and 3.4 respectively, we use PV reduction with the external momenta basis

$$P_1 \equiv p_1 + p_3 \ , \quad P_2 \equiv p_2 + p_4 \quad \text{and} \quad q \, . \tag{3.2.4}$$

A useful property of this basis is that we have $P_1 \cdot q = P_2 \cdot q = 0$, greatly simplifying the contractions when solving PV equations. Additionally, using the equations of motion we can show that $\bar{u}(p_3)\not{q}u(p_1) = \bar{u}(p_4)\not{q}u(p_2) = 0$, meaning we will not have to consider components of the integrals proportional to q^μ since they will always vanish in the amplitude when contracted against the spinors.

We start by building the Compton amplitude corresponding to the tree-level $\psi a \to \psi a$ scattering process. Using the derivative basis operator, this corresponds to the two diagrams shown in Figure 3.6; after some simplifications using the equations of motion, the matrix amplitude can be written as

$$\mathcal{M}_C^d(p_{\rm in}, p_{\rm out}; k, k') = \frac{c_\psi^2}{4f^2} 4M_\psi^2 \, \bar{u}(p_{\rm out}) \left[\frac{\not{k}}{k^2 + 2p_{\rm in}\cdot k} + \frac{\not{k}'}{k'^2 + 2p_{\rm in}\cdot k'} - \frac{1}{M_\psi} \right] u(p_{\rm in}) \, . \tag{3.2.5}$$

Similarly, in the mass basis, the amplitude corresponding to the two diagrams in Figure 3.6, plus the four-point vertex induced by the $O(1/f^2)$ term in (3.2.3), is

$$\mathcal{M}_C^m(p_{\rm in}, p_{\rm out}; k, k') = \frac{c_\psi^2}{4f^2} 4M_\psi^2 \, \bar{u}(p_{\rm out}) \left[\frac{\not{k}}{k^2 + 2p_{\rm in}\cdot k} + \frac{\not{k}'}{k'^2 + 2p_{\rm in}\cdot k'} \right] u(p_{\rm in}) - 4M_\psi \frac{c_\psi^2}{4f^2} \, \bar{u}(p_{\rm out}) u(p_{\rm in}) \, , \tag{3.2.6}$$

which is exactly equal to the matrix amplitude in the derivative basis $\mathcal{M}_C^d$ that we wrote above, up to order $1/f^3$.

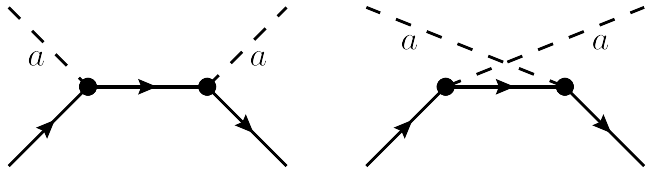

Figure 3.6: Tree-level diagrams involved in the $\psi a \to \psi a$ Compton amplitude.

The amplitude associated with the exchange of two axions is then

$$i\mathcal{M} = \frac{1}{2}\int \frac{\mathrm{d}^4k}{(2\pi)^4}\frac{\mathrm{d}^4k'}{(2\pi)^4}\,(2\pi)^4\delta^{(4)}\left(q-k-k'\right)\frac{i}{k^2-m_a^2}\frac{i}{k'^2-m_a^2} \times \mathcal{M}_C^d(p_1,p_3;-k,-k')\mathcal{M}_C^d(p_2,p_4;k,k')\,. \quad (3.2.7)$$

Replacing the Compton amplitudes by their expressions and using (3.1.12), we write the discontinuity of the matrix amplitude as

$$\begin{aligned}[\mathcal{M}]_t = i\frac{c_{\psi_1}^2 c_{\psi_2}^2}{2f^4}M_1^2M_2^2\Bigg\{&\left[\bar{u}(p_3)\gamma_\mu u(p_1)\right]\left[\bar{u}(p_4)\gamma_\nu u(p_2)\right]\times\left[I_{\mathrm{box}}^{\mu\nu}\right]_t\\ &-\frac{1}{M_2}\left[\bar{u}(p_3)\gamma_\mu u(p_1)\right]\left[\bar{u}(p_4)u(p_2)\right]\times\left[I_{\mathrm{tri.1}}^{\mu}\right]_t\\ &-\frac{1}{M_1}\left[\bar{u}(p_3)u(p_1)\right]\left[\bar{u}(p_4)\gamma_\nu u(p_2)\right]\times\left[I_{\mathrm{tri.2}}^{\nu}\right]_t\\ &+\frac{1}{M_1M_2}\left[\bar{u}(p_3)u(p_1)\right]\left[\bar{u}(p_4)u(p_2)\right]\left(-\frac{1}{8\pi}\frac{\sqrt{\tau}}{\sqrt{t}}\right)\Bigg\}, \end{aligned} \quad (3.2.8)$$

where we have defined the angular integrals

$$\left[I_{\mathrm{box}}^{\mu\nu}\right]_t = -\frac{1}{8\pi}\frac{\sqrt{\tau}}{\sqrt{t}}\int\frac{\mathrm{d}^2\Omega}{4\pi}\,\frac{k^\mu k^\nu}{\mathcal{D}_1\mathcal{D}_2} \quad \text{and} \quad \left[I_{\mathrm{tri.1,2}}^{\mu}\right]_t = -\frac{1}{8\pi}\frac{\sqrt{\tau}}{\sqrt{t}}\int\frac{\mathrm{d}^2\Omega}{4\pi}\,\frac{k^\mu}{\mathcal{D}_{1,2}}\,, \quad (3.2.9)$$

with the terms in the denominators

$$\frac{1}{\mathcal{D}_1} = \left(-\frac{1}{k^2-2p_1\cdot k}+\frac{1}{k'^2-2p_1\cdot k'}\right) = -2\left(\frac{1}{\mathrm{T}+\sqrt{\tau\tau_1}\hat{\boldsymbol{k}}\cdot\hat{\boldsymbol{p}}}+\frac{-1}{\mathrm{T}-\sqrt{\tau\tau_1}\hat{\boldsymbol{k}}\cdot\hat{\boldsymbol{p}}}\right), \quad (3.2.10a)$$

$$\frac{1}{\mathcal{D}_2} = \left(\frac{1}{k^2+2p_2\cdot k}-\frac{1}{k'^2+2p_2\cdot k'}\right) = -2\left(\frac{1}{\mathrm{T}+\sqrt{\tau\tau_2}\hat{\boldsymbol{k}}\cdot\hat{\boldsymbol{p}}'}+\frac{-1}{\mathrm{T}-\sqrt{\tau\tau_2}\hat{\boldsymbol{k}}\cdot\hat{\boldsymbol{p}}'}\right), \quad (3.2.10b)$$

and the shorthand notations $\tau \equiv t-4m_a^2$, $\tau_{1,2}\equiv t-4M_{1,2}^2$, and $\mathrm{T}\equiv t-2m_a^2$. In the

definitions for $\mathcal{D}_{1,2}$, we have used the kinematics defined in Appendix B.1 to express them in terms directly useable in the angular integrals defined in (3.1.13).

We start with the angular integrals $I^{\mu}_{\text{tri.1}}$ and $I^{\nu}_{\text{tri.2}}$. To solve these, we use PV reduction over the basis $\{P_1, P_2, q\}$ chosen earlier to find

$$I^{\mu}_{\text{tri.1,2}} = -\frac{P_1 \cdot I_{\text{tri.1,2}} - y\frac{\sqrt{\tau_1}}{\sqrt{\tau_2}} P_2 \cdot I_{\text{tri.1,2}}}{\left(1-y^2\right)\tau_1} P_1^{\mu} - \frac{P_2 \cdot I_{\text{tri.1,2}} - y\frac{\sqrt{\tau_2}}{\sqrt{\tau_1}} P_1 \cdot I_{\text{tri.1,2}}}{\left(1-y^2\right)\tau_2} P_2^{\mu} \,. \tag{3.2.11}$$

Then, evaluating the dot products and the resulting angular integrals of the form (3.1.13), we find

$$[I^{\mu}_{\text{tri.1}}]_t = -\frac{1}{8\pi}\frac{\sqrt{\tau}}{\sqrt{t}}\left[-\frac{2}{\tau_1}\left(1 - \frac{\text{T}}{\sqrt{\tau\tau_1}}\operatorname{arctanh}\frac{\sqrt{\tau\tau_1}}{\text{T}}\right)\right] P_1^{\mu} \equiv [I_1]_t \, P_1^{\mu} \,, \tag{3.2.12a}$$

$$[I^{\nu}_{\text{tri.2}}]_t = -\frac{1}{8\pi}\frac{\sqrt{\tau}}{\sqrt{t}}\left[-\frac{2}{\tau_2}\left(1 - \frac{\text{T}}{\sqrt{\tau\tau_2}}\operatorname{arctanh}\frac{\sqrt{\tau\tau_2}}{\text{T}}\right)\right] P_2^{\nu} \equiv [I_2]_t \, P_2^{\nu} \,. \tag{3.2.12b}$$

Now, we use a similar process for the tensor integral $I^{\mu\nu}_{\text{box}}$. Using the fact that it is symmetric under the exchange of tensor indices, we write the decomposition in terms of the scalar integrals

$$\begin{aligned} I^{\mu\nu}_{\text{box}} = {} & P_1^{\mu}P_1^{\nu} I_{11} + (P_1^{\mu}P_2^{\nu} + P_2^{\mu}P_1^{\nu})\, I_{12} + P_2^{\mu}P_2^{\nu} I_{22} + (P_1^{\mu}q^{\nu} + q^{\mu}P_1^{\nu})\, I_{1q} \\ & + (P_2^{\mu}q^{\nu} + q^{\mu}P_2^{\nu})\, I_{2q} + q^{\mu}q^{\nu} I_{qq} + g^{\mu\nu} I_g \,, \end{aligned} \tag{3.2.13}$$

which can then be solved using the various contractions with pairs of external vectors. Ignoring the components containing q^{μ} as before, we obtain solutions to the system of the form

$$I_{11} = \frac{1}{\left(1-y^2\right)^2 \tau_1}\left[\frac{2}{\tau_1} P_{11}\cdot I - \frac{2y}{\sqrt{\tau_1}\sqrt{\tau_2}} P_{12}\cdot I + \frac{1+y^2}{\tau_2} P_{22}\cdot I + \left(1-y^2\right) Q\cdot I\right] , \tag{3.2.14a}$$

$$\begin{aligned} I_{12} = \frac{1}{2\left(1-y^2\right)^2 \sqrt{\tau_1}\sqrt{\tau_2}}\Bigg[& -\frac{4y}{\tau_1} P_{11}\cdot I + \frac{1+3y^2}{\sqrt{\tau_1}\sqrt{\tau_2}} P_{12}\cdot I - \frac{4y}{\tau_2} P_{22}\cdot I \\ & - 2y\left(1-y^2\right) Q\cdot I\Bigg] , \end{aligned} \tag{3.2.14b}$$

$$I_{22} = \frac{1}{\left(1-y^2\right)^2 \tau_2}\left[\frac{1+y^2}{\tau_1}P_{11}\cdot I - \frac{2y}{\sqrt{\tau_1}\sqrt{\tau_2}}P_{12}\cdot I + \frac{2}{\tau_2}P_{22}\cdot + \left(1-y^2\right)Q\cdot I\right], \tag{3.2.14c}$$

$$I_g = \frac{1}{1-y^2}\left[\frac{1}{\tau_1}P_{11}\cdot I - \frac{y}{\sqrt{\tau_1}\sqrt{\tau_2}}P_{12}\cdot I + \frac{1}{\tau_2}P_{22}\cdot I + \left(1-y^2\right)Q\cdot I\right], \tag{3.2.14d}$$

in terms of the four contractions

$$P_{11}\cdot I \equiv P_{1\mu}P_{1\nu}I^{\mu\nu}_{\text{box}}\,, \tag{3.2.15a}$$

$$P_{12}\cdot I \equiv \left(P_{1\mu}P_{2\nu}+P_{2\mu}P_{1\nu}\right)I^{\mu\nu}_{\text{box}}\,, \tag{3.2.15b}$$

$$P_{22}\cdot I \equiv P_{2\mu}P_{2\nu}I^{\mu\nu}_{\text{box}}\,, \tag{3.2.15c}$$

$$Q\cdot I \equiv \left(g_{\mu\nu}-\frac{1}{t}q_\mu q_\nu\right)I^{\mu\nu}_{\text{box}}\,. \tag{3.2.15d}$$

We write the matrix amplitude in terms of the scalar integrals we obtained above, and compute the spectral density ρ by taking the NR limit. Using the fact that $P_{1,2} = 2W - P_{2,1}$, where we have defined $W \equiv p_1 + p_2 = p_3 + p_4$ such that $W^2 = s$, we evaluate the spinor contractions in the CoM frame using the identities found in Appendix A, to get

$$\begin{aligned}\rho_a(s,t) = \frac{c_{\psi_1}^2 c_{\psi_2}^2}{4f^4}M_1M_2\Big\{&M_1M_2\left[I_g\right]_t \\ &+4M_1^2M_2\left(\sqrt{s}-M_2\right)\left[I_{11}\right]_t + 4M_1M_2^2\left(\sqrt{s}-M_1\right)\left[I_{22}\right]_t \\ &+4M_1M_2\left(M_1M_2+\left(\sqrt{s}-M_1\right)\left(\sqrt{s}-M_2\right)\right)\left[I_{12}\right]_t \\ &-2M_1^2\left[I_1\right]_t - 2M_2^2\left[I_2\right]_t + \left(-\frac{1}{8\pi}\frac{\sqrt{\tau}}{\sqrt{t}}\right)\Big\}.\end{aligned} \tag{3.2.16}$$

The angular integrals contain several terms which cannot be written as polynomials in t, and the integral (3.1.5) has therefore no exact analytical solution when using the expression above for the spectral density. To nonetheless obtain a closed form expression, we choose to evaluate the spectral density in the heavy external fermion limit $M_{1,2} \to \infty$. This limit implies that the resulting IP is only valid for a light mediator $m_a \ll M_{1,2}$ and for long ranges $r \gg 1/M_{1,2}$. In practice, fifth force experiments involve relatively long ranges ($r \gtrsim a_0$), with a_0 the Bohr radius, and are only sensitive to light axion masses $m_a < 1\,\text{eV}$. If we consider the interaction

between two nucleons, or even a nucleon and an electron, this sets a range limit at $r_{\min} \approx 10^{-12}\,\mathrm{m}$, well below the ranges of interest. In this limit, we have $\sqrt{s} \approx M_1 + M_2$ and the expression above simplifies to

$$\rho_a(t) = \frac{c_{\psi_1}^2 c_{\psi_2}^2}{4f^4} M_1 M_2 \left\{ 4M_1^3 M_2 \left[I_{11}\right]_t + 4M_1 M_2^3 \left[I_{22}\right]_t + 8M_1^2 M_2^2 \left[I_{12}\right]_t \right. \\ \left. + M_1 M_2 \left[I_g\right]_t - 2M_1^2 \left[I_1\right]_t - 2M_2^2 \left[I_2\right]_t + \left(-\frac{1}{8\pi}\frac{\sqrt{\tau}}{\sqrt{t}}\right) \right\}. \quad (3.2.17)$$

When taking a similar expansion in the massless mediator limit, the authors of [143] show that terms odd in powers of $\sqrt{t}$ (or equivalently odd in powers of $M_{1,2}$) are cancelled by the contributions from the iterated lowest order potential which we have ignored so far. This allows us to only consider terms even in powers of $M_{1,2}$ in the expansion.

Recognising the first four terms in (3.2.17) as the contributions from box-type diagrams from Figure 3.4, the fifth and sixth terms from triangle-type diagrams, and the final term from the bubble diagram from Figure 3.5, we separate the spectral density as $\rho_a = \rho_{\text{box}} + \rho_{\text{tri.1}} + \rho_{\text{tri.2}} + \rho_{\text{bub.}}$ and evaluate these to, up to order $1/M_{1,2}^2$,

$$\rho_{\text{box}} = -\frac{c_{\psi_1}^2 c_{\psi_2}^2}{32\pi f^4} M_1 M_2 \frac{\sqrt{\tau}}{\sqrt{t}} \left[1 + \left(\frac{1}{4M_1^2} + \frac{1}{4M_2^2}\right)\left(t + \frac{\mathrm{T}^2}{\tau}\right) - \frac{t}{4M_1 M_2}\right], \quad (3.2.18a)$$

$$\rho_{\text{tri.1}} = +\frac{c_{\psi_1}^2 c_{\psi_2}^2}{32\pi f^4} M_1 M_2 \frac{\sqrt{\tau}}{\sqrt{t}} \left[1 + \frac{1}{4M_1^2}\left(t + \frac{\mathrm{T}^2}{\tau}\right)\right], \quad (3.2.18b)$$

$$\rho_{\text{tri.2}} = +\frac{c_{\psi_1}^2 c_{\psi_2}^2}{32\pi f^4} M_1 M_2 \frac{\sqrt{\tau}}{\sqrt{t}} \left[1 + \frac{1}{4M_2^2}\left(t + \frac{\mathrm{T}^2}{\tau}\right)\right], \quad (3.2.18c)$$

$$\rho_{\text{bub.}} = -\frac{c_{\psi_1}^2 c_{\psi_2}^2}{32\pi f^4} M_1 M_2 \frac{\sqrt{\tau}}{\sqrt{t}}. \quad (3.2.18d)$$

Summing these contributions together we finally obtain

$$\rho_a(t) = \frac{c_{\psi_1}^2 c_{\psi_2}^2}{128\pi f^4} \frac{\sqrt{\tau}}{\sqrt{t}} t + O\left(\frac{1}{M_{1,2}^2}\right). \quad (3.2.19)$$

Recalling the discussion in Section 3.2.1 and repeating this calculation in the "naive" mass basis, that is ignoring the a^2/f^2 term in the right-hand side of (3.2.3), we find that only the contributions from the "box" terms are present[2], yielding a spectral

[2]Pictorially, we realise that the triangle and bubble type diagrams in Figure 3.5 require a

density $\rho' = \rho_{\text{box}}$. This spectral density will eventually yield the r^{-3} potential found when considering a purely pseudoscalar interaction of the form $\phi\bar{\psi}\gamma^5\psi$ [143], or, noting that it is also exactly equal to $\rho_{\text{bub.}}$ at leading order, a quadratic scalar interaction of the form $\phi^2\bar{\psi}\psi$. Only when including the additional quadratic terms do we observe a cancellation between the spectral densities at leading order, leaving a higher order r^{-5} potential.

Finally, we use (3.1.5) to obtain the full axion IP

$$V_a(r) = \frac{3c_{\psi_1}^2 c_{\psi_2}^2}{128\pi^3 f^4}\frac{1}{r^5}\left[2m_a^2 r^2 K_2(2m_a r) + \frac{4}{3}m_a^3 r^3 K_1(2m_a r)\right], \tag{3.2.20}$$

and the purely pseudoscalar, or quadratic scalar, potential

$$V'(r) = -\frac{c_{\psi_1}^2 c_{\psi_2}^2}{64\pi^3 f^4}M_1 M_2 \frac{1}{r^3}\left[2m_\phi r K_1(2m_\phi r)\right]. \tag{3.2.21}$$

As earlier, we have normalised these expressions such that the terms in square brackets tend to 1 as $m_{a,\phi} \to 0$. Expanding in this small mass parameter, we find

$$V_a(r) = \frac{3c_{\psi_1}^2 c_{\psi_2}^2}{128\pi^3 f^4}\left(\frac{1}{r^5} - \frac{1}{3}\frac{m_a^2}{r^3} + O(m_a^4)\right), \tag{3.2.22}$$

$$V'(r) = -\frac{c_{\psi_1}^2 c_{\psi_2}^2}{64\pi^3 f^4}M_1 M_2\left(\frac{1}{r^3} + \left(-1 + 2\gamma_E + 2\log m_\phi r\right)\frac{m_\phi^2}{r} + O(m_\phi^4)\right). \tag{3.2.23}$$

3.2.3 Axion-nucleon Interactions

To quadratic order in a, the inclusion of the additional quadratic operator in (3.2.3) restores the results obtained using the shift invariant coupling. However, the shift invariance in (3.2.1) is explicitly broken by the presence of an axion mass. Treating m_a^2 as the only spurion that breaks the shift invariance suggests the existence of higher order shift symmetry breaking operators proportional to this spurion term, such as

$$\mathcal{O}_{\text{ssb}} \supset \sum_\psi m_a^2 \frac{c_m}{f^3} a^2 \bar{\psi}\psi\,, \tag{3.2.24}$$

quadratic vertex.

where c_m is a dimensionless Wilson coefficient. These operators spoil the cancellation in (3.2.3).

In general, it is a conservative assumption that the spurion is given by m_a^2, because the source of shift symmetry breaking responsible for generating the axion mass can induce higher-order operators that are less suppressed than (3.2.24). An example of such an enhancement is the coupling of the QCD axion to nucleons. The shift symmetry is explicitly broken by the presence of light quark masses and the QCD confinement scale via the second term of (2.4.29). Interactions between the QCD axion and nucleons are therefore shift-invariant or suppressed by these spurions. At leading order, the operators of the two-flavour chiral Lagrangian coupling baryons to pions and axions read [114, 144]

$$\mathcal{L}_{aN}^{(1)} = \bar{N}\left(i\not{D} - m_N + \frac{g_A}{2}\gamma^\mu\gamma^5\boldsymbol{u}_\mu + g_0\gamma^\mu\gamma^5 a_\mu^{(s)}\right)N\,. \tag{3.2.25}$$

Couplings to the axion enter via the covariant derivative D_μ and the objects $\boldsymbol{u}_\mu$ and $a_\mu^{(s)}$, all three of which contain the axion in an explicitly shift-invariant way, and can be found in Section 2.5 of [114]. At second order, there are four operators [144],

$$\begin{aligned}\mathcal{L}_{aN}^{(2)} = c_1\,\mathrm{Tr}\left[\boldsymbol{\chi}_+\right]\bar{N}N - \frac{c_2}{4m_N^2}\,\mathrm{Tr}\left[\boldsymbol{u}_\mu\boldsymbol{u}_\nu\right]\left(\bar{N}D^\mu D^\nu N + \text{h.c.}\right)\\ + \frac{c_3}{2}\,\mathrm{Tr}\left[\boldsymbol{u}_\mu\boldsymbol{u}^\mu\right]\bar{N}N - \frac{c_4}{4}\bar{N}\gamma^\mu\gamma^\nu\left[\boldsymbol{u}_\mu,\boldsymbol{u}_\nu\right]N\,.\end{aligned} \tag{3.2.26}$$

The axion field additionally enters via

$$\boldsymbol{\chi}_+ = 2B_0\left(\boldsymbol{\xi}^\dagger\hat{\boldsymbol{m}}_q(a)\boldsymbol{\xi}^\dagger + \boldsymbol{\xi}\hat{\boldsymbol{m}}_q^\dagger(a)\boldsymbol{\xi}\right)\,, \tag{3.2.27}$$

$$\hat{\boldsymbol{m}}_q(a) = e^{-i\boldsymbol{\kappa}_q\frac{a}{2f}(2c_{GG}+c_u+c_d)}\boldsymbol{m}_q e^{-i\boldsymbol{\kappa}_q\frac{a}{2f}(2c_{GG}+c_u+c_d)}\,, \tag{3.2.28}$$

where B_0 is the parameter appearing in the Gell-Mann-Oakes-Renner relation $m_\pi^2 \approx B_0(m_u+m_d)$ [145], $\boldsymbol{\xi} = \exp\left(i\frac{1}{\sqrt{2}f_\pi}\pi^b\boldsymbol{\sigma}^b\right)$ contains the pion fields, the quark matrices read $\boldsymbol{m}_q = \mathrm{diag}(m_u, m_d)$, and $\boldsymbol{\kappa}_q = \mathrm{diag}(\kappa_u, \kappa_d)$ are unphysical parameters[3] subject

[3] They can be chosen freely as they will drop out of any physical result, but we note that (2.4.29), taken from [17], was written with a choice of $\boldsymbol{\kappa}_q$ such as to eliminate ALP-pion mixing at leading order in f_π/f.

to the constraint $\mathrm{Tr}[\boldsymbol{\kappa}_q] = 1$. All operators in (3.2.26) are shift-invariant, apart from the operator with coefficient c_1, which contains a shift-symmetry breaking interaction

$$c_1 \,\mathrm{Tr}\,[\boldsymbol{\chi}_+]\,\bar{N}N = c_N \frac{a^2}{f^2}\bar{N}N + \dots \tag{3.2.29}$$

After rotating into the mass eigenbasis and taking into account contributions from pion mixing one can write the leading terms for the amplitude of axions coupled to nuclei from (3.2.25) and (3.2.26) as

$$i\mathcal{M}\left(N(k') \to N(k) + a(q)\right) = -\frac{g_N}{4f}\bar{u}_N(k')\not{q}\gamma^5 u_N(k)\,, \tag{3.2.30a}$$

$$i\mathcal{M}\left(N(k') \to N(k) + 2a(q/2)\right) = -\frac{c_N}{f^2}\bar{u}_N(k')u_N(k) \tag{3.2.30b}$$

respectively. Here, the couplings are defined for protons and neutrons $N = p, n$, with g_N defined in (2.4.31) and

$$c_N = -c_1\frac{m_\pi^2}{2}\frac{1}{(1-\tau_a)^2}\left\{4c_{GG}^2\left[\tau_a^2 + 4(1-2\tau_a)\frac{m_u m_d}{(m_u+m_d)^2}\right]\right.$$
$$\left. - 4\tau_a^2 c_{GG}(c_d - c_u)\frac{m_d - m_u}{m_d + m_u} + \tau_a^2(c_d - c_u)^2\right\}, \tag{3.2.31}$$

with $\tau_a = m_a^2/m_\pi^2$. The low energy coefficients c_1, c_2, c_3, c_4 can be found in [85], we use $c_1 = -1.26(14)\,\mathrm{GeV}^{-1}$ here.

Expanding c_N in small axion masses and using the expression for the QCD axion mass (2.4.29) with $m_u = m_d$, one can write the coefficient in (3.2.24) as $c_m = -8c_1 f^3/f_\pi^2$, which corresponds to a substantial enhancement compared with the naive assumption.

Since the axion has a potential, in principle any quadratic interaction can also give rise to a linear spin-independent interaction if the axion vacuum expectation value does not vanish. The Vafa-Witten theorem guarantees that $\langle a\rangle = 0$ in vacuum [146], but in a high density environment the potential is modified such that the minimum of the axion potential jumps to $\langle a\rangle = \pi f$ above some critical density, leading to long-range forces for large, dense objects such as neutron stars [147, 148].

In general, linear interactions proportional to the theta angle are strongly sup-

pressed [149–151]. For the remainder of this chapter, we therefore focus on the spin-independent force induced by the exchange of axion pairs.

Consider now the ALP IP; additional contributions from shift-symmetry breaking operators (3.2.24) are suppressed by $\sim 1/f^6$. However, in the case of the QCD axion there are additional terms at order $1/f^4$ induced by the quadratic interaction terms (3.2.29) proportional to the shift-symmetry breaking spurion responsible for the axion mass. Evaluated for an interaction between two nucleons N_1 and N_2, the quadratic interaction (3.2.29) generates five additional diagrams as shown in Figure 3.7, corresponding to the diagrams in Figure 3.5 with a new type of quadratic vertex carrying a coupling c_N. These additional contributions take the form of the spectral densities (3.2.18b), (3.2.18c) and (3.2.18d), eventually giving the extra potential

$$\begin{aligned} V_{\text{sp.}}(r) = -\frac{c_{N_1}c_{N_2}}{64\pi^3 f^4}\frac{1}{r^3}\left[2m_a r K_1(2m_a r)\right] \\ + \frac{3}{64\pi^3 f^4}\left(c_{\psi_1}^2 c_{N_2}\frac{1}{M_1} + c_{N_1}c_{\psi_2}^2\frac{1}{M_2}\right)\frac{1}{r^5} \\ \times\left[m_a^3 r^3 K_1(2m_a r) + \left(2m_a^2 r^2 + \frac{1}{3}m_a^4 r^4\right)K_2(2m_a r)\right]. \end{aligned} \tag{3.2.32}$$

We note that the leading order contribution from the mixed $c_{\psi_i}^2 c_{N_j}$ term cancel out between the triangle and bubble diagrams from Figure 3.7. As a result, the effect of the shift-symmetry breaking interaction will not significantly affect an IP between a nucleon and lepton, as only the $c_{N_1}c_{N_2}$ term contributes to leading order in (3.2.32).

The contributions from the quadratic axion interaction induced by the spurion (3.2.32) dominate over the contribution from the interaction induced by shift-invariant operators (3.2.20), even though the latter appear at leading order in the EFT expansion. Note that this is different from the corrections in the expansion (3.2.22) which are suppressed by the axion mass, which in the case of the QCD axion scales as $m_a^2 \propto f_\pi^4/f^2$. We also note that the importance of the shift-symmetry breaking operator has been pointed out previously in the context of coherent axion-nucleon scattering [152].

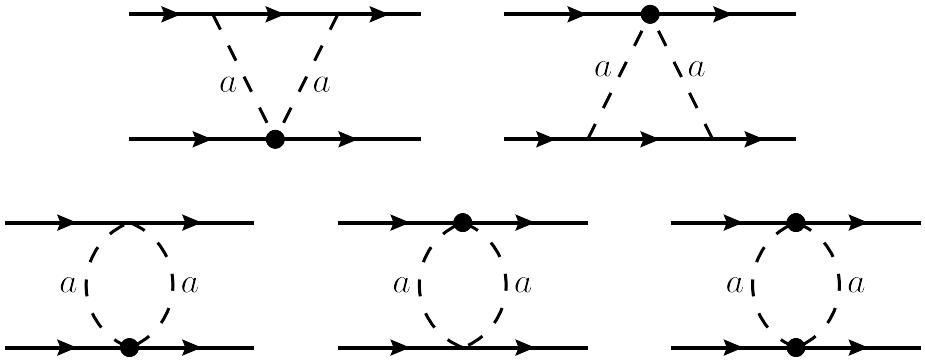

Figure 3.7: Additional diagrams for the ALP IP generated by the presence of an extra quadratic vertex. Bullets indicate a vertex carrying a coupling c_N.

3.2.4 Fifth Force Constraints on Axions

In the following, we illustrate the effect of the shift-symmetry breaking interaction on the sensitivity of experiments searching for a fifth force. We consider the simplest axion model with a single coupling to gluons described by the Wilson coefficient c_{GG}, keeping its mass m_a a free parameter. Constraints on such a model will be expressed as bounds on c_{GG}/f as a function of m_a; for the specific case of the QCD axion, the mass is not a free parameter, and it is useful to recast these as bounds on c_{GG} as a function of f.

There are several ways to search for the effects of a new, macroscopic force, including searches with Cavendish-type experiments [153], searches for new forces in atoms and molecules [154], measurements of the effective Casimir pressure [155, 156] and experiments specifically designed to suppress the Casimir force [157]. Bounds from atomic and molecular spectroscopy are not substantially changed by the inclusion of the higher order operators (3.2.26) as the leading effects only affect nucleon-nucleon interactions. We then consider experiments probing macroscopic, spin-independent forces such as the one described in [157], in which the difference in the force between a sphere and a plate of two different materials is probed, which minimises the contribution from the Casimir effect. The accuracy in measuring this force (or absence thereof) has been used in [158] to obtain the best limits on the pseudoscalar-to-

nucleon coupling in the meV–eV range for an experiment of this type.

The experimental setup consists of a disk of thickness D with alternating gold (Au) and silicon (Si) sections, coated with a uniform layer of gold to equalise the Casimir force, placed at a distance ℓ from a sphere of radius R. The sphere is made of a sapphire (sa.) core coated with a layer of chrome (Cr) of thickness $d_{\rm Cr}$ and an outer layer of gold of thickness $d_{\rm Au}$. The corresponding differential force between the sphere and the disk (taken to be infinitely wide) reads

$$\Delta F(\ell) = 2\pi C_s \left(C_{\rm Au} - C_{\rm Si}\right) \int_\ell^{2R+\ell} \mathrm{d}z_1 \left[R^2 - (z_1 - R - \ell)^2\right] \times \frac{\partial}{\partial z_1} \int_{-D}^0 \mathrm{d}z_2 \int_0^\infty \rho \mathrm{d}\rho \; \mathcal{V}\left(\sqrt{\rho^2 + (z_1 - z_2)^2}\right) , \quad (3.2.33)$$

where we factor out the coupling constants such that $V_a(r) = c_{\psi_1}^2 c_{\psi_2}^2 \mathcal{V}_a(r)$ in the case of the potential derived from the derivative interaction (3.2.20), and $V_{\rm sp.}(r) = c_{N_1} c_{N_2} \mathcal{V}_{\rm sp.}(r)$ for the leading term of (3.2.32). We define the material-dependent prefactors in terms of the axion couplings to nucleons (2.4.31) and (3.2.31), respectively

$$C_X = \rho_X \left(\frac{g_p^2}{4}\frac{Z_X}{m_X} + \frac{g_n^2}{4}\frac{N_X}{m_X}\right) , \quad (3.2.34a)$$

$$C_X = \rho_X c_N \frac{A_X}{m_X} , \quad (3.2.34b)$$

with density ρ_X, average number of protons and neutrons $A_X = Z_X + N_X$, and mean masses m_X of the disc and sphere atoms for a material X. The calculation of (3.2.33) is lengthy but straightforward following [156, 158, 159]. Integrating (3.2.33) for the potential (3.2.20) and (3.2.32) yields respectively

$$\Delta F_a(\ell) = \frac{3}{64\pi m_a}\frac{1}{f_4}\left|C_{\rm Au} - C_{\rm Si}\right| \int_1^\infty \mathrm{d}u \; \frac{\sqrt{u^2-1}}{u^3} \sum_l C_l \Psi(m_a u) , \quad (3.2.35a)$$

$$\Delta F_{\rm sp.}(\ell) = \frac{1}{32\pi m_a}\frac{1}{f^4}\left|C_{\rm Au} - C_{\rm Si}\right| \int_1^\infty \mathrm{d}u \; \frac{\sqrt{u^2-1}}{u^3} e^{-2m_a u \ell}\left(1 - e^{-2m_a u D}\right) X(m_a u) . \quad (3.2.35b)$$

The coefficients C_X are given by (3.2.34a) and (3.2.34b) respectively, and the func-

tion $X(x)$ is given by Eq. (11) in [158]. The sum in (3.2.35a) is

$$\sum_l C_l \Psi(x) = C_{\rm Au}\Psi(x; R, \ell) + (C_{\rm Cr} - C_{\rm Au})\Psi(x; R - d_{\rm Au}, \ell + d_{\rm Au}) + (C_{\rm sa.} - C_{\rm Cr})\Psi(x; R - d_{\rm Au} - d_{\rm Cr}, \ell + d_{\rm Au} + d_{\rm Cr}) \quad (3.2.36)$$

with the function

$$\Psi(x; R, \ell) = 8x^4 \int_\ell^{2R+\ell} {\rm d}z \ \left[R^2 - (R + \ell - z)^2\right] \times \left\{ -\frac{e^{-2xz}}{2xz}\left(1 - \frac{z}{D+z}e^{-2xD}\right) + {\rm Ei}\left[-2x(D+z)\right] - {\rm Ei}\left[-2xz\right] \right\} \quad (3.2.37)$$

where ${\rm Ei}(x)$ is the exponential integral function. We mention that Ψ has a closed but unwieldy analytical form. Comparing the axion force derived from the shift-symmetry breaking interactions $V_{\rm sp.}(r)$ to that derived from the derivative interactions $V_a(r)$, we note that, as expected, the former grows with ℓ relative to the latter, such that $\Delta F_{\rm sp.}/\Delta F_a \sim m_\pi^2 \ell^2$.

The resulting bounds on c_{GG}/f are shown as a function of the axion mass in Figure 3.8. The red line is the bound obtained by using the purely pseudoscalar interaction term $a\bar{\psi}\gamma^5\psi$ in (3.2.3). However, including the quadratic interaction terms as shown in (3.2.3) changes the potential to the $1/r^5$ form in (3.2.20), resulting in a substantially weaker bound compared to the previous potential, as shown by the position of the green line in the figure. The quadratic nucleon spurion term in (3.2.29) generates the additional potential (3.2.32) proportional to $1/r^3$ at leading order. Furthermore, the coupling of this term is not suppressed by the axion mass, unlike what one would expect from a spurion breaking the axion shift symmetry. As a result, this spurion term generates a bound close to that obtained using the $1/r^3$ pseudoscalar potential; this bound is shown by the blue line in Figure 3.8.

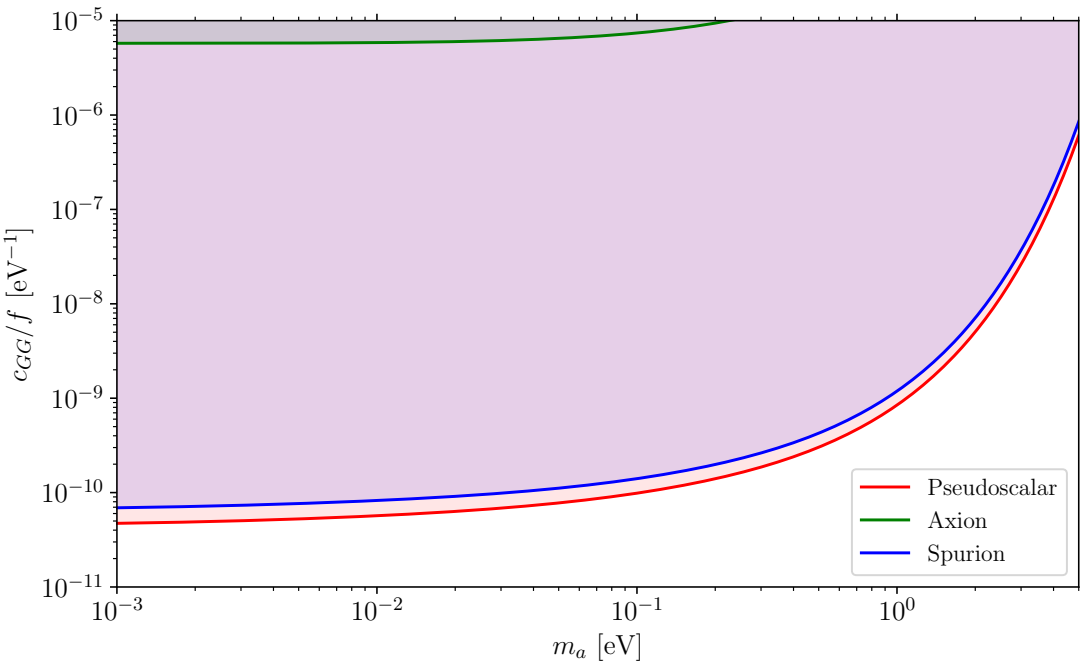

Figure 3.8: Limits on the axion-gluon couplings c_{GG}/f obtained from the Casimir-less experiment [157]. The red contour corresponds to the limit obtained using the pseudoscalar form of the potential (3.2.21), the green contour corresponds to the axion potential without shift-symmetry breaking terms (3.2.20), and the blue line corresponds to the full axion potential including the nucleon spurion term (3.2.32).

3.3 Summary

In this chapter, we have developed a framework for deriving long-range, spin-dependent and -independent, IPs, starting from the simple case of tree-level, single particle exchanges to more complicated loop-induced pair exchanges. We have applied this method to evaluate IPs for several interactions, notably the full neutrino pair exchange IP, and the first result for the massive ALP pair exchange IP.

For the latter, we have identified the dominant contribution to the low-energy potential for ALPs that—like the QCD axion—obtain their mass from the chiral anomaly. This contribution arises from higher-order operators of the axion Lagrangian that would naively be expected to produce subleading effects. We show explicitly that these operators not only generate the most important contribution to the IP, but

result in a scaling $V(r) \sim 1/r^3$ as opposed to the leading term $V(r) \sim 1/r^5$ expected from derivative interactions. Moreover, since the QCD axion mass is generated via strong dynamics, this new contribution is only present for interactions between hadrons and so the nature of the shift-symmetry breaking for an axion can be probed via the comparison of different searches for fifth forces. We demonstrate the impact with the example of a Casimir-less fifth-force experiment and find an improved sensitivity of almost five orders of magnitude in c_{GG}/f.

Chapter 4

The Axion-Higgs Portal

4.1 Motivation

In the general dimension-5 ALP Lagrangian (2.4.15) from earlier, we explicitly omitted the dimension-5 operator (2.4.16) describing the interactions between an axion and the Higgs boson, as it can be shown to vanish under field redefinitions. In fact, the leading order axion-Higgs interaction to give non-zero contributions to Higgs decays is the dimension-6 operator [160]

$$\mathcal{O}_{a\Phi}^{(6)} = \frac{c_{ah}}{f^2}(\partial_\mu a)(\partial^\mu a)\Phi^\dagger\Phi \tag{4.1.1}$$

which we name the *derivative Higgs portal*, or *axion-Higgs portal*, in order to avoid confusion with scalar dimension-4 operators often referred to as Higgs portals. Importantly, the operator (4.1.1) is the leading operator in the axion field expansion that preserves the shift symmetry $a \to a + c$, where c is a constant, and is invariant under the Z_2 transformation $a \to -a$.

Such an ALP has several interesting features. It can be a dark matter candidate independent of its mass as it cannot decay, and interactions with light SM particles are strongly suppressed by Higgs couplings as well as by the momentum suppression due to the two derivatives in (4.1.1). As a consequence, it is particularly challenging to discover an axion that interacts with the SM through this operator, and

observables based on very precise measurements at low energies can be less sensitive compared to high-energy probes.

Near the UV scale, we define the theory of the axion-Higgs portal as an extension of the SM with a real pseudoscalar field a and an effective Lagrangian

$$\mathcal{L}_{ah}(\mu < f) = \frac{1}{2}(\partial_\mu a)(\partial^\mu a) - \frac{1}{2}m_a^2 a^2 + \frac{c_{ah}}{f^2}(\partial_\mu a)(\partial^\mu a)\Phi^\dagger\Phi + \mathcal{L}_{\text{SM}}\,, \tag{4.1.2}$$

where $\mathcal{L}_{\text{SM}}$ denotes the SM Lagrangian. For this discussion, we consider the Z_2 symmetry as a consequence of the UV completion which remains unbroken at the level of the effective theory, while the shift symmetry is softly broken by the axion mass m_a. The Z_2 symmetry implies that the effects of the axion do not introduce any additional parity violation, independent of it being a scalar or a pseudoscalar particle. In the following sections, we will discuss some theoretical and phenomenological aspects of this model. We compare constraints from spectroscopy experiments, flavour violating and flavour conserving meson decays, invisible Higgs decays and astrophysics. Throughout the discussion we will compare these results with the corresponding parameter space for a renormalisable *scalar Higgs portal* [161]

$$\mathcal{O}_{s\Phi} = c_{sh}s^2\Phi^\dagger\Phi \tag{4.1.3}$$

which is not protected by a shift symmetry, but still invariant under the Z_2 transformation $s \to -s$. Therefore—in contrast to the axion—the mass of the scalar s is not protected against quadratically divergent radiative corrections.

In this chapter, we first consider some theoretical aspects of the axion-Higgs portal in Section 4.2, namely we present a simple model for a UV completion, write down its interactions with SM particles present at various energy scales, and consider its suitability as a true QCD axion. Then, in Section 4.3, we place constraints on the axion-Higgs portal, via Higgs boson and meson decays, and fifth force effects.

4.2 The Theory of the Axion-Higgs Portal

4.2.1 A Minimal UV Completion

The discussion in this chapter does not depend on the specific UV completion of (4.1.2), but for completeness we nonetheless give a particularly simple UV completion of the SM by introducing a complex scalar singlet [160]

$$S = \frac{s+f}{\sqrt{2}} e^{ia/f}\,, \tag{4.2.1}$$

with a vacuum expectation value $\langle S\rangle = f/\sqrt{2}$, coupled to the SM Higgs doublet and with a corresponding Lagrangian

$$\mathcal{L}_S = (\partial_\mu S^\dagger)(\partial^\mu S) + \mu_s^2 S^\dagger S - \lambda_s (S^\dagger S)^2 - \lambda_{hs} S^\dagger S \Phi^\dagger \Phi + \mathcal{L}_{\rm SM}\,. \tag{4.2.2}$$

This Lagrangian arises from the assumption that no SM fields are charged under the global U(1) symmetry associated with this complex scalar, such that linear interactions with S are forbidden.

Expanding (4.2.2) in terms of the radial s and angular a modes of S yields

$$\begin{aligned}\mathcal{L}_S = {}& \frac{1}{2}(\partial_\mu s)(\partial^\mu s) + \frac{1}{2}\left(\mu_s^2 - 3\lambda_s f^2\right) s^2 - \lambda_s f s^3 - \frac{1}{4}\lambda_s s^4 \\ & + \frac{1}{2}(\partial_\mu a)(\partial^\mu a) + \frac{1}{f} s (\partial_\mu a)(\partial^\mu a) + \frac{1}{2f^2} s^2 (\partial_\mu a)(\partial^\mu a) \\ & - \frac{1}{2}\lambda_{hs} f^2 \Phi^\dagger\Phi - \lambda_{hs} f s \Phi^\dagger\Phi - \frac{1}{2}\lambda_{hs} s^2 \Phi^\dagger\Phi\,. \end{aligned} \tag{4.2.3}$$

Upon EWSB, the radial mode s mixes with the SM Higgs field. The dominant contribution to the mass of the radial mode is determined by the scale f, whereas the mass m_a of the Pseudo Nambu-Goldstone Boson (PNGB) a is generated by explicit symmetry breaking effects. In order for (4.2.3) to match onto (4.1.2) we assume that the scalar s is sufficiently heavy and can be integrated out at the energy scales that we can access experimentally. From (4.2.3) follows for the axion-Higgs portal

$$c_{ah} = \frac{f}{v}\sin\alpha \qquad \text{with} \qquad \tan 2\alpha = \frac{2\lambda_{hs} v f}{m_s^2 - m_h^2}, \tag{4.2.4}$$

where m_s and m_h are the masses of the radial mode s and the SM Higgs boson h, respectively. The coefficients in (4.2.3) are constrained by measurements of the SM Higgs decays into SM particles. For example, a conservative estimate using bounds on the signal strength from Large Hadron Collider (LHC) Higgs analyses leads to $|\sin\alpha| < 0.2$ for masses $m_s > m_h/2$ [162–164]. Further constraints on the parameters in (4.2.3) arise from perturbativity, requiring a stable minimum of the potential and measurements of electroweak precision observables [165].

4.2.2 The Axion-Higgs Portal at Different Scales

As earlier for the full dimension-5 ALP Lagrangian from Section 2.4.3, we need to translate $\mathcal{L}_{ah}$ as defined in (4.1.2) in terms of heavy SM d.o.f. to a Lagrangian involving only particles present in low-energy environments, namely nucleons and electrons.

Below the electroweak scale $\mu < v$, we integrate out the $W^\pm$ and Z gauge bosons as well as the Higgs scalar and the top quark, so that we can write the effective Lagrangian as

$$\begin{aligned}\mathcal{L}_{ah}(\mu < v) = \frac{c_{ah}c_\gamma}{f^2 m_h^2}(\partial_\mu a)(\partial^\mu a)F_{\rho\sigma}F^{\rho\sigma} + \frac{c_{ah}c_G}{f^2 m_h^2}(\partial_\mu a)(\partial^\mu a)G^a_{\rho\sigma}G^{\rho\sigma a} \\ - \sum_{i,j}\frac{c_{ah}c_{ij}}{f^2 m_h^2}(\partial_\mu a)(\partial^\mu a)\bar{\psi}_i\Big(m_i P_L + m_j P_R\Big)\psi_j + \text{h.c.}\end{aligned} \tag{4.2.5}$$

Here, m_i and m_j are the masses of the fermions ψ_i and ψ_j and the sum over i, j extends over all SM leptons and quarks apart from the top quark. The dimensionless Wilson coefficients are obtained to leading order in $m_h^2/(2m_t)^2$ and $m_h^2/(2m_W)^2$. In this limit, the couplings between the axion and gauge bosons read [166]

$$c_\gamma = -\frac{\alpha}{4\pi}\frac{47}{18}\,, \qquad c_G = \frac{\alpha_s}{4\pi}\frac{1}{3}\,, \tag{4.2.6}$$

and the couplings of the axion to SM fermions are given by

$$c_{ii} = \frac{1}{2}\,, \tag{4.2.7}$$

in the case of flavour diagonal couplings. Flavour-violating axion couplings are induced through the Higgs penguin [167–169] and are only relevant for external down-type quarks. For example, the axion-coupling to d and s quarks is given by

$$c_{ds} = -\frac{3}{16\pi^2}\frac{m_t^2}{v^2}V_{td}^* V_{ts}\,. \tag{4.2.8}$$

The Wilson coefficients for the flavour changing transitions $b \to d$ and $b \to s$ can be obtained by replacing the CKM elements in (4.2.8). Flavour changing axion couplings to up-type quarks are suppressed by m_b^2/v^2 at the amplitude level, and charged lepton flavour-changing couplings are suppressed by neutrino masses.

In contrast to the QCD axion, or more generally axions that interact linearly with quarks or gluons [170], the axion-Higgs portal does not induce mixing between the neutral pion or other pseudoscalar mesons with the axion as long as the Z_2 symmetry remains unbroken. At energies below the QCD scale $\Lambda_{\rm QCD}$, the relevant degrees of freedom are nucleons, leptons and photons. The effective Lagrangian for interactions induced by the axion-Higgs portal then reads

$$\begin{aligned}\mathcal{L}_{ah}(\mu < \Lambda_{\rm QCD}) = \frac{c_{ah}c_N}{f^2 m_h^2} m_N (\partial_\mu a)(\partial^\mu a)\bar{N}N + \frac{c_{ah}m_l}{f^2 m_h^2}(\partial_\mu a)(\partial^\mu a)\bar{l}l \\ + \frac{c_{ah}c_\gamma}{f^2 m_h^2}(\partial_\mu a)(\partial^\mu a)F_{\rho\sigma}F^{\rho\sigma}\,,\end{aligned} \tag{4.2.9}$$

where the nucleons are protons and neutrons $N = p, n$ with mass m_N and the leptons can be electrons or muons $l = e, \mu$ with mass m_l. The coupling to nucleons can be written as [171]

$$c_N = \sum_{q=u,d,s} f_q^N + \frac{6}{27} f_{TG}\,, \tag{4.2.10}$$

with the matrix elements defined by

$$f_q^N \equiv \frac{\langle N|m_q \bar{q}q|N\rangle}{m_N}\,, \quad \frac{8\pi}{9\alpha_s} f_{TG} = -\frac{\langle N|G^a_{\rho\sigma}G^{\rho\sigma a}|N\rangle}{m_N}\,, \tag{4.2.11}$$

that can be determined from pion-nucleon scattering [172–174]. Using the results from [175], we find the numerical values

$$c_p \approx c_n \approx 0.30\,. \tag{4.2.12}$$

We will neglect the mass difference between the proton and the neutron.

For the scalar Higgs portal defined via the interaction (4.1.3), the matching procedure outlined above can be repeated in a straightforward way, by replacing the field structures and couplings with, respectively,

$$(\partial_\mu a)(\partial^\mu a) \to s^2 \quad \text{and} \quad \frac{c_{ah}}{f^2} \to c_{sh}\,, \tag{4.2.13}$$

leaving the Wilson coefficients unchanged.

4.2.3 Relation to the Strong CP Problem

We briefly discuss the possibility of the axion as defined in (4.1.2) being a solution to the strong CP problem. We recall the discussion in Section 2.4.1 and how we subsequently defined the axion in (2.4.13) such as to drive the value of the effective strong CP angle θ_{eff} to zero.

For the case of the axion-Higgs portal, the coupling (2.4.13) is forbidden by the Z_2 symmetry prohibiting linear axion couplings. This Z_2 symmetry is a global symmetry and should therefore be explicitly broken at a scale Λ_{Z_2} that need not be related to the scale of shift symmetry breaking Λ_{PQ} and should fulfil $\Lambda_{Z_2} \gg f$ in order to make the axion-Higgs portal a good effective theory, so that the equivalent to (2.4.13) reads

$$\mathcal{L} \ni \frac{g_s^2}{32\pi^2}\left(\bar{\theta} + \frac{a}{\Lambda_{Z_2}}\right) G^a_{\mu\nu}\tilde{G}^{\mu\nu a}\,. \tag{4.2.14}$$

The axion couplings to Higgs bosons and gluons can therefore be controlled by different scales, but because the axion is periodic (such that $a = a + 2\pi f$), the allowed parameter space for the effective QCD theta angle becomes

$$\theta_{\text{eff}} = \bar{\theta} + \frac{a}{\Lambda_{Z_2}} \in \left[\bar{\theta} - \pi\frac{f}{\Lambda_{Z_2}}, \bar{\theta} + \pi\frac{f}{\Lambda_{Z_2}}\right)\,. \tag{4.2.15}$$

Given the hierarchy $f \ll \Lambda_{Z_2}$, the vacuum expectation value $\langle\theta_{\text{eff}}\rangle$ can only take values in the close vicinity of $\bar{\theta}$. This is in contrast to the QCD axion, where the Z_2

symmetry is spontaneously broken as well, so that $\Lambda_{Z_2} = f$ and the axion field can balance an arbitrary value of $\bar{\theta}$. We conclude that the mechanism that solves the strong CP problem for the QCD axion does not work if the axion-Higgs portal is the dominant interaction between SM fields and the axion. This discussion did not rely on the specific properties of the axion-Higgs portal, but holds for any ALP model where the coupling (2.4.13) is forbidden by a global symmetry and only generated through explicit symmetry breaking.

4.3 Phenomenological Constraints on the Axion-Higgs Portal

After the preparations of the last section, we are now ready to calculate the predictions of the axion-Higgs portal and compare them to experimental data. The phenomenology of the axion-Higgs portal is different from the QCD axion and other linearly coupled ALPs. Axions and ALPs are constrained by searches for the direct production at colliders [109, 176, 177], indirect effects in lab based experiments such as light-shining-through-the-wall experiments [178, 179] or cavity resonance searches [180], and astrophysical observables [181]. Many of these experiments are only sensitive to axial interactions or axions decaying into SM final states, which are both absent in the case of the axion-Higgs portal. In the following sections, we present existing bounds on the ratio c_{ah}/f^2 and discuss the best experimental strategy to discover a sterile axion.

4.3.1 Higgs decays

The study of Higgs decays is the most direct way to probe the axion-Higgs portal. The corresponding diagram is the leftmost shown in Figure 4.1 and the decay rates read

$$\Gamma(h \to aa) = \frac{v^2 m_h^3}{32\pi} \frac{c_{ah}^2}{f^4} \left(1 - \frac{2m_a^2}{m_h^2}\right)^2 \sqrt{1 - \frac{4m_a^2}{m_h^2}} \tag{4.3.1}$$

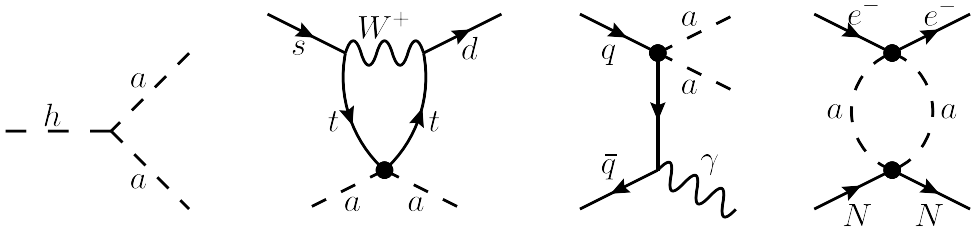

Figure 4.1: Diagrams for different processes induced by the axion-Higgs portal, from left to right: the Higgs decay into two axions, a contribution to the flavour changing transition $s \to daa$, a contribution to the vector meson annihilation $V \to \gamma aa$, and a contribution to the potential between electrons and nuclei generated by the exchange of axion pairs. Bullets indicate effective Higgs-mediated vertices.

experiment	BR($h \to$ inv.)	c_{ah}/f^2[GeV^{-2}]	c_{sh}	ref
LHC (today)	1.45×10^{-1}	7.1×10^{-7}	4.9×10^{-3}	[182]
HL-LHC	2×10^{-2}	2.6×10^{-7}	1.8×10^{-3}	[186]
ILC 250 GeV	4.4×10^{-3}	1.2×10^{-7}	8.6×10^{-4}	[187]
FCC-hh	2.5×10^{-4}	3×10^{-8}	2.0×10^{-4}	[188]

Table 4.1: Current limits and projections for experimental bounds on the branching ratio of Higgs bosons to invisible final states, with corresponding maximal constraints on the axion-Higgs c_{ah}/f^2 and scalar Higgs c_{sh} portals couplings.

for the axion-Higgs portal defined in (4.1.2), and

$$\Gamma(h \to ss) = \frac{v^2}{8\pi m_h} c_{sh}^2 \sqrt{1 - 4\frac{m_s^2}{m_h^2}} \tag{4.3.2}$$

for the scalar Higgs portal. In the absence of linear interactions, the axion is stable, leading to invisible Higgs decays. Bounds on the branching ratio are set by searches for invisible decays of Higgs bosons produced in vector-boson fusion BR($h \to$ inv.) $\leq$ 0.145 at ATLAS [182] and BR($h \to$ inv.) ≤ 0.18 at CMS [183] at 95% Confidence level (CL). Global fits result in slightly stronger bounds of BR($h \to$ inv.) ≤ 0.13 at ATLAS [184] and BR($h \to$ inv.) ≤ 0.16 at CMS [185]. The reach of the high luminosity LHC and potential future colliders is given in Table 4.1.

4.3.2 Flavour-Violating Meson Decays

Some of the most sensitive probes of axions or ALPs in the mass range $m_a = 1-100$ MeV are meson decays like $K^\pm \to \pi^\pm a$ [110, 114, 189]. These decays are however forbidden for the axion-Higgs portal as they violate the Z_2 symmetry. Instead, axions interacting through the axion-Higgs portal are pair-produced in meson decays, such as $K^\pm \to \pi^\pm aa$ induced by so-called penguin diagrams like the second diagram in Figure 4.1. The 3-body phase space leads to a strong suppression of the decay rate

$$\Gamma(K^\pm \to \pi^\pm aa) = \frac{m_{K^\pm}^9}{3 \cdot 2^{13}\pi^3} \frac{c_{ah}^2}{f^4} \frac{c_{ds}^2}{m_h^4} F_3\left(\frac{m_a^2}{m_{K^\pm}^2}, \frac{m_{\pi^\pm}^2}{m_{K^\pm}^2}\right), \tag{4.3.3}$$

where $m_{K^\pm}$ and $m_{\pi^\pm}$ are the charged kaon and pion masses respectively, and c_{ds} the flavour-violating coupling given in (4.2.8). Similar expressions hold for analogous 3-body decays of B mesons. In (4.3.3) we defined the phase space function

$$F_3(a,b) = 24(1-b)^2 \int_{4a}^{\left(1-\sqrt{b}\right)^2} \mathrm{d}x\ (x-2a)^2 \sqrt{x-4a} \sqrt{\left(\frac{1-b-x}{2\sqrt{x}}\right)^2 - b}\,. \tag{4.3.4}$$

with useful limiting forms

$$F_3(a,0) = \sqrt{1-4a}\left(1-10a+42a^2+12a^3\right) - 48a^3\,(2-a)\,\mathrm{arctanh}\,\sqrt{1-4a}\,, \tag{4.3.5a}$$

$$F_3(0,b) = (1-b)^2\left[\left(1-b^2\right)\left(1+28b+b^2\right) + 12b\left(1+3b+b^2\right)\log b\right]. \tag{4.3.5b}$$

In addition to 3-body decays, the axion-Higgs portal predicts flavour-violating decays of neutral mesons to invisible final states. Similar to invisible Higgs decays, it is experimentally very challenging to constrain invisible meson decays unless the meson recoils against SM particles. In B factories, the invisible decay of B^0 mesons can be observed through $e^+e^- \to \Upsilon \to B^0\bar{B}^0$ with a subsequent invisible B^0 decay by tagging the second B^0 meson [190]. The decay rate reads

$$\Gamma(B^0 \to aa) = \frac{m_{B^0}^7}{128\pi} \frac{c_{ah}^2}{f^4} \frac{c_{bd}^2 f_{B^0}^2}{m_h^4} \left(1-\frac{2m_a^2}{m_{B^0}^2}\right)^2 \sqrt{1-\frac{4m_a^2}{m_{B^0}^2}}\,, \tag{4.3.6}$$

where m_{B^0} is the B^0 meson mass, c_{bd} a flavour-violating coupling obtained via (4.2.8),

Decay mode	upper bound	$c_{ah}/f^2[\mathrm{GeV}^{-2}]$	c_{sh}	ref
$\mathrm{BR}(K^\pm \to \pi^\pm + \mathrm{inv.})$	4.8×10^{-11}	1.15×10^{1}	3.4×10^{-1}	[192, 193]
$\mathrm{BR}(B^\pm \to K^\pm + \mathrm{inv.})$	1.6×10^{-5}	6.0×10^{-2}	2.9×10^{-1}	[194]
$\mathrm{BR}(B^\pm \to \pi^\pm + \mathrm{inv.})$	1.4×10^{-5}	2.3×10^{-1}	1.3	[195]
$\mathrm{BR}(B^0 \to \mathrm{inv.})$	2.4×10^{-5}	2.0×10^{-1}	2.7	[190]
$R(\Upsilon \to \gamma + \mathrm{inv})$	1.5×10^{-4}	9.5×10^{-1}	1.7×10^{1}	[196]

Table 4.2: Current experimental bounds on meson decays into final states with invisible particles, with corresponding maximal constraints on the axion-Higgs c_{ah}/f^2 and scalar Higgs c_{sh} portals couplings.

and $f_{B^0} = 190.5\,\mathrm{MeV}$ [191] is the neutral B meson decay constant.

Similarly, we find, for the scalar Higgs portal, the decay rates

$$\Gamma(K^\pm \to \pi^\pm ss) = \frac{m_{K^\pm}^5}{2^{10}\pi^3} \frac{c_{sh}^2 c_{ds}^2}{m_h^4} G_3\left(\frac{m_s^2}{m_{K^\pm}^2}, \frac{m_{\pi^\pm}^2}{m_{K^\pm}^2}\right), \tag{4.3.7}$$

$$\Gamma(B^0 \to ss) = \frac{m_{B^0}^3}{32\pi} \frac{c_{sh}^2 c_{bd}^2 f_{B^0}^2}{m_h^4} \sqrt{1 - 4\frac{m_s^2}{m_{B^0}^2}}, \tag{4.3.8}$$

where the phase space function G_3 is defined as

$$G_3(a,b) = 4(1-b)^2 \int_{4a}^{(1-\sqrt{b})^2} \mathrm{d}x\ \sqrt{x-4a} \sqrt{\left(\frac{1-b-x}{2\sqrt{x}}\right)^2 - b} \tag{4.3.9}$$

and has limiting forms

$$G_3(a,0) = \sqrt{1-4a}\,(1+2a) - 8a\,(1-a)\,\mathrm{arctanh}\,\sqrt{1-4a}\,, \tag{4.3.10a}$$

$$G_3(0,b) = (1-b)^2\left(1 - b^2 + 2b\log b\right). \tag{4.3.10b}$$

Current experimental bounds for the $K^\pm \to \pi^\pm +$ inv., $B^\pm \to K^\pm +$ inv., $B^\pm \to \pi^\pm +$ inv., and $B^0 \to$ inv. decays, as well as the corresponding bounds on the parameters c_{ah}/f^2 and c_{sh} are calculated using meson masses and lifetimes found in [6] and given in Table 4.2.

4.3.3 Radiative Vector Meson Decays

The axion-Higgs portal mediates the flavour-conserving vector meson decays $V \to \gamma aa$ via diagrams like the third one in Figure 4.1. These decays avoid loop suppres-

sion and are proportional to the flavour diagonal couplings (4.2.7), which can be many orders of magnitude larger compared to the flavour violating couplings (4.2.8). In line with the Wilczek equation [197], we use the ratio of decay widths

$$R(V \to \gamma aa) \equiv \frac{\Gamma(V \to \gamma aa)}{\Gamma(V \to e^+e^-)} = \frac{1}{3 \cdot 2^{10}\pi^3\alpha}\frac{c_{ah}^2}{f^4}\frac{m_V^8}{m_h^4}F_3\left(\frac{m_a^2}{m_V^2}, 0\right)\left[1 - \frac{4\alpha_s}{3\pi}a_H(z)\right], \tag{4.3.11}$$

not including contributions suppressed by terms of order $O(c_\gamma)$, for the axion-Higgs portal, and

$$R(V \to \gamma ss) = \frac{1}{2^7\pi^3\alpha}\frac{c_{sh}^2 m_V^4}{m_h^4}G_3\left(\frac{m_s^2}{m_V^2}, 0\right)\left[1 - \frac{4\alpha_s}{3\pi}a_H(z)\right] \tag{4.3.12}$$

for the scalar Higgs portal. We use the Next-to-Leading Order (NLO) corrections $a_H(z)$ where $z = 1 - 4m_a^2/m_V^2$ as given in [198] such that $a_H(1) \approx 10$ for $m_a = 0$ and $a_H(z) \propto z^{-1/2}$ in the limit $m_a \to m_V/2$. The strongest constraints are currently set by BESIII [199] for J/ψ decays and Belle [196] for $\Upsilon(1S)$ decays, the latter of which is also shown in Table 4.2.

4.3.4 Constraints from Spectroscopy

We can also study the effect of the fifth force induced by the exchange of pairs of axions as shown in the last diagram of Figure 4.1 on atomic or molecular systems. The interaction through the axion-Higgs portal is strongly suppressed by the two effective vertices in (4.2.9) proportional to the inverse Higgs mass squared as well as to the small Higgs Yukawa couplings to stable SM particles. Following the method outlined in Section 3.1.2, we derive the IP between a nucleon N and an electron e mediated by a pair of axions,

$$\begin{aligned} V_{ah}(r) = &-\frac{15}{8\pi^3}\frac{c_{ah}^2}{f^4}\frac{c_N m_N m_e}{m_h^4}\frac{1}{r^7} \\ &\times\left[\frac{1}{15}(m_a r)^5 K_1(2m_a r) + \frac{2}{5}(m_a r)^4 K_2(2m_a r) + (m_a r)^3 K_3(2m_a r)\right], \end{aligned} \tag{4.3.13}$$

in agreement with existing literature [124,125,127,138]. We note that, for low axion masses, this potential scales as r^{-7}, in contrast to the IP that we derived in Section

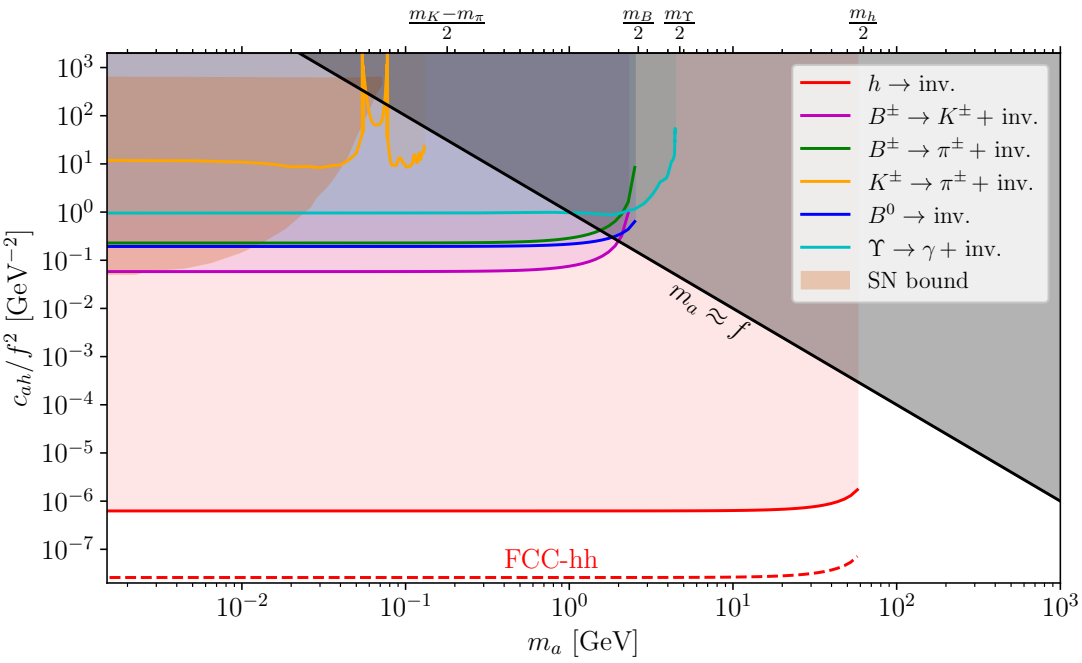

Figure 4.2: Constraints and projections from Higgs and flavour-violating meson decays and bounds from supernova energy loss for the axion-Higgs portal. For the parameter space above the black solid line, the approximate shift symmetry is not a good assumption any more. The supernova bound is taken from [200].

3.2 for an ALP coupling linearly via dimension-5 operators, which scales as r^{-5}. This harsher scaling can be understood as the result of the momentum suppression caused by the derivatives enforcing the shift symmetry in (4.1.2). The IP corresponding to the scalar Higgs portal (4.1.3) takes a form similar to the quadratic scalar potential (3.2.21) and is given by,

$$V_{sh}(r) = -\frac{1}{16\pi^3} c_{sh}^2 \frac{c_N m_N m_e}{m_h^4} \frac{1}{r^3} \left[2 m_s r K_1(2 m_s r)\right] , \tag{4.3.14}$$

which "only" scales as r^{-3}.

Spectroscopic experiments measure atomic or molecular energy transitions with extremely high-precision, and have been proposed as probes of new physics, via the measurement of the change of fundamental constants over time [154], or via fifth force interactions [201]. For the latter, at first order in perturbation theory, the shift in the energy of the $n\ell_j$ state of a hydrogen-like atom is given by the expectation

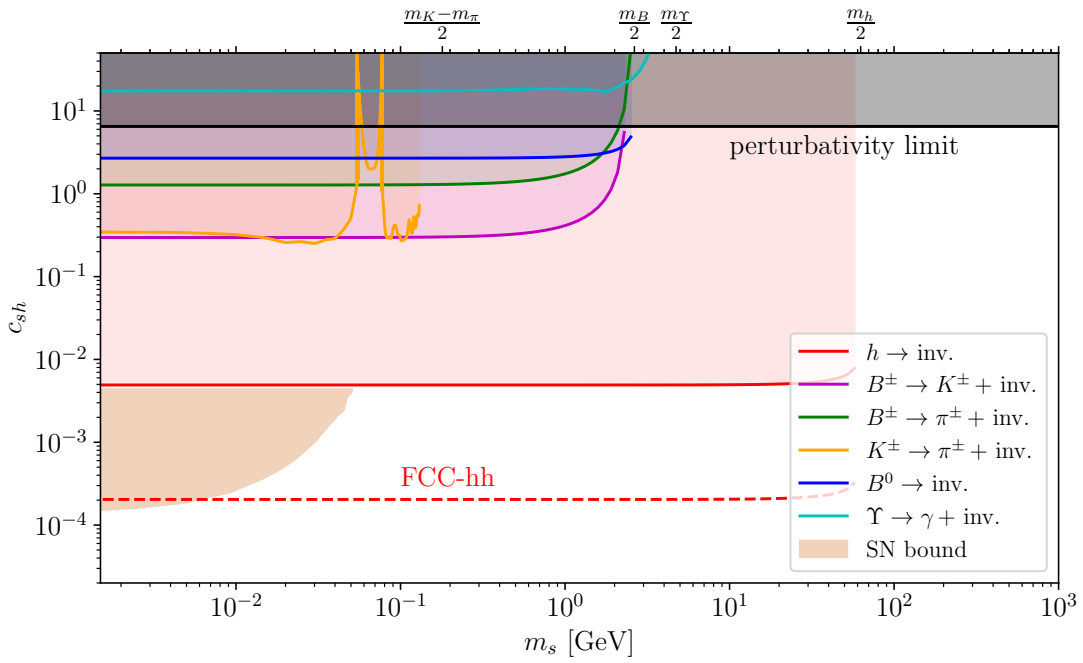

Figure 4.3: Constraints and projections from Higgs and flavour-violating meson decays and bounds from supernova energy loss for the scalar Higgs portal. The region above the black line violates perturbativity. The supernova bound is taken from [200].

value of the corresponding potential with respect to the electronic wavefunction,

$$\Delta E_{n\ell_j} = \langle \psi_{n\ell_j} | V(\boldsymbol{r}) | \psi_{n\ell_j} \rangle = \int \mathrm{d}^3\boldsymbol{r} \; |\psi_{n\ell_j}(\boldsymbol{r})|^2 V(\boldsymbol{r}) \tag{4.3.15}$$

where $\psi_{n\ell_j}(\boldsymbol{r})$ is the hydrogen Schrödinger wavefunction. [202] For a spherically symmetric potential, $V(\boldsymbol{r}) = V(r)$, only the radial component of the wavefunction will enter the calculation; the calculated energy shifts will therefore only depend on the principal and orbital angular momentum quantum numbers n and ℓ.

Using hydrogen-like atoms (or just hydrogen) has the benefit that the theoretical corrections to the wavefunction of a given state are known with extremely high precision [203, 204] allowing strong constraints when considering discrepancies between these predictions and measurements. Errors stemming from uncertainties in fundamental constants, notably the difficulty of measuring the Rydberg constant R_∞ without using transition frequencies, can be minimised by considering ratios of two different atomic transitions; the strongest constraint is currently found by comparing

the $(2s_{1/2} \leftrightarrow 8d_{5/2})$ and $(1s_{1/2} \leftrightarrow 3s_{1/2})$ transition frequencies [205], and reads

$$\left.\frac{E_{2s_{1/2}} - E_{8d_{5/2}}}{E_{1s_{1/2}} - E_{3s_{1/2}}}\right|_{\text{exp}} - \left.\frac{E_{2s_{1/2}} - E_{8d_{5/2}}}{E_{1s_{1/2}} - E_{3s_{1/2}}}\right|_{\text{SM}} < (-0.5 \pm 3.1) \times 10^{-12}\,, \tag{4.3.16}$$

where the experimental values are taken from [204] and the theoretical SM predictions have been calculated using corrections in [203].

The computation of the energy shifts using (4.3.15) is however not straightforward in some cases. The hydrogen electronic wavefunction can be written as a polynomial in r multiplied by an exponential, and at lowest order in r, it scales as $\psi_{n\ell_j}(r) \sim r^\ell e^{-r/2}$. Therefore, evaluating the integral (4.3.15) for a potential scaling as r^{-p} yields terms of the form

$$\int_0^\infty r^2 \mathrm{d}r \left(r^\ell e^{-r/2}\right)^2 r^{-p} = \Gamma\left(3 + 2\ell - p\right)\,, \tag{4.3.17}$$

which is divergent when the argument of the gamma function is non-positive. In other words, in the case of the axion-Higgs IP (4.3.13), which scales as r^{-7}, the calculated energy shifts will be divergent for $\ell \leq 2$ which includes all three states considered in (4.3.16).

This divergence can reasonably be expected to be non-physical and ought to be caused by the breakdown of the effective IP at short distances/high momenta. In the case of an atom, the first effect we expect to change the form of the momentum is the treatment of the nucleus as an extended object at $r \lesssim r_N$; while more generally, the effective interaction will become invalid at $r \lesssim 1/f$ and the low-distance behaviour of the potential will be dictated by higher-order operators in the UV completion. For example, when computing the neutrino IP in Section 3.1.3, considering the weak theory with extended weak boson propagators instead of the four-fermion interaction (3.1.16) yields an IP scaling as $V \sim 1/r$ in the short-distance limit $r \lesssim 1/m_Z$ [206].

Nevertheless, we can regulate these divergences by introducing a cutoff scale r_C on the integral over r following [125, 127, 207]. Using a reference cutoff scale to be the proton radius $r_p = 0.84\,\text{fm}$ [204], (4.3.16) translates into a maximal bound on the

axion coupling at 1σ,

$$\frac{c_{ah}}{f^2} < 4 \times 10^6 \left(\frac{r_C}{r_p}\right)^2 \text{GeV}^{-2}\,, \tag{4.3.18}$$

for $m_a \ll 1/r_p \approx 0.2\,\text{GeV}$, dropping sharply as m_a approaches $1/r_p$. We note that this result strongly depends on the cutoff scale chosen and is therefore not as robust a constraint as the bounds from Higgs and meson decays shown in Figure 4.2. In the case of scalar Higgs portal, the r^{-3} scaling of (4.3.14) yields an approximately logarithmic dependence on the cutoff scale chosen.

A solution to eliminate the divergences and cutoff dependency of the spectroscopic bounds is to consider higher-ℓ states of hydrogen, with ℓ at least 3. Theoretical values can be obtained using [203,208,209], and measurements for the $4f_{5/2}$, $4f_{7/2}$ and $5f_{7/2}$ states can be found in [210]. Considering the $(4f_{7/2} \leftrightarrow 4f_{5/2})$ and $(5f_{7/2} \leftrightarrow 4f_{7/2})$ transitions we find

$$\left.\frac{(E_{4f_{7/2}} - E_{4f_{5/2}})/h}{(E_{5f_{7/2}} - E_{4f_{7/2}})/h}\right|_{\text{exp}-\text{SM}} = (-0.9 \pm 2.1) \times 10^{-8}\,. \tag{4.3.19}$$

Our simple calculation for energy shifts (4.3.15) uses Schrödinger wavefunctions which do not depend on the total angular momentum quantum number j, therefore we need states with at least three distinct n or ℓ numbers to obtain a non-zero shift. Instead, we could use Dirac radial wavefunctions of hydrogen which are functions of n, ℓ and j in the computation of the axion-induced energy shift. [211] However, this causes some issues. First, the energy shifts of two states from a transition $(n\ell_{j_1} \leftrightarrow n\ell_{j_2})$ are very close, leading to worse constraints than a transition between states with different n or ℓ. Then, the Dirac wavefunction of a state $n\ell_{j=\ell-\frac{1}{2}}$ actually scales in r like the Schrödinger wavefunction of the state $n(\ell-1)_j$. In other words, the energy shift for the $4f_{5/2}$ state used in (4.3.19) will still be divergent, and we would actually need to go to $\ell = 4$ states to obtain non-divergent energy shifts, leading to even weaker constraints. To nevertheless obtain an estimate of the bounds for these high-ℓ states, we suppose that a *fictitious* measurement of the $6f_{7/2}$ state has been made with an agreement between experiment and the SM similar to that in (4.3.19)

such that

$$\left.\frac{(E_{5f_{7/2}} - E_{6f_{7/2}})/h}{(E_{4f_{7/2}} - E_{6f_{7/2}})/h}\right|_{\text{exp}-\text{SM}} = (-0.9 \pm 2.1) \times 10^{-8}\,. \tag{4.3.20}$$

The bounds corresponding to this estimate are shown in Figure 4.4.

Molecular spectroscopy can yield stronger constraints at short distances, in particular for systems in which an electron is replaced by a muon whose wavefunction has a larger overlap with the nucleus. It can also offer measurements precise enough to derive bounds on the model. Various systems are considered in [125, 127] with the strongest bound resulting from the binding energy of the $(\nu = 1, J = 0)$ state of the muonic molecular deuterium ion $dd\mu^+$ giving

$$\frac{c_{ah}}{f^2} < 4.4 \times 10^8 \left(\frac{r_C}{r_d}\right)^2 \text{GeV}^{-2}\,, \tag{4.3.21}$$

for a cutoff set at the deuterium radius $r_d = 2.1$ fm [204] and assuming $c_d \approx c_p$ for the deuterium-Higgs coupling. This result is however also strongly dependent on the cutoff scale chosen, as the full integral is divergent for this system [125].

We contrast these constraints with the corresponding results for the Higgs portal scalar. The main difference between the two models is that for interactions induced by the axion-Higgs portal, the bounds obtained from high-ℓ transitions are considerably weaker compared to transitions at low ℓ, whereas the difference is not as extreme in the case of the scalar Higgs portal. This is due to the different scaling of the potentials (4.3.13) and (4.3.14) with r. We also mention the strongest molecular spectroscopy bounds from [125, 127] from the antiprotonic helium molecular ion $\bar{p}\text{He}^+$

$$c_{sh} < 8.4 \times 10^4\,, \tag{4.3.22}$$

for $m_s < 10^4$ eV, and from the $dd\mu^+$ ion with

$$c_{sh} < 2.2 \times 10^5\,, \tag{4.3.23}$$

for $m_s < 10^5$ eV. We note that for the axion-Higgs portal model, the shift-symmetry breaking operator $\frac{m_a^2}{f^2} a^2 \Phi^\dagger \Phi$ always generates the potential (4.3.14) with $c_{sh} =$

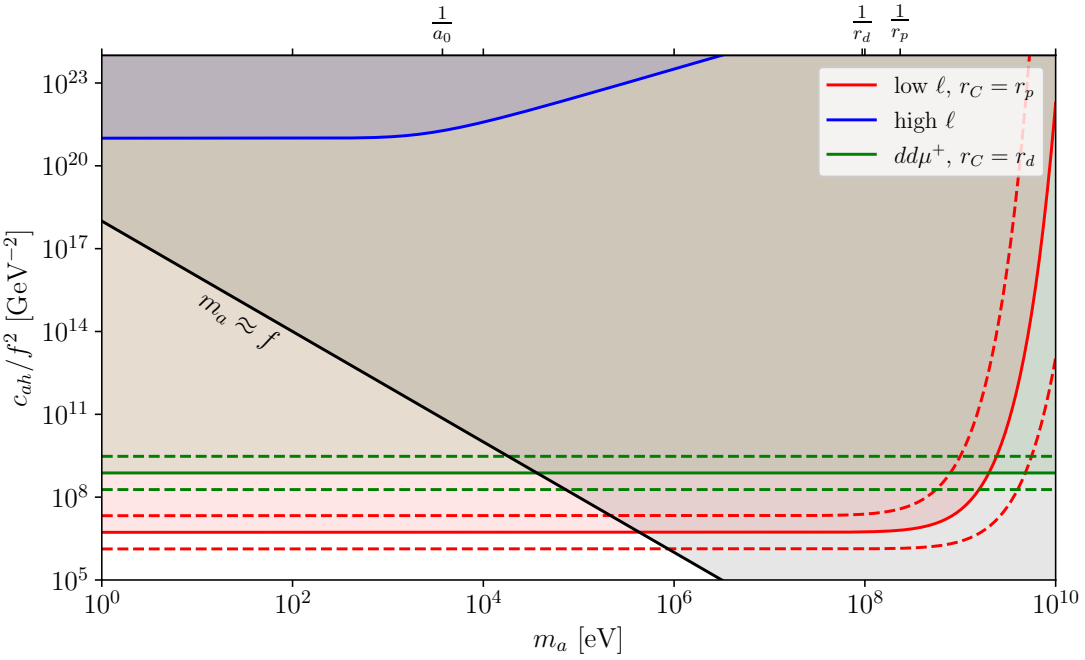

Figure 4.4: Bounds on the axion coupling and scale obtained from spectroscopic data for the axion-Higgs portal. The red bound is obtained from low-ℓ hydrogen states with a cutoff $r_C = r_p$, in blue are the cutoff-independent bounds obtained from $\ell = 3$ hydrogen f-states, and in green that obtained from molecular spectroscopy of the $dd\mu^+$ ion. The dashed lines show the scale dependence of the bounds on the chosen cutoffs with $r_C = 2r_p, r_p/2$ and $r_C = 2r_d, r_d/2$ for the hydrogen and $dd\mu^+$ states respectively. Most of the parameter space is excluded by shift-symmetry breaking operators with $m_a \gtrsim f$ as shown by the black line.

m_a^2/f^2. The bounds on c_{ah}/f^2 in Figure 4.4 are so weak that for some values of m_a, stronger constraints on f could be extracted from the bounds on c_{sh} itself.

4.3.5 Discussion

The different constraints discussed in this section are shown in the $m_a - c_{ah}/f^2$ plane in Figure 4.2, including supernova bounds from [200]. Given the hierarchy in precision between the constraints, one would expect that low-energy experiments give stronger bounds for sufficiently small axion masses. However, due to the powerful double suppression by the axion derivative couplings and the factor $1/m_h^2$ in

the effective couplings, invisible Higgs boson decays result in the strongest bound $c_{ah}/f^2 \lesssim 10^{-6}\,\mathrm{GeV}^{-2}$ for the axion mass range where the decay is allowed. This bound is considerably stronger than bounds from searches for pair-produced axions in flavour violating or flavour conserving meson decays, as well as the bound from supernova energy loss discussed in [200]. We also note that the strength of the constraints from the meson decays correspond to an energy scale $f \lesssim 10\,\mathrm{GeV} \approx m_{B,\Upsilon}$ for a coupling $c_{ah} \approx 1$, and one must be careful before taking these bounds at face value. In order for the effective approach to remain valid, we can drive the value of f by requiring a large coupling $c_{ah} \gg 1$. The constraints from atomic spectroscopy are so weak that they do not show up in Figure 4.2; a dedicated plot is shown in Figure 4.4. Note that for some of the values for c_{ah}/f^2 in Figure 4.2 and Figure 4.4 the bounds shown are only qualitative because the effective theory approach is not justified there. The parameter space shown in gray in Figure 4.2 is excluded because the axion mass is larger than the decay constant and the assumption of an approximate shift symmetry is not justified. Axions with masses $m_a \geq m_h/2$ can only be produced in off-shell, invisible decays of the Higgs boson, which provide a significantly weaker bound [212–214]. For comparison, we show the constraints on a scalar Higgs portal with a stable scalar in Figure 4.3. Here the strongest constraint for masses $m_s \gtrsim 50$ MeV is set by the bound on invisible Higgs decays, but for smaller scalar masses the constraint from supernova energy loss is stronger. These results are in stark contrast to axions with an approximate shift symmetry and linear couplings to Standard Model particles, for which flavour constraints are substantially stronger than the constraint from invisible Higgs decays [114].

4.4 Summary

In this chapter, we have introduced the axion-Higgs portal as the leading effective operator describing interactions between SM particles and axions or ALPs respecting the shift symmetry as well as a Z_2 symmetry. We established some of the theoretical

properties of this effective operator. Namely its couplings to d.o.f. present at different energy levels, such as quarks, gauge bosons, and nucleons. We also showed that the axion-Higgs portal is unsuitable to solve the strong CP problem via the PQ mechanism, and therefore cannot be classified as a QCD axion.

In the absence of any additional interaction, the Z_2 symmetry ensures that the axion is stable and can only be produced in pairs. As a result, we found that very precise measurements such as searches for fifth forces do not result in relevant bounds, as the potential induced by the exchange of axion pairs scales as $V(r) \sim r^{-7}$ as a consequence of the derivative axion interaction in the axion-Higgs portal. Similarly, we showed that the production of axions in the decays of pseudoscalar mesons such as $K^{\pm} \to \pi^{\pm} aa$ and $B^0 \to aa$, and vector mesons $V \to \gamma aa$ are suppressed by powers of the meson mass over the UV scale f. Bounds on the UV scale from atomic spectroscopy and meson decays are therefore substantially weaker compared to the bounds from searches for invisible Higgs decays. Invisible Higgs decays provide the strongest constraint on the axion-Higgs portal independent of the axion mass, including astrophysical constraints from supernova cooling.

Chapter 5

The Dark Stodolsky Effect

5.1 Motivation

Recalling the discussion in Section 2.3, we justified the existence of DM through gravitational interactions, leaving the details of its interactions with the SM unclear and unconstrained. We considered some of the properties of a specific class of DM candidates, QCD axions and ALPs, in the previous chapters; the methods used are however not straightforwardly applicable to other candidates as they rely on model specific properties. Instead, we use the framework of EFTs, which have already proven to be an incredibly powerful tool to constrain DM in a model-independent way [215–218]; by making use of the symmetries of the interaction Lagrangian, EFTs reduce the landscape of underlying theories to a finite number of permitted operators. These operators are typically classified by the spin of the DM particle, along with their mass dimension and coupling to the SM, which can then be constrained and mapped onto the candidate DM theory on a case-by-case basis.

In this chapter, we propose two experiments to observe a spin-dependent energy shift induced by a DM background, which is more commonly known as the Stodolsky effect [219]. As we will see in the following section, the Stodolsky effect has several features which make it a promising avenue for DM detection. First, unlike scattering, the magnitude of the energy shift depends on the DM-SM coupling linearly rather

than quadratically, leading to an effect which is less suppressed by small coupling constants. Second, while many detection techniques depend heavily on the mass of the DM particle under consideration, the Stodolsky effect depends primarily on the velocity of the background particle. For neutrinos, this leads to an energy shift that is largely independent of the neutrino mass [220], which if also true for dark matter would allow us to probe a wide region of parameter space. On the contrary, the Stodolsky effect for neutrinos requires either a neutrino-antineutrino or left-right helicity asymmetry in the background, the former of which is expected to be absent in the standard Cosmic Neutrino Background (CνB) scenario [221]. As we will see, analogous requirements persist for DM backgrounds, potentially restricting the range of models that can give rise to the Stodolsky effect. Even so, both chiral and asymmetric [222] models of DM exist, which, alongside models with finite chemical potentials, generate an asymmetry during DM production. We additionally note that there are several mechanisms, such as finite chemical potentials, DM reflection at the surface of the Earth [223], or gravitational potentials [224], through which either asymmetry may develop post-production.

In Section 5.2 we review the Stodolsky effect for neutrinos and introduce the general formalism that will be used throughout this chapter. Following this, in Section 5.3 we compute the magnitude of the Stodolsky effect for all effective DM operators ranging from spin-0 to spin-$\frac{3}{2}$, up to dimension-6. Finally, we will discuss the experimental signatures of the Stodolsky effect and the feasibility of this technique for DM detection in Section 5.4.

5.2 The Stodolsky Effect

We begin by reviewing the Stodolsky effect for the CνB, which has been discussed in several previous works [219, 220, 225, 226]. This will closely follow the formalism of [220], with the exception that we more carefully treat the external states as partially localised wavepackets, rather than eigenstates of definite momentum. Ad-

ditionally, we assume that the neutrinos are monochromatic in the CνB reference frame, which is a good approximation when their momentum distribution is narrow.

Working in the mass basis and starting from the neutrino interaction term (3.1.16), the effective low-energy Hamiltonian density for neutrino-electron interactions is

$$\mathcal{H}_{\rm int}(x) = \frac{G_F}{\sqrt{2}} \sum_{i,j} \bar{\nu}_i \gamma_\mu \left(1 - \gamma^5\right) \nu_j \bar{e} \gamma^\mu \left(g_{ij}^V - g_{ij}^A \gamma^5\right) e \,, \tag{5.2.1}$$

where G_F is the Fermi constant, g_{ij}^V and g_{ij}^A are the effective electron vector and axial couplings defined in (3.1.18), and $i, j \in \{1, 2, 3\}$ denote the neutrino mass eigenstates. To leading order in $\mathcal{H}_{\rm int}$, the energy shift of the electron helicity state h_e is given by

$$\Delta E_e(\boldsymbol{p}_e, h_e) = \sum_{\nu,i,h_\nu} \sum_{N_\nu} \left\langle e_{h_e}, \nu_{i,h_\nu} \left| \int \mathrm{d}^3\boldsymbol{x}\, \mathcal{H}_{\rm int}(x) \right| e_{h_e}, \nu_{i,h_\nu} \right\rangle \,, \tag{5.2.2}$$

where h_e and h_ν denote the electron and neutrino helicities respectively, and $\sum_\nu$ is a sum over neutrinos and antineutrinos. Similarly, $\sum_{N_\nu}$ is a sum over all neutrinos in the background with the d.o.f. specified by the preceding sum. The fermionic external states are incoherent superpositions of momentum eigenstates, defined by [117, 118, 227]

$$|\psi_h\rangle \equiv |\psi(p, x, h)\rangle = \int \frac{\mathrm{d}^3\boldsymbol{q}}{(2\pi)^3} \frac{1}{\sqrt{2E_q}}\, \omega_\psi(p, q) e^{-i\boldsymbol{q}\cdot\boldsymbol{x}} \, |\{q, h\}\rangle \,, \tag{5.2.3}$$

with $\psi \in \{e, \nu\}$, where E_q is the energy of the momentum eigenstate with momentum q, and ω_ψ is a wavepacket function centred on the momentum p. The wavepacket states are normalised to unity, which also sets the normalisation of ω_ψ,

$$\int \frac{\mathrm{d}^3\boldsymbol{q}}{(2\pi)^3} \, |\omega_\psi(p, q)|^2 = 1 \,. \tag{5.2.4}$$

For the momentum eigenstates, we use the relativistic normalisation

$$|\{p, h\}\rangle = \sqrt{2E_p}\, a_\psi^\dagger(\boldsymbol{p}, h)|0\rangle \,, \tag{5.2.5}$$

where $a_\psi^\dagger(\boldsymbol{p}, h)$ is the particle creation operator for species ψ with momentum and helicity $\boldsymbol{p}$ and h respectively, while its Hermitian conjugate is the corresponding

annihilation operator. We denote the antiparticle creation and annihilation operators with $b_\psi^\dagger$ and b_ψ, respectively. These operators all satisfy the anticommutation relations

$$\left\{a_i(\boldsymbol{p},h), a_j^\dagger(\boldsymbol{q},h')\right\} = \left\{b_i(\boldsymbol{p},h), b_j^\dagger(\boldsymbol{q},h')\right\} = (2\pi)^3\delta^{(3)}(\boldsymbol{p}-\boldsymbol{q})\delta_{ij}\delta_{hh'}\,, \tag{5.2.6}$$

with all other anticommutators equal to zero. Finally, the fermion field operators are decomposed as

$$\psi(x) = \int \frac{\mathrm{d}^3\boldsymbol{p}}{(2\pi)^3}\frac{1}{\sqrt{2E_p}}\sum_h \left(a_\psi(\boldsymbol{p},h)u_\psi(p,h)e^{-ip\cdot x} + b_\psi^\dagger(\boldsymbol{p},h)v_\psi(p,h)e^{ip\cdot x}\right)\,, \tag{5.2.7a}$$

$$\bar\psi(x) = \int \frac{\mathrm{d}^3\boldsymbol{p}}{(2\pi)^3}\frac{1}{\sqrt{2E_p}}\sum_h \left(a_\psi^\dagger(\boldsymbol{p},h)\bar u_\psi(p,h)e^{ip\cdot x} + b_\psi(\boldsymbol{p},h)\bar v_\psi(p,h)e^{-ip\cdot x}\right)\,, \tag{5.2.7b}$$

for Dirac fermions, where u_ψ and v_ψ are positive and negative frequency Dirac spinors respectively. The corresponding field decompositions for Majorana fermions are found by setting $b_\psi = a_\psi$ in (5.2.7). Expanding out (5.2.2), we find[1]

$$\begin{aligned}\Delta E_e(\boldsymbol{p}_e,h_e)\big|_{\boldsymbol{x}_e,\boldsymbol{x}_\nu} = \sum_{\nu,i,h_\nu}\sum_{N_\nu}\int \mathrm{d}^3\boldsymbol{x}\,\mathrm{d}\Pi\;&\omega_e(p_e,q_e)\omega_e^*(p_e,q_e')e^{-i(\boldsymbol{q}_e-\boldsymbol{q}_e')\cdot\boldsymbol{x}_e}\\ &\times\omega_\nu(p_\nu,q_\nu)\omega_\nu^*(p_\nu,q_\nu')e^{-i(\boldsymbol{q}_\nu-\boldsymbol{q}_\nu')\cdot\boldsymbol{x}_\nu}\\ &\times\left\langle\left\{q_e',h_e\right\},\left\{q_\nu',h_\nu\right\}\middle|\,\mathcal{H}_{\mathrm{int}}(x)\,|\{q_\nu,h_\nu\},\{q_e,h_e\}\right\rangle\,,\end{aligned} \tag{5.2.8}$$

where we have introduced the shorthand

$$\mathrm{d}\Pi = \frac{\mathrm{d}^3\boldsymbol{q}_e}{(2\pi)^3}\frac{\mathrm{d}^3\boldsymbol{q}_e'}{(2\pi)^3}\frac{\mathrm{d}^3\boldsymbol{q}_\nu}{(2\pi)^3}\frac{\mathrm{d}^3\boldsymbol{q}_\nu'}{(2\pi)^3}\frac{1}{\sqrt{2E_{q_e}}}\frac{1}{\sqrt{2E_{q_e'}}}\frac{1}{\sqrt{2E_{q_\nu}}}\frac{1}{\sqrt{2E_{q_\nu'}}}\,. \tag{5.2.9}$$

In line with [117,227], we now average ΔE_e over the regions in which the wavepackets are localised, i.e. we take

$$\Delta E_e(\boldsymbol{p}_e,h_e)\big|_{\boldsymbol{x}_e,\boldsymbol{x}_\nu} \to \frac{1}{V^2}\int \mathrm{d}^3\boldsymbol{x}_e\,\mathrm{d}^3\boldsymbol{x}_\nu\;\Delta E_e(\boldsymbol{p}_e,h_e)\big|_{\boldsymbol{x}_e,\boldsymbol{x}_\nu}\,, \tag{5.2.10}$$

[1] For notational clarity, we suppress the neutrino indices i in equations from now on, $q_{\nu_i}\to q_\nu$ and so on.

which allows us to eliminate two of the momentum integrals, giving

$$\Delta E_e(\boldsymbol{p}_e, h_e) = \sum_{\nu,i,h_\nu} \sum_{N_\nu} \frac{1}{4V^2} \int \mathrm{d}^3\boldsymbol{x}\, \frac{\mathrm{d}^3\boldsymbol{q}_e}{(2\pi)^3 E_e} \frac{\mathrm{d}^3\boldsymbol{q}_\nu}{(2\pi)^3 E_\nu}\, |\omega_e(p_e, q_e)|^2 |\omega_\nu(p_\nu, q_\nu)|^2 \langle \mathcal{H}_{\mathrm{int}} \rangle \,, \tag{5.2.11}$$

with the dimensionless quantity

$$\langle \mathcal{H}_{\mathrm{int}} \rangle = \langle \{q_e, h_e\}, \{q_\nu, h_\nu\} |\, \mathcal{H}_{\mathrm{int}}(x)\, | \{q_\nu, h_\nu\}, \{q_e, h_e\} \rangle \,. \tag{5.2.12}$$

Recalling the normalisation of the wavepacket function ω allows us to identify $|\omega(p,q)|^2/V$ as the phase space density for a single particle. The sum over all particles in the background can therefore be used to replace the wavepacket functions with momentum distribution functions

$$\sum_{N_\nu} \frac{|\omega_\nu(p_\nu, q_\nu)|^2}{V} = n_\nu(\nu_{i,h_\nu}) f_\nu(\boldsymbol{q}_\nu) \qquad \frac{|\omega_e(p_e, q_e)|^2}{V} = \frac{1}{V} (2\pi)^3 \delta^{(3)}(\boldsymbol{p}_e - \boldsymbol{q}_e) \,, \tag{5.2.13}$$

where $n_\nu(\nu_{i,h_\nu})$ is the number density of background neutrino eigenstate i with helicity h_ν. Finally, after noting that nothing in $\langle \mathcal{H}_{\mathrm{int}} \rangle$ depends on position and considering an electron at rest in the lab frame, we find

$$\begin{aligned} \Delta E_e(\boldsymbol{0}, h_e) &= \frac{1}{4m_e} \sum_{\nu,i,h_\nu} n_\nu(\nu_{i,h_\nu}) \int \frac{\mathrm{d}^3\boldsymbol{q}_\nu}{(2\pi)^3} f_\nu(\boldsymbol{q}_\nu) \frac{1}{E_\nu}\, \langle \mathcal{H}_{\mathrm{int}} \rangle|_{|\boldsymbol{p}_e|=0} \\ &\equiv \frac{1}{4m_e} \sum_{\nu,i,h_\nu} n_\nu(\nu_{i,h_\nu}) \left\langle \frac{1}{E_\nu} \langle \mathcal{H}_{\mathrm{int}} \rangle \right\rangle \,, \end{aligned} \tag{5.2.14}$$

where m_e is the electron mass and the outermost angled brackets denote an averaged quantity, which must be done in order to account for the motion of the Earth relative to the CνB reference frame. The averaging procedure differs slightly between the CνB and DM, as we do not know the velocity of the former. We therefore use the flux averages method from [220] for the CνB, while those for DM are discussed in Appendix C.

Expanding out the external states with (5.2.5), applying the appropriate anticommutation relations (5.2.6) and taking the traces of Dirac spinor chains yields [220]

$$\langle \mathcal{H}_{\mathrm{int}} \rangle = 2\sqrt{2} G_F g^A_{ii} m_e h_e \left[m_\nu h_\nu (S_e \cdot S_\nu) - (S_e \cdot p_\nu) \right] + f(g^V_{ii}) \,, \tag{5.2.15}$$

where $h = \pm 1$ denotes the particle spin eigenvalue, m_{ν_i} denotes the neutrino mass and $f(V_{ii})$ contains terms that do not depend on the electron spin, which will not contribute to the Stodolsky effect. Note that (5.2.15) takes the opposite sign for external antineutrino states, while for external Majorana neutrino states the expectation value is twice as large. For a massive particle with four-spin $S^\mu_{\text{rest}} = (0, \boldsymbol{s})$ in its rest frame, its four-spin in the reference frame where it has momentum $\boldsymbol{p}$ is found by boosting S^μ_{rest} into this frame and reads

$$S^\mu = \left(\frac{\boldsymbol{p}\cdot\boldsymbol{s}}{m},\ \boldsymbol{s} + \frac{\boldsymbol{p}\cdot\boldsymbol{s}}{m(E+m)}\,\boldsymbol{p} \right) . \tag{5.2.16}$$

By inspection, we see that S^μ satisfies $S^2 = -|\boldsymbol{s}|^2$ and $p \cdot S = 0$. If we restrict our discussion to helicity eigenstates then $\boldsymbol{s}$ will be directed along $\boldsymbol{p}$, such that (5.2.16) reduces to

$$S^\mu = \left(\frac{|\boldsymbol{p}|}{m},\ \frac{E}{m}\frac{\boldsymbol{p}}{|\boldsymbol{p}|} \right) , \tag{5.2.17}$$

and we instead identify $h = \pm 1$ with the particle helicity.[2] Naturally, we cannot use (5.2.17) for a particle at rest.

The energy splitting between the two electron spin states is then found by taking the difference between the energy shifts for each spin state, which after performing the flux averaging on (5.2.15) gives

$$\begin{aligned}\Delta E_e^D = \frac{\sqrt{2}G_F}{3}|\boldsymbol{\beta}_\oplus| \sum_i A_{ii} \Bigg[& 2\sum_{s_\nu} \left(2 - |\boldsymbol{\beta}_\nu|^2\right) \left(n_\nu(\nu^D_{i,s_\nu}) - n_\nu(\bar{\nu}^D_{i,s_\nu} \right) \\ & + \frac{1}{|\boldsymbol{\beta}_\nu|} \left(3 - |\boldsymbol{\beta}_\nu|^2\right) \left(n_\nu(\nu^D_{i,L}) - n_\nu(\nu^D_{i,R}) + n_\nu(\bar{\nu}^D_{i,R}) - n_\nu(\bar{\nu}^D_{i,L}) \right) \Bigg] , \end{aligned} \tag{5.2.18}$$

for a Dirac neutrino background, where the subscripts L and R denote left and right *helicity* neutrinos respectively, with R/L corresponding to $h_\nu = \pm 1\,(\mp 1)$ for (anti)neutrinos. Additionally, $\boldsymbol{\beta}_\oplus$ is the relative velocity between the Earth and CνB reference frame, which may be time-dependent, and $\boldsymbol{\beta}_\nu$ is the lab frame neutrino velocity. For completeness, we note that while the term scaling as $|\boldsymbol{\beta}_\nu|^{-1}$ appears divergent, it in fact tends to zero as $|\boldsymbol{\beta}_\nu| \to 0$ as a consequence of a vanishing

[2] For simplicity, we will only consider helicity eigenstates for the remainder of this discussion.

helicity asymmetry for slow neutrinos.[3] Similarly, we find for a Majorana neutrino background

$$\Delta E_e^M = \frac{2\sqrt{2}G_F}{3}|\boldsymbol{\beta}_\oplus| \sum_i \frac{A_{ii}}{|\boldsymbol{\beta}_\nu|}\left(3 - |\boldsymbol{\beta}_\nu|^2\right)\left(n_\nu(\nu_{i,L}^M) - n_\nu(\nu_{i,R}^M)\right) . \tag{5.2.19}$$

We immediately see that the Stodolsky effect for neutrinos requires either a non-zero neutrino-antineutrino or helicity asymmetry, but depends only on the neutrino velocity and scales linearly with G_F. These features, if present in an analogue effect for DM, would allow an experiment utilising the Stodolsky effect to probe a vast region of DM parameter space, as the effect is less suppressed than scattering in weakly coupled regions, whilst only depending on the dark matter velocity, $|\boldsymbol{\beta}_{\rm DM}| \simeq 1.2 \times 10^{-3}$ [57], independent of the DM mass.

We are now ready to move onto the Stodolsky effect for DM, henceforth referred to as the *Dark Stodolsky Effect (DSE)* to distinguish it from the effect for neutrinos, which we will explicitly call the *Neutrino Stodolsky Effect (νSE)*. By analogy with (5.2.2), the energy shift of a SM fermion ψ at rest in a DM background will be given by

$$\Delta E_\psi(\mathbf{0}, h_\psi) = \frac{1}{4m_\psi}\sum_{\text{d.o.f.}} n_{\rm DM}\left\langle \frac{1}{E_{\rm DM}}\langle \mathcal{H}_{\rm int}\rangle \right\rangle , \tag{5.2.20}$$

where the sum runs over all the DM degrees of freedom. For the remainder of this chapter we will focus on the object appearing inside the angled brackets, which will typically be some kinematic structure depending on the effective DM operator under consideration. When evaluating these expectation values we will only keep the terms that depend on S_ψ, as no other terms will contribute to the DSE. The energy splitting of the two SM fermion spin states can then found by starting with (5.2.20), and then taking the difference in the energy shifts for the two spin states. This will typically enter as an overall factor of two.

[3] The apparent divergence is an artefact of the frame transformation, and is discussed in Section 5.2 and Appendix B of [220].

5.3 Effective Dark Matter Operators

We now turn our attention to the landscape of effective DM operators that can give rise to the DSE. For the remainder of this work, we will consider an effective DM Lagrangian of the form

$$\mathcal{L}_{\rm DM} = \mathcal{L}_{\rm SM} + \mathcal{L}_{\rm kin} + \mathcal{L}_{\rm int}, \tag{5.3.1}$$

where $\mathcal{L}_{\rm SM}$ is the complete SM Lagrangian, $\mathcal{L}_{\rm kin}$ contains the kinetic and mass terms for the DM field, and $\mathcal{L}_{\rm int}$ contains effective SM-DM interaction operators. This will take the form

$$\mathcal{L}_{\rm int} = -\frac{g_{\psi\chi}}{\Lambda^{d-4}}\mathcal{O}_{\rm DM}^{\mu\nu\ldots}\mathcal{O}_{\mu\nu\ldots}^{\rm SM}\,, \tag{5.3.2}$$

where $g_{\psi\chi}$ denotes the coupling between the SM fermion and DM field, Λ is the new physics scale, and d is the combined mass dimension of the SM and DM effective operators, $\mathcal{O}_{\rm SM}$ and $\mathcal{O}_{\rm DM}$ respectively. We will only work with Lagrangians that are Lorentz invariant, Hermitian, invariant under the SM gauge group and irreducible by the equations of motion. By inspection of the expectation value, we immediately see that in order for an operator to contribute to the DSE it must contain at least two copies of the field operator corresponding to each external field. For bosonic DM, this gives a minimum combined mass dimension for $\mathcal{O}_{\rm SM}$ and $\mathcal{O}_{\rm DM}$ of $d = 5$, while for fermionic DM, the minimum mass dimension is $d = 6$. As such, we include *all* effective DM operators up to $d = 6$; we however do not consider DM operators with $d > 6$, which become increasingly suppressed by the new physics scale Λ with increasing d.

For an operator $\mathcal{O}_{\rm SM} \sim \bar{\psi}\Gamma_{\mu\nu\ldots}\psi$, where $\Gamma_{\mu\nu\ldots}$ is an arbitrary Dirac matrix structure, after expanding out the field operators and external states, and applying the appropriate (anti)commutation relations, we find the general form for the expectation value containing a trace over the SM fermion Dirac structure

$$\langle\mathcal{H}_{\rm int}\rangle = \frac{g_{\psi\chi}}{\Lambda^{d-4}}P_{\rm DM}^{\mu\nu\ldots}\cdot{\rm Tr}\left[u_\psi\bar{u}_\psi\Gamma_{\mu\nu\ldots}\right]\,, \tag{5.3.3}$$

where $P_{\rm DM}$ contains details of the DM kinematics, and may itself contain Dirac

traces, and we have used the shorthand $u_\psi \equiv u_\psi(p_\psi, s_\psi)$ for the Dirac spinors. The trace can be simplified in a basis independent way be making use of the identities

$$u(p,h)\bar{u}(p,h') = \frac{1}{2}(\not{p} + m)(1 + h\gamma^5 \not{S})\delta_{hh'}\,, \tag{5.3.4a}$$

$$v(p,h)\bar{v}(p,h') = \frac{1}{2}(\not{p} - m)(1 + h\gamma^5 \not{S})\delta_{hh'}\,. \tag{5.3.4b}$$

There are a total of five independent gamma matrix structures that can be included in the fermion trace

$$1, \quad \gamma^5, \quad \gamma^\mu, \quad \gamma^\mu\gamma^5, \quad \sigma^{\mu\nu}, \tag{5.3.5}$$

with $\sigma^{\mu\nu} = \frac{i}{2}[\gamma^\mu, \gamma^\nu]$. Of these, only some will give rise to expectation values that depend on the SM fermion spin, and the remainder can be neglected. Explicitly, we find

$$\mathrm{Tr}\left[u_\psi \bar{u}_\psi\right] = 2m_\psi \tag{5.3.6a}$$

$$\mathrm{Tr}\left[u_\psi \bar{u}_\psi \gamma^5\right] = -2h_\psi p_\psi \cdot S_\psi = 0 \tag{5.3.6b}$$

$$\mathrm{Tr}\left[u_\psi \bar{u}_\psi \gamma^\mu\right] = 2p_\psi^\mu \tag{5.3.6c}$$

$$\mathrm{Tr}\left[u_\psi \bar{u}_\psi \gamma^\mu\gamma^5\right] = 2m_\psi h_\psi S_\psi^\mu \tag{5.3.6d}$$

$$\mathrm{Tr}\left[u_\psi \bar{u}_\psi \sigma^{\mu\nu}\right] = -2h_\psi \varepsilon^{\alpha\beta\mu\nu} p_{\psi\alpha} S_{\psi\beta} \tag{5.3.6e}$$

where $\varepsilon^{\alpha\beta\mu\nu}$ is the Levi-Civita tensor, such that of the five independent gamma matrix structures appearing in (5.3.5), we only need to consider $\gamma^\mu\gamma^5$ and $\sigma^{\mu\nu}$. Therefore, excluding field indices, we realise that the Lorentz structures that can enter into effective DM operators are the ones already given in (5.3.5), along with the partial derivative ∂_μ, and the Levi-Civita tensor $\varepsilon_{\alpha\beta\mu\nu}$ mentioned earlier. Considering operators up to dimension-6 with a fermionic SM part, we can have at most a single derivative entering. As such, for spin-0 and spin-$\frac{1}{2}$ DM candidates, the only way that the Levi-Civita tensor can enter a Lagrangian is through operators that contain at least three gamma matrices; which can then be reduced to simpler Lorentz structures via the Chisholm identity,

$$\gamma^\alpha\gamma^\beta\gamma^\mu = g^{\alpha\beta}\gamma^\mu + g^{\beta\mu}\gamma^\alpha - g^{\alpha\mu}\gamma^\beta - i\varepsilon^{\sigma\alpha\beta\mu}\gamma_\sigma\gamma^5\,, \tag{5.3.7}$$

where $g^{\mu\nu}$ is the metric tensor. Including the Levi-Civita tensor in the list of Lorentz structures we can use in the $\mathcal{O}_{\rm SM}$ part of the operators, we find that there exists an additional Lorentz invariant structure that we need to consider which includes contractions of a Levi-Civita tensor and a sigma tensor $\sigma^{\mu\nu}$, which will clearly depend on S_ψ. Using the Chisholm identity (5.3.7) we can derive the identity

$$\varepsilon_{\alpha\beta\mu\nu}\sigma^{\mu\nu} = -2i\sigma_{\alpha\beta}\gamma^5 \tag{5.3.8}$$

which allows us to rewrite this new operator in terms of γ^5 as

$$\varepsilon_{\alpha\beta\mu\nu}P^{\alpha\beta}_{\rm DM}\bar{u}_\psi\sigma^{\mu\nu}u_\psi = -2iP^{\mu\nu}_{\rm DM}\bar{u}_\psi\sigma_{\mu\nu}\gamma^5 u_\psi\,, \tag{5.3.9}$$

and so we will consider the structure $\bar{\psi}\sigma^{\mu\nu}\gamma^5\psi$ as an additional "independent" operator throughout, with

$$\mathrm{Tr}\left[u_\psi\bar{u}_\psi\sigma^{\mu\nu}\gamma^5\right] = 2ih_\psi\left(p^\mu_\psi S^\nu_\psi - S^\mu_\psi p^\nu_\psi\right)\,. \tag{5.3.10}$$

Many operators containing derivatives can be reduced using conserved currents, and through integration by parts. Take, for example, the scalar operator

$$\left(\partial_\mu|\phi|^2\right)\bar{\psi}\gamma^\mu\gamma^5\psi = \partial_\mu\left[|\phi|^2\bar{\psi}\gamma^\mu\gamma^5\psi\right] - |\phi|^2\partial_\mu\left(\bar{\psi}\gamma^\mu\gamma^5\psi\right). \tag{5.3.11}$$

The first term on the right-hand side is a total derivative and so will not contribute to the classical action, while the second term contains the derivative of the axial current which can be re-expressed as $2im_\psi|\phi|^2\bar{\psi}\gamma^5\psi$ using the equations of motion for spin-$\frac{1}{2}$ fields. We can therefore perform the operator reduction

$$\left(\partial_\mu|\phi|^2\right)\bar{\psi}\gamma^\mu\gamma^5\psi \rightsquigarrow |\phi|^2\bar{\psi}\gamma^5\psi, \tag{5.3.12}$$

which as per (5.3.6) does not contribute to the DSE. Note that similar structures containing vector currents vanish from the requirement $\partial_\mu(\bar{\psi}\gamma^\mu\psi) = 0$. Further reductions in the effective operator basis can be obtained using equations of motion for the relevant field.

Finally, we note that there are several operator combinations, e.g.

$$\mathcal{O}_{\rm DM}\mathcal{O}_{\rm SM} = |\phi|^2\bar{\psi}\gamma^5\psi = |\phi|^2\bar{\psi}_L\psi_R + \dots\,, \tag{5.3.13}$$

containing some complex scalar DM field ϕ, that couple left to right-chiral SM fermions and appear to be dimension-5. However, in order for the SM component to be gauge invariant under $\mathrm{SU}(2)_L$, we require an additional insertion of the SM fermion mass. As a result, if $\Lambda \gg m_\psi$, the operator will effectively scale as one of dimension-6. However, as we do not specify the new physics scale, we will treat such operators as dimension-5 throughout. By extension, we will define the dimension of any operator considered in the remainder of this work as the sum of the mass dimensions of its field content and the number of derivatives.

The operator bases used throughout this chapter are those in which the equations of motion have been applied maximally. This avoids the need to apply Hamilton's equations to the Hamiltonian when computing the energy shifts, which is a far more involved task than using the Euler-Lagrange equations. For completeness, we also specify the spin-independent members of our operator bases: at spin-0, these are $|\phi|^2\bar{\psi}\psi$, $i|\phi|^2\bar{\psi}\gamma^5\psi$, and $i(\phi^\dagger\overset{\leftrightarrow}{\partial_\mu}\phi)(\bar{\psi}\gamma^\mu\psi)$; for spin-1 DM, we have $|X|^2\bar{\psi}\psi$, $i|X|^2\bar{\psi}\gamma^5\psi$, along with the vector current analogues of each axial-vector operator appearing in Table 5.2, made Hermitian with appropriate factors of the imaginary unit. Finally, the full spin-$\frac{1}{2}$ basis includes products of fermion bilinears not given in Table 5.1, while the complete basis for spin-$\frac{3}{2}$ fermions is given in [228]. The same spin-0 basis, along with a similar spin-1 basis can also be found in [229].

5.3.1 Spin-0

New scalar fields are popular candidates for DM [99, 230, 231], which typically take the form of axions or Higgs-like particles. The latter are Higgs-like extensions to the SM and require very few additional parameters. In fact, a real singlet scalar coupled to the SM Higgs is the minimal renormalisable extension to the SM capable

of explaining DM [161].

In our EFT approach, we will make no reference to the underlying theory and simply consider some complex scalar field ϕ, for which the corresponding field decompositions are

$$\phi(x) = \int \frac{\mathrm{d}^3\boldsymbol{p}}{(2\pi)^3}\frac{1}{\sqrt{2E_p}}\left(a(\boldsymbol{p})e^{-ip\cdot x} + b^\dagger(\boldsymbol{p})e^{ip\cdot x}\right) , \tag{5.3.14a}$$

$$\phi^*(x) = \int \frac{\mathrm{d}^3\boldsymbol{p}}{(2\pi)^3}\frac{1}{\sqrt{2E_p}}\left(a^\dagger(\boldsymbol{p})e^{ip\cdot x} + b(\boldsymbol{p})e^{-ip\cdot x}\right) , \tag{5.3.14b}$$

and the analogous field decomposition for a real scalar DM candidate is found by setting $b = a$. Unlike neutrinos, the creation and annihilation operators for bosonic DM follow commutation relations

$$\left[a_i(\boldsymbol{p}), a_j^\dagger(\boldsymbol{q})\right] = \left[b_i(\boldsymbol{p}), b_j^\dagger(\boldsymbol{q})\right] = (2\pi)^3\delta^{(3)}(\boldsymbol{p}-\boldsymbol{q})\delta_{ij} , \tag{5.3.15}$$

with all other commutators equal to zero. As it turns out, there is only one scalar operator up to dimension-6 that gives rise to the DSE, with interaction Lagrangian

$$\mathcal{L}_{\text{int}}^{\phi} = -\frac{ig_{\psi\phi}}{\Lambda^2}(\phi^*\overset{\leftrightarrow}{\partial_\mu}\phi)(\bar{\psi}\gamma^\mu\gamma^5\psi) , \tag{5.3.16}$$

where we use $\phi^*\overset{\leftrightarrow}{\partial_\mu}\phi = \phi^*(\partial_\mu\phi) - (\partial_\mu\phi^*)\phi$. The corresponding Hamiltonian density is found via a Legendre transformation,

$$\mathcal{H}_{\text{int}}^{\phi} \equiv \sum_\phi \dot{\phi}\frac{\partial\mathcal{L}_{\text{int}}^{\phi}}{\partial\dot{\phi}} - \mathcal{L}_{\text{int}}^{\phi} = \frac{ig_{\psi\phi}}{\Lambda^2}\left(\phi^*(\nabla\phi) - (\nabla\phi^*)\phi\right)\cdot\left(\bar{\psi}\boldsymbol{\gamma}\gamma^5\psi\right) , \tag{5.3.17}$$

where the sum runs over ϕ and ϕ^*. In a background of pure ϕ scalars, the relevant expectation value that contributes to the DSE can be computed using the appropriate field decompositions and commutators defined earlier to find

$$\langle\mathcal{H}_{\text{int}}^{\phi}\rangle = -\frac{2g_{\psi\phi}}{\Lambda^2}\boldsymbol{p}_\phi\cdot\mathrm{Tr}\left[\bar{u}_\psi\boldsymbol{\gamma}\gamma^5 u_\psi\right] = -\frac{4g_{\psi\phi}}{\Lambda^2}m_\psi h_\psi(\boldsymbol{p}_\phi\cdot\boldsymbol{S}_\psi) , \tag{5.3.18}$$

where in going from the first to the second equality we have used one of the trace identities in (5.3.6). If a background of pure ϕ^* scalars is considered instead, the expectation value (5.3.18) takes the opposite sign. Plugging this into (5.2.20), we

find the energy shift of the SM fermion state with spin h_ψ

$$\Delta E^\phi_\psi(\mathbf{0}, h_\psi) = -\frac{g_{\psi\phi}}{\Lambda^2} h_\psi \left\langle \frac{\boldsymbol{p}_\phi \cdot \boldsymbol{S}_\psi}{E_\phi} \right\rangle \left(n_\phi(\phi) - n_\phi(\phi^*) \right) , \tag{5.3.19}$$

with $n_\phi(\phi)$ and $n_\phi(\phi^*)$ the number densities of background species ϕ and ϕ^* respectively. Replacing the average with the corresponding expression found in Appendix C yields

$$\Delta E^\phi_\psi(\mathbf{0}, h_\psi) = -\frac{2 g_{\psi\phi}}{\Lambda^2} h_\psi \beta_\oplus (n_\phi(\phi) - n_\phi(\phi^*)), \tag{5.3.20}$$

where $\beta_\oplus$ is the magnitude of the relative velocity between the laboratory and DM reference frames. By taking the difference between the energy shift for each SM fermion spin state, we find an energy splitting

$$\Delta E^\phi_\psi = \Delta E^\phi_\psi(\mathbf{0}, 1) - \Delta E^\phi_\psi(\mathbf{0}, -1) = -\frac{4 g_{\psi\phi}}{\Lambda^2} \beta_\oplus \left(n_\phi(\phi) - n_\phi(\phi^*) \right) . \tag{5.3.21}$$

The energy splitting (5.3.21) is therefore independent of the DM kinematics, potentially allowing us to constrain scalar DM with masses ranging across many orders of magnitude. Notably however, we still require a matter-antimatter asymmetry in order to generate a DSE for scalar DM. The culprit in this case is the derivative appearing between the scalar fields in (5.3.16), which generates an overall minus sign between the positive and negative frequency field modes. This differs from the neutrino case presented in Section 5.2, where the asymmetry results from the anticommutation relations for fermionic operators. Finally, for completeness we note that the corresponding energy splittings for a real scalar DM background are found by setting $n_\phi(\phi) = n_\phi(\phi^*)$, such that (5.3.21) should vanish identically.

5.3.2 Spin-$\frac{1}{2}$

We now turn our attention to spin-$\frac{1}{2}$ dark matter, popular candidates for which include sterile neutrinos [232–234] (or more generally heavy neutral leptons), which may also explain short baseline anomalies [235], and neutralinos [45, 236], which naturally arise from supersymmetric models.

Label	$\mathcal{O}_{\rm DM}\mathcal{O}_{\rm SM}$	Background	$\langle\mathcal{H}_{\rm int}\rangle$
$\mathcal{O}_{\chi_1}$	$(\bar{\chi}\gamma_\mu\chi)(\bar{\psi}\gamma^\mu\gamma^5\psi)$	$\|\chi\rangle$	$4m_\psi(p_\chi\cdot S_\psi)$
		$\|\bar{\chi}\rangle$	$-4m_\psi(p_\chi\cdot S_\psi)$
$\mathcal{O}_{\chi_2}$	$(\bar{\chi}\gamma_\mu\gamma^5\chi)(\bar{\psi}\gamma^\mu\gamma^5\psi)$	$\|\chi\rangle$	$4m_\psi m_\chi h_\chi(S_\chi\cdot S_\psi)$
		$\|\bar{\chi}\rangle$	$4m_\psi m_\chi h_\chi(S_\chi\cdot S_\psi)$
$\mathcal{O}_{\chi_3}$	$(\bar{\chi}\sigma_{\mu\nu}\chi)(\bar{\psi}\sigma^{\mu\nu}\psi)$	$\|\chi\rangle$	$8h_\chi\big[(p_\chi\cdot S_\psi)(S_\chi\cdot p_\psi) - (p_\chi\cdot p_\psi)(S_\chi\cdot S_\psi)\big]$
		$\|\bar{\chi}\rangle$	$-8h_\chi\big[(p_\chi\cdot S_\psi)(S_\chi\cdot p_\psi) - (p_\chi\cdot p_\psi)(S_\chi\cdot S_\psi)\big]$
$\mathcal{O}_{\chi_4}$	$i(\bar{\chi}\sigma_{\mu\nu}\chi)(\bar{\psi}\sigma^{\mu\nu}\gamma^5\psi)$	$\|\chi\rangle$	$-8h_\chi\varepsilon_{\alpha\beta\mu\nu}p_\chi^\alpha p_\psi^\beta S_\chi^\mu S_\psi^\nu$
		$\|\bar{\chi}\rangle$	$8h_\chi\varepsilon_{\alpha\beta\mu\nu}p_\chi^\alpha p_\psi^\beta S_\chi^\mu S_\psi^\nu$

Table 5.1: Lorentz invariant, Hermitian, gauge invariant and irreducible spin-$\frac{1}{2}$ DM operators contributing to the DSE up to dimension-6, along with their corresponding expectation values in a background of Dirac fermions and antifermions, denoted by $|\chi\rangle$ and $|\bar{\chi}\rangle$ respectively. We leave the global factors of the coupling, new physics scale and SM fermion spin eigenvalue h_ψ implicit.

As we have already seen for neutrinos, the DSE for spin-$\frac{1}{2}$ backgrounds differs considerably to the effect for scalar DM, as it can additionally depend on the helicity composition of the background. Furthermore, as the product of four fermion field operators has mass dimension-6, there can be no derivative couplings for fermions at the order considered here. As such, we only need to consider Lorentz structures containing products of linearly independent gamma matrices (5.3.5) and Levi-Civita symbols, the latter of which, as we saw, can be treated as an additional gamma matrix structure, $\sigma^{\mu\nu}\gamma^5$. In all cases, the absence of derivative couplings, along with the anticommutators for fermionic operators, will necessarily lead to energy splittings that require a background asymmetry.

Considering a spin-$\frac{1}{2}$ DM candidate χ, we tabulate all irreducible operators contributing the DSE up to dimension-6, along with their corresponding expectation values, in Table 5.1. For each, we consider the case where the background consists of Dirac χ and anti-χ, which we denote by $|\chi\rangle$ and $|\bar{\chi}\rangle$, respectively. The corresponding

expectation values in Majorana χ backgrounds are found by summing those in $|\chi\rangle$ and $|\bar{\chi}\rangle$ backgrounds.

In addition to the operators shown in Table 5.1, we could also have considered operators of the form $i(\bar{\chi}\sigma_{\mu\nu}\gamma^5\chi)(\bar{\psi}\sigma^{\mu\nu}\psi)$ and $(\bar{\chi}\sigma_{\mu\nu}\gamma^5\chi)(\bar{\psi}\sigma^{\mu\nu}\gamma^5\psi)$. However, using the identity (5.3.8), we can show that these are equivalent respectively to $\mathcal{O}_{\chi_4}$ and $\mathcal{O}_{\chi_3}$ from Table 5.1.

We have already seen the operators $\mathcal{O}_{\chi_1}$ and $\mathcal{O}_{\chi_2}$ in our discussion of the νSE in Section 5.2, which gave rise to the neutrino-antineutrino and helicity asymmetry terms for neutrinos respectively. The third operator in Table 5.1, $\mathcal{O}_{\chi_3}$, with the corresponding interaction Lagrangian

$$\mathcal{L}_{\text{int}}^{\chi_3} = -\frac{g_{\psi\chi}}{\Lambda^2}(\bar{\chi}\sigma_{\mu\nu}\chi)(\bar{\psi}\sigma^{\mu\nu}\psi), \tag{5.3.22}$$

leads to an energy shift

$$\Delta E_\psi^{\chi_3}(\mathbf{0}, h_\psi) = \frac{2g_{\psi\chi}}{m_\psi\Lambda^2}h_\psi \sum_{h_\chi} h_\chi \left[\left\langle \frac{(p_\chi \cdot S_\psi)(S_\chi \cdot p_\psi)}{E_\chi}\right\rangle - \left\langle \frac{(p_\chi \cdot p_\psi)(S_\chi \cdot S_\psi)}{E_\chi}\right\rangle\right] \times \left(n_\chi(\chi_{h_\chi}) - n_\chi(\bar{\chi}_{h_\chi})\right), \tag{5.3.23}$$

which after computing the averages as shown in Appendix C yields

$$\Delta E_\psi^{\chi_3}(\mathbf{0}, h_\psi) = \frac{7g_{\psi\chi}}{4\Lambda^2}h_\psi \left(n_\chi(\chi_R) - n_\chi(\chi_L) - n_\chi(\bar{\chi}_L) + n_\chi(\bar{\chi}_R)\right) + O\left(\beta_\oplus^2, 1-\beta_r\right), \tag{5.3.24}$$

where $\beta_r = \beta_\oplus/\beta_c \simeq 1$ is the ratio of the relative frame velocity and galactic circular velocity, β_c. The resulting energy splitting between the SM fermion spin states has magnitude

$$\Delta E_\psi^{\chi_3} = \frac{7g_{\psi\chi}}{2\Lambda^2}h_\psi \left(n_\chi(\chi_R) - n_\chi(\chi_L) - n_\chi(\bar{\chi}_L) + n_\chi(\bar{\chi}_R)\right), \tag{5.3.25}$$

to leading order in small quantities, where the subscripts L and R denote the number densities of left and right helicity dark fermions χ, which satisfy $n_\chi(\chi_R) + n_\chi(\chi_L) = n_\chi(\chi)$ and $n_\chi(\bar{\chi}_L) + n_\chi(\bar{\chi}_R) = n_\chi(\bar{\chi})$ by definition. Remarkably, this energy shift is not suppressed by the velocity scale provided that $\beta_r \simeq 1$. Despite this, energy

shifts of the form (5.3.25) are exceedingly difficult to generate: while the helicity asymmetry requirement of (5.3.25) naively appears comparable to that of (5.2.18) for neutrinos, this is not the case. The first difference is seen when considering Majorana fermions, for which $n_\chi(\chi_R) = n_\chi(\bar{\chi}_L)$ and $n_\chi(\chi_L) = n_\chi(\bar{\chi}_R)$. This leads to (5.3.25) vanishing identically, when (5.2.18) becomes (5.2.19) which importantly is non-zero. The second difference is more subtle. A chiral theory such as the weak interaction will naturally lead to scenarios in which

$$n_\chi(\chi_R) \simeq n_\chi(\bar{\chi}_L) \neq n_\chi(\chi_L) \simeq n_\chi(\bar{\chi}_R), \tag{5.3.26}$$

in particular when the DM fermion is produced relativistically, such that its helicity and chirality coincide[4]. This helicity profile is sufficient to generate a DSE through the operator $\mathcal{O}_{\chi_2}$, but not $\mathcal{O}_{\chi_3}$, which requires a further fermion-antifermion asymmetry (*e.g.* through a chemical potential) to give a non-zero energy splitting. This significantly restricts the number of models that can generate a DSE through operators of the form $\mathcal{O}_{\chi_3}$. Finally, we note that as discussed in Appendix B of [220], background helicity asymmetries vanish for very cold DM as a consequence of the relative frame velocity. This is true irrespective of the DM spin, and so should be taken into account whenever an operator requires a non-zero helicity asymmetry to contribute to the DSE.

The final operator appearing in Table 5.1, $\mathcal{O}_{\chi_4}$, generates an energy shift scaling with

$$\Delta E_\psi^{\chi_4}(\mathbf{0}, s_\psi) \sim \varepsilon_{\alpha\beta\mu\nu} p_\chi^\alpha p_\psi^\beta S_\chi^\mu S_\psi^\nu = m_\psi \left[\boldsymbol{p}_\chi, \boldsymbol{S}_\chi, \boldsymbol{S}_\psi\right], \tag{5.3.27}$$

where, in the second inequality, we have used that the SM fermion is at rest in the lab frame in the setup considered, and $[\boldsymbol{a}, \boldsymbol{b}, \boldsymbol{c}] = \boldsymbol{a} \cdot (\boldsymbol{b} \times \boldsymbol{c})$ is the scalar triple product. Considering only helicity eigenstates (5.2.17) with $\boldsymbol{S}_\chi \parallel \boldsymbol{p}_\chi$, (5.3.27) vanishes identically. We note, however, that this operator may give rise to a non-zero

[4] As helicity is a good quantum number, it is conserved in time. The helicity profile of the DM background today should therefore be the same as at production in the absence of significant late time interactions. See [220] and [221] for the argument as applied to the CνB.

DSE for an alternative experimental setup where the SM fermion is not at rest in the lab frame.

5.3.3 Spin-1

Vector bosons remain popular in many models of DM, with candidates including additional U(1) gauge bosons [6, 237–240], superpartners to neutrinos [45, 236], and Kaluza-Klein states in theories with extra dimensions [45,241,242]. It is also possible to generate dark hadronic vector states in non-Abelian extensions to the SM [243].

The DSE for vector bosons is similar to that for scalar bosons, and may depend on either the total background DM density or require an asymmetry in the presence of derivative couplings. They differ, however, in the fact that vector bosons carry an additional Lorentz index, which expands the number of contributing operators. Here we consider a massive[5] vector field X^μ, with field decomposition

$$X_\mu(x) = \int \frac{\mathrm{d}^3\boldsymbol{p}}{(2\pi)^3}\frac{1}{\sqrt{2E_p}}\sum_l \left(a(\boldsymbol{p},l)\epsilon_\mu(p,l)e^{-ip\cdot x} + b^\dagger(\boldsymbol{p},l)\epsilon^*_\mu(p,l)e^{ip\cdot x}\right) , \quad (5.3.28a)$$

$$X^*_\mu(x) = \int \frac{\mathrm{d}^3\boldsymbol{p}}{(2\pi)^3}\frac{1}{\sqrt{2E_p}}\sum_l \left(a^\dagger(\boldsymbol{p},l)\epsilon^*_\mu(p,l)e^{ip\cdot x} + b(\boldsymbol{p},l)\epsilon_\mu(p,l)e^{-ip\cdot x}\right) , \quad (5.3.28b)$$

where the creation and annihilation operators satisfy the commutation relations (5.3.15), and $\epsilon^\mu(p,l) \equiv \epsilon^\mu_l$ is the polarisation vector with polarisation $l \in \{-1,0,1\}$. Considering the helicity eigenstates for a state with momentum along the positive z direction, these take the form

$$\epsilon^\mu(p,1) \equiv \epsilon^\mu_+ = \frac{1}{\sqrt{2}}(0,1,i,0) \quad (5.3.29a)$$

$$\epsilon^\mu(p,-1) \equiv \epsilon^\mu_- = \frac{1}{\sqrt{2}}(0,1,-i,0) \quad (5.3.29b)$$

$$\epsilon^\mu(p,0) \equiv \epsilon^\mu_L = \frac{1}{m_X}\left(|\boldsymbol{p}|,0,0,E_p\right) \quad (5.3.29c)$$

which we will refer to as the right, left and longitudinal polarisation states respectively, together satisfying $\epsilon_l \cdot \epsilon^*_{l'} = -\delta_{ll'}$. The polarisation vectors for momenta along

[5] In order to be cold, the dark matter background must be massive.

other directions are found by applying the appropriate rotation matrix. These will need to be considered in order to perform the averaging appropriately.

We tabulate all irreducible operators for vector DM contributing to the DSE up to dimension-6 in Table 5.2. As before, we consider each of the cases where the background consists of a complex vector field, X_μ and its conjugate, X^*_μ, which we denote by $|X\rangle$ and $|X^*\rangle$, respectively. The corresponding expectation values in real X backgrounds are found by summing those in $|X\rangle$ and $|X^*\rangle$ backgrounds.

The first operator in Table 5.2, $\mathcal{O}_{X_1}$, is analogous to the scalar DM operator appearing in (5.3.16). The DSE for this operator has been discussed in detail in Section 5.3.1; the only difference being the overall sign of the energy shift, generated by the contraction of two polarisation vectors. As a result, the energy splitting between the two SM fermion spin states will be the same for $\mathcal{O}_{X_1}$ as for its scalar counterpart, and sensitivity to the individual energy shifts is required to distinguish between the two operators.

The second operator in Table 5.2, $\mathcal{O}_{X_2}$, generates an energy shift

$$\Delta E_\psi^{X_2}(\mathbf{0}, h_\psi) = \frac{g_{\psi X}}{2m_\psi \Lambda} h_\psi \sum_{l_X} \left\langle \frac{1}{E_X} \mathrm{Im}\left[\varepsilon_{\alpha\beta\mu\nu} p_\psi^\alpha S_\psi^\beta \epsilon_{l_X}^{*\mu} \epsilon_{l_X}^{\nu}\right] \right\rangle \left(n_X(X_{l_X}) - n_X(X^*_{l_X})\right) , \tag{5.3.30}$$

for charged vector bosons, and zero otherwise. We immediately see that the longitudinal modes of X_μ with real polarisation vectors do not contribute to the DSE. This leaves the remaining two polarisation states, which after performing the averaging and taking the difference between the two energy shifts gives an SM fermion energy splitting

$$\Delta E_\psi^{X_2} = \frac{7 g_{\psi X}}{8 m_X \Lambda} \left(n_X(X_-) - n_X(X_+) - n_X(X^*_-) + n_X(X^*_+)\right) , \tag{5.3.31}$$

to leading order. Similarly to (5.3.25), the energy shift from $\mathcal{O}_{X_2}$ is not suppressed by the velocity scale, but requires both a polarisation and matter-antimatter asymmetry in order to give a non-zero contribution to the DSE. The former requirement is more difficult for vector bosons than fermions, which permit chiral Lagrangians that

Label	$\mathcal{O}_{\rm DM}\mathcal{O}_{\rm SM}$	Background	$\langle\mathcal{H}_{\rm int}\rangle$
$\mathcal{O}_{X_1}$	$i(X^*_\alpha \overset{\leftrightarrow}{\partial_\mu} X^\alpha)(\bar\psi\gamma^\mu\gamma^5\psi)$	$\lvert X\rangle$	$4m_\psi(\boldsymbol{p}_X\cdot\boldsymbol{S}_\psi)$
		$\lvert X^*\rangle$	$-4m_\psi(\boldsymbol{p}_X\cdot\boldsymbol{S}_\psi)$
$\mathcal{O}_{X_2}$	$iX^*_\mu X_\nu(\bar\psi\sigma^{\mu\nu}\psi)$	$\lvert X\rangle$	$2\,\mathrm{Im}\left[\varepsilon_{\alpha\beta\mu\nu}\epsilon^{*\alpha}_{l_X}\epsilon^{\beta}_{l_X}p^\mu_\psi S^\nu_\psi\right]$
		$\lvert X^*\rangle$	$-2\,\mathrm{Im}\left[\varepsilon_{\alpha\beta\mu\nu}\epsilon^{*\alpha}_{l_X}\epsilon^{\beta}_{l_X}p^\mu_\psi S^\nu_\psi\right]$
$\mathcal{O}_{X_3}$	$X^*_\mu X_\nu(\bar\psi\sigma^{\mu\nu}\gamma^5\psi)$	$\lvert X\rangle$	$4\,\mathrm{Im}\left[(\epsilon^*_{l_X}\cdot S_\psi)(\epsilon_{l_X}\cdot p_\psi)\right]$
		$\lvert X^*\rangle$	$-4\,\mathrm{Im}\left[(\epsilon^*_{l_X}\cdot S_\psi)(\epsilon_{l_X}\cdot p_\psi)\right]$
$\mathcal{O}_{X_4}$	$i\left[X^{\mu*}(\partial_\mu X_\nu)-(\partial_\mu X^*_\nu)X^\mu\right]\times(\bar\psi\gamma^\nu\gamma^5\psi)$	$\lvert X\rangle$	$-4m_\psi\mathrm{Re}\left[(\epsilon^*_{l_X}\cdot S_\psi)(\boldsymbol{\epsilon}_{l_X}\cdot\boldsymbol{p}_X)\right]$
		$\lvert X^*\rangle$	$4m_\psi\mathrm{Re}\left[(\epsilon^*_{l_X}\cdot S_\psi)(\boldsymbol{\epsilon}_{l_X}\cdot\boldsymbol{p}_X)\right]$
$\mathcal{O}_{X_5}$	$\left[X^{\mu*}(\partial_\mu X_\nu)+(\partial_\mu X^*_\nu)X^\mu\right]\times(\bar\psi\gamma^\nu\gamma^5\psi)$	$\lvert X\rangle$	$4m_\psi\mathrm{Im}\left[(\epsilon^*_{l_X}\cdot S_\psi)(\boldsymbol{\epsilon}_{l_X}\cdot\boldsymbol{p}_X)\right]$
		$\lvert X^*\rangle$	$4m_\psi\mathrm{Im}\left[(\epsilon^*_{l_X}\cdot S_\psi)(\boldsymbol{\epsilon}_{l_X}\cdot\boldsymbol{p}_X)\right]$
$\mathcal{O}_{X_6}$	$i(X^{*\mu}X_\nu+X^\mu X^*_\nu)\times(\bar\psi\overset{\leftrightarrow}{\partial_\mu}\gamma^\nu\gamma^5\psi)$	$\lvert X\rangle$	$-8m_\psi\mathrm{Re}\left[(\epsilon^*_{l_X}\cdot S_\psi)(\boldsymbol{\epsilon}_{l_X}\cdot\boldsymbol{p}_\psi)\right]$
		$\lvert X^*\rangle$	$-8m_\psi\mathrm{Re}\left[(\epsilon^*_{l_X}\cdot S_\psi)(\boldsymbol{\epsilon}_{l_X}\cdot\boldsymbol{p}_\psi)\right]$
$\mathcal{O}_{X_7}$	$i\varepsilon^{\alpha\beta\mu\nu}\left[X^*_\alpha(\partial_\beta X_\mu)-(\partial_\beta X^*_\mu)X_\alpha\right]\times(\bar\psi\gamma_\nu\gamma^5\psi)$	$\lvert X\rangle$	0
		$\lvert X^*\rangle$	0
$\mathcal{O}_{X_8}$	$\varepsilon^{\alpha\beta\mu\nu}\left[X^*_\alpha(\partial_\beta X_\mu)+(\partial_\beta X^*_\mu)X_\alpha\right]\times(\bar\psi\gamma_\nu\gamma^5\psi)$	$\lvert X\rangle$	$4m_\psi\mathrm{Im}\left[\varepsilon_{\alpha\beta i\nu}\epsilon^{*\alpha}_{l_X}\epsilon^{\beta}_{l_X}\boldsymbol{p}^i_X S^\nu_\psi\right]$
		$\lvert X^*\rangle$	$4m_\psi\mathrm{Im}\left[\varepsilon_{\alpha\beta i\nu}\epsilon^{*\alpha}_{l_X}\epsilon^{\beta}_{l_X}\boldsymbol{p}^i_X S^\nu_\psi\right]$

Table 5.2: Lorentz invariant, Hermitian, gauge invariant and irreducible spin-1 DM operators contributing to the DSE up to dimension-6, along with their corresponding expectation values in a background of complex vector bosons and the conjugate field, denoted by $|X\rangle$ and $|X^*\rangle$, respectively. We leave the global factors of the coupling, new physics scale and SM fermion spin eigenvalue h_ψ implicit.

preferentially produce fermions of a single helicity at high energies. For vector DM, a polarisation asymmetry must therefore be generated through another mechanism such as scattering on a polarised fermionic background.

The third operator in Table 5.2 gives rise to an energy shift

$$\Delta E_\psi^{X_3}(\mathbf{0}, s_\psi) \sim \left\langle \frac{1}{E_X} \mathrm{Im}\left[(p_\psi \cdot \epsilon_{l_X})(S_\psi \cdot \epsilon_{l_X}^*)\right] \right\rangle , \tag{5.3.32}$$

which vanishes for an SM fermion at rest in the lab frame. We note, however, that there may be a contribution to the energy shift from the right and left polarisation states for other experimental setups. On the other hand, the longitudinal state cannot contribute for any setup as its polarisation vector is real.

The fourth operator in Table 5.2 is unique, and leads to an energy splitting

$$\begin{aligned} \Delta E_\psi^{X_4} &= \frac{2g_{\psi X}}{\Lambda^2} \sum_{l_X} \left\langle \frac{1}{E_X} \mathrm{Re}\left[(\epsilon_{l_X}^* \cdot S_\psi)(\boldsymbol{\epsilon}_{l_X} \cdot \boldsymbol{p}_X)\right] \right\rangle \left(n_X(X_{l_X}) - n_X(X_{l_X}^*)\right) \\ &= -\frac{4g_{\psi X}}{\Lambda^2} \beta_\oplus \left(n_X(X_L) - n_X(X_L^*)\right) , \end{aligned} \tag{5.3.33}$$

which depends solely on the density of longitudinally polarised background states. This energy splitting is most closely related to the one generated by $\mathcal{O}_{X_1}$, which instead depends on the total asymmetry between X_μ and its conjugate. As such, it must always be the case that $\Delta E_\psi^{X_1} \geq \Delta E_\psi^{X_4}$, which may serve to distinguish the two.

Of the remaining operators, all have vanishing contributions to the Stodolsky effect for the experimental setup considered: the contribution from $\mathcal{O}_{X_5}$ is proportional to the imaginary part of the kinematic structure found in (5.3.33), which is real valued after averaging over background momenta; the contribution from $\mathcal{O}_{X_6}$ is proportional to $\boldsymbol{p}_\psi$, which is zero for this setup; the contribution due to $\mathcal{O}_{X_7}$ vanishes at the kinematic level as

$$\left\langle \mathcal{H}_{\mathrm{int}}^{X_7} \right\rangle \sim \varepsilon_{\alpha\beta\mu\nu} \mathrm{Re}\left[\epsilon_{l_X}^{*\alpha} \epsilon_{l_X}^{\beta}\right] = 0 ; \tag{5.3.34}$$

while the energy splitting due to $\mathcal{O}_{X_8}$ scales with

$$\left\langle \mathcal{H}_{\rm int}^{X_8} \right\rangle \sim \varepsilon_{\alpha\beta i\nu} \epsilon_{l_X}^{*\alpha} \epsilon_{l_X}^{\beta} \boldsymbol{p}_X^i S_\psi^\nu \,, \tag{5.3.35}$$

which is zero for the longitudinal states since $\epsilon_L^* = \epsilon_L$, and for the right and left helicity states as only their spatial components are non-zero.

Notice that the operator giving rise to the Zeeman effect, $\mathcal{O}_F \sim F_{\mu\nu}\bar{\psi}\sigma^{\mu\nu}\psi$, where $F_{\mu\nu}$ is the field strength tensor, does not appear in Table 5.2. This is because it only contains a single copy of the vector field, and as a result has a zero expectation value for incoherent background DM states (5.2.3). Instead, the Zeeman effect occurs in a coherent background, defined as the minimum uncertainty state and by extension the state which is the closest to a classical background. Importantly, bosonic field operators have non-zero expectation values in coherent backgrounds. Such coherent states can be formed by any boson, leading to SM fermion spin-dependent energy shifts that are generated by lower dimension operators than those for incoherent states. It is possible, therefore, that the energy shifts arising from coherent states are significantly larger than those considered here. It is also worth noting that none of the operators in Table 5.2 describe U(1) gauge bosons, but that the wider class of operators generating energy splittings for coherent backgrounds can. The operator $\mathcal{O}_F$ is such an example.

5.3.4 Spin-$\frac{3}{2}$

The last class of particle we look at are spin-$\frac{3}{2}$ fermions, which satisfy both Dirac and spin-1 equations of motion,

$$\left(i\partial\!\!\!/ - m\right)\Psi_\mu = 0\,, \qquad \partial^\mu \Psi_\mu = 0\,, \tag{5.3.36}$$

together with the constraint $\not{\Psi} = \gamma^\mu \Psi_\mu = 0$. Combining these equations and the Chisholm identity (5.3.7), one can show that these fermions are solutions to the

Rarita-Schwinger (RS) Lagrangian which can be written as [244],

$$\mathcal{L}_{\rm RS} = -\frac{1}{2}\bar{\Psi}_\mu \left(\varepsilon^{\mu\alpha\beta\nu}\gamma^5\gamma_\alpha\partial_\beta - im\sigma^{\mu\nu}\right)\Psi_\nu\,, \tag{5.3.37}$$

and we will refer to the solutions Ψ_μ to this equation as *RS fermions*. There is however a caveat to this definition: it can be shown that the general massive solution to the RS Lagrangian in fact consists of a superposition of a spin-$\frac{3}{2}$ and two spin-$\frac{1}{2}$ states [245, 246][6]. In other words, Ψ_μ is not a pure spin-$\frac{3}{2}$ state. This problem can however be alleviated by only considering the helicity $\lambda = \pm\frac{3}{2}$ modes of an RS fermion, which is equivalent to selecting the spin-$\frac{3}{2}$ components [247]. Bearing this in mind, we nevertheless choose to consider the general solution Ψ_μ in this section, as the helicity $\lambda = \pm\frac{3}{2}$ and $\lambda = \pm\frac{1}{2}$ states of the gravitino are present alongside each other in most scenari [248–250].

Spin-$\frac{3}{2}$ particles are less popular candidates for DM, partly due to the fact that there are no known spin-$\frac{3}{2}$ fermions in renormalisable theories [228]. Despite this, spin-$\frac{3}{2}$ DM has been shown capable of reproducing the observed relic density [251], and can be produced as the gravitino in supergravity [45], or as bound states in non-Abelian extensions to the SM. In particular, spin-$\frac{3}{2}$ baryons are the lightest states of a dark SU(3) with a single quark flavour [243, 252].

Despite sharing many properties with pure spin-$\frac{1}{2}$ fermions, the additional spin d.o.f. carried by RS fermions give rise to operators with richer Lorentz structures. This is turn leads a larger number of operators that generate a DSE, the energy shift from which will depend on up to four helicity states. As we will see, the contribution to the energy shift from each helicity state will differ in both sign and magnitude for RS fermions, which may serve as an additional tool to help distinguish them from pure spin-$\frac{1}{2}$ fermions.

For this section, we consider an RS fermion Ψ_μ with field decomposition [247]

$$\Psi_\mu(x) = \int \frac{\mathrm{d}^3\boldsymbol{p}}{(2\pi)^3}\frac{1}{\sqrt{2E_p}}\sum_\lambda \left(a(\boldsymbol{p},\lambda)\xi^+_\mu(p,\lambda)e^{-ip\cdot x} + b^\dagger(\boldsymbol{p},\lambda)\xi^-_\mu(p,\lambda)e^{ip\cdot x}\right)\,, \tag{5.3.38}$$

[6]The spin-$\frac{1}{2}$ states do not satisfy the constraint $\not{\Psi} = 0$.

$$\bar{\Psi}_\mu(x) = \int \frac{\mathrm{d}^3\boldsymbol{p}}{(2\pi)^3}\frac{1}{\sqrt{2E_p}}\sum_\lambda \left(a^\dagger(\boldsymbol{p},\lambda)\bar{\xi}^+_\mu(p,\lambda)e^{ip\cdot x} + b(\boldsymbol{p},\lambda)\bar{\xi}^-_\mu(p,\lambda)e^{-ip\cdot x}\right) , \quad (5.3.39)$$

where $\lambda \in \{\frac{3}{2}, \frac{1}{2}, -\frac{1}{2}, -\frac{3}{2}\}$ is the helicity of the RS fermion, a and b are annihilation operators obeying the anticommutation relations (5.2.6), and again we set $a = b$ for Majorana fermions, while we define the "polarisation spinors" $\xi^\pm_\mu$ via

$$\xi^+_\mu(p,\lambda) = \sum_{l,h} C^\lambda_{l,h}\epsilon_\mu(p,l)u(p,h)\,, \quad (5.3.40a)$$

$$\xi^-_\mu(p,\lambda) = \sum_{l,h} C^\lambda_{l,h}\epsilon^*_\mu(p,l)v(p,h)\,, \quad (5.3.40b)$$

with the sum running over the values of $l \in \{-1, 0, 1\}$ and $h = \pm 1$ for which $l + \frac{h}{2} = \lambda$. Finally, the Clebsch-Gordan coefficients for an RS field can be found in [6] and read

$$\lambda = +\frac{3}{2}: \qquad C^{\frac{3}{2}}_{1,1} = 1\,, \quad (5.3.41a)$$

$$\lambda = +\frac{1}{2}: \qquad C^{\frac{1}{2}}_{1,-1} = \sqrt{\frac{1}{3}}\,,\ C^{\frac{1}{2}}_{0,1} = \sqrt{\frac{2}{3}}\,, \quad (5.3.41b)$$

$$\lambda = -\frac{1}{2}: \qquad C^{-\frac{1}{2}}_{-1,1} = \sqrt{\frac{1}{3}}\,,\ C^{-\frac{1}{2}}_{0,-1} = \sqrt{\frac{2}{3}}\,, \quad (5.3.41c)$$

$$\lambda = -\frac{3}{2}: \qquad C^{-\frac{3}{2}}_{-1,-1} = 1\,, \quad (5.3.41d)$$

with all other coefficients equal to zero.

Once more, we tabulate all irreducible operators for RS fermion DM contributing to the DSE up to dimension-6 in Table 5.3. As before, we consider backgrounds of RS fermions Ψ_μ and anti-RS fermions, $\bar{\Psi}_\mu$, which we denote by $|\Psi\rangle$ and $|\bar{\Psi}\rangle$, respectively. The corresponding expectation values in backgrounds of RS fermions that satisfy the Majorana condition are found by summing those in $|\Psi\rangle$ and $|\bar{\Psi}\rangle$ backgrounds. We additionally introduce the shorthand sum

$$\sum_C \equiv \sum_{l_\Psi, h_\Psi} \left(C^{\lambda_\Psi}_{l_\Psi,h_\Psi}\right)^2 . \quad (5.3.42)$$

We note that the argument used to exclude the operators $\mathcal{O}_{\chi_5}$ and $\mathcal{O}_{\chi_6}$ in Section 5.3.2 applies here to the equivalent operators with RS fields.

Label	$\mathcal{O}_{\rm DM}\mathcal{O}_{\rm SM}$	Background	$\langle\mathcal{H}_{\rm int}\rangle$
$\mathcal{O}_{\Psi_1}$	$(\bar{\Psi}_\alpha\gamma_\mu\Psi^\alpha)(\bar{\psi}\gamma^\mu\gamma^5\psi)$	$\lvert\Psi\rangle$	$-4m_\psi(p_\Psi\cdot S_\psi)$
		$\lvert\bar{\Psi}\rangle$	$4m_\psi(p_\Psi\cdot S_\psi)$
$\mathcal{O}_{\Psi_2}$	$(\bar{\Psi}_\alpha\gamma_\mu\gamma^5\Psi^\alpha)(\bar{\psi}\gamma^\mu\gamma^5\psi)$	$\lvert\Psi\rangle$	$-4m_\psi m_\Psi\sum_C h_\Psi(S_\Psi\cdot S_\psi)$
		$\lvert\bar{\Psi}\rangle$	$-4m_\psi m_\Psi\sum_C h_\Psi(S_\Psi\cdot S_\psi)$
$\mathcal{O}_{\Psi_3}$	$i(\bar{\Psi}_\mu\Psi_\nu)(\bar{\psi}\sigma^{\mu\nu}\psi)$	$\lvert\Psi\rangle$	$4m_\Psi\sum_C \mathrm{Im}\left[\varepsilon_{\alpha\beta\mu\nu}p_\psi^\alpha S_\psi^\beta\epsilon_{l_\Psi}^{*\mu}\epsilon_{l_\Psi}^\nu\right]$
		$\lvert\bar{\Psi}\rangle$	$-4m_\Psi\sum_C \mathrm{Im}\left[\varepsilon_{\alpha\beta\mu\nu}p_\psi^\alpha S_\psi^\beta\epsilon_{l_\Psi}^{*\mu}\epsilon_{l_\Psi}^\nu\right]$
$\mathcal{O}_{\Psi_4}$	$(\bar{\Psi}_\alpha\sigma_{\mu\nu}\Psi^\alpha)(\bar{\psi}\sigma^{\mu\nu}\psi)$	$\lvert\Psi\rangle$	$-8\sum_C h_\Psi\Big[(p_\Psi\cdot S_\psi)(S_\Psi\cdot p_\psi) - (p_\Psi\cdot p_\psi)(S_\Psi\cdot S_\psi)\Big]$
		$\lvert\bar{\Psi}\rangle$	$8\sum_C h_\Psi\Big[(p_\Psi\cdot S_\psi)(S_\Psi\cdot p_\psi) - (p_\Psi\cdot p_\psi)(S_\Psi\cdot S_\psi)\Big]$
$\mathcal{O}_{\Psi_5}$	$(\bar{\Psi}_\mu\Psi_\nu)(\bar{\psi}\sigma^{\mu\nu}\gamma^5\psi)$	$\lvert\Psi\rangle$	$8m_\Psi\sum_C \mathrm{Im}\left[(S_\psi\cdot\epsilon_{l_\Psi}^*)(p_\psi\cdot\epsilon_{l_\Psi})\right]$
		$\lvert\bar{\Psi}\rangle$	$-8m_\Psi\sum_C \mathrm{Im}\left[(S_\psi\cdot\epsilon_{l_\Psi}^*)(p_\psi\cdot\epsilon_{l_\Psi})\right]$
$\mathcal{O}_{\Psi_6}$	$i(\bar{\Psi}_\alpha\sigma_{\mu\nu}\Psi^\alpha)(\bar{\psi}\sigma^{\mu\nu}\gamma^5\psi)$	$\lvert\Psi\rangle$	$8\sum_C h_\Psi\varepsilon_{\alpha\beta\mu\nu}p_\Psi^\alpha p_\psi^\beta S_\Psi^\mu S_\psi^\nu$
		$\lvert\bar{\Psi}\rangle$	$-8\sum_C h_\Psi\varepsilon_{\alpha\beta\mu\nu}p_\Psi^\alpha p_\psi^\beta S_\Psi^\mu S_\psi^\nu$

Table 5.3: Lorentz invariant, Hermitian, gauge invariant and irreducible RS DM operators contributing to the DSE up to dimension-6, along with their corresponding expectation values in a background of RS and anti-RS fermions, denoted by $|\Psi\rangle$ and $|\bar{\Psi}\rangle$, respectively. We leave the global factors of the coupling, new physics scale and SM fermion spin eigenvalue, h_ψ, implicit.

The first operator, $\mathcal{O}_{\Psi_1}$, gives the same energy shift as the similar spin-$\frac{1}{2}$ operator $\mathcal{O}_{\chi_1}$ up to an overall sign, which results from the contraction of two polarisation vectors. It therefore only requires a matter-antimatter asymmetry in order to generate a DSE, but cannot tell us anything about the helicity structure of the background. This naturally makes it difficult to distinguish from $\mathcal{O}_{\chi_1}$.

The remaining operators are far more interesting. Consider $\mathcal{O}_{\Psi_2}$, which gives rise to an energy shift

$$\begin{aligned}\Delta E_\psi^{\Psi_2}(\mathbf{0}, h_\psi) &= -\frac{g_{\psi\Psi}}{\Lambda^2} m_\Psi h_\psi \sum_{\lambda_\Psi} \sum_C h_\Psi \left\langle \frac{1}{E_\Psi}(S_\Psi \cdot S_\psi) \right\rangle \Big(n_\Psi(\Psi_{\lambda_\Psi}) + n_\Psi(\bar{\Psi}_{\lambda_\Psi}) \Big) \\ &= \frac{7 g_{\psi\Psi}}{8\Lambda^2} h_\psi \Big[\Big(n_\Psi(\Psi_{++}) + n_\Psi(\bar{\Psi}_{++}) - n_\Psi(\Psi_{--}) - n_\Psi(\bar{\Psi}_{--}) \Big) \\ &\quad + \frac{1}{3} \Big(n_\Psi(\Psi_{+-}) + n_\Psi(\bar{\Psi}_{+-}) - n_\Psi(\Psi_{-+}) - n_\Psi(\bar{\Psi}_{-+}) \Big) \Big], \end{aligned} \tag{5.3.43}$$

where the subscripts $\pm\pm$ and $\pm\mp$ refer to the $\pm\frac{3}{2}$ and $\pm\frac{1}{2}$ helicity states respectively. Taking the difference between the energy shifts for each spin state gives the energy splitting due to $\mathcal{O}_{\Psi_2}$

$$\begin{aligned}\Delta E_\psi^{\Psi_2} = \frac{7 g_{\psi\Psi}}{4\Lambda^2} \Big[& \Big(n_\Psi(\Psi_{++}) + n_\Psi(\bar{\Psi}_{++}) - n_\Psi(\Psi_{--}) - n_\Psi(\bar{\Psi}_{--}) \Big) \\ & + \frac{1}{3} \Big(n_\Psi(\Psi_{+-}) + n_\Psi(\bar{\Psi}_{+-}) - n_\Psi(\Psi_{-+}) - n_\Psi(\bar{\Psi}_{-+}) \Big) \Big], \end{aligned} \tag{5.3.44}$$

which requires a non-zero helicity asymmetry in order to generate a DSE, akin to $\mathcal{O}_{\chi_2}$. This is easily achieved in a chiral theory similar to the weak interaction. Owing to the Clebsch-Gordan coefficients, however, the contribution to the DSE from the $\pm\frac{1}{2}$ helicity states is suppressed by a factor of three, which for the same total DM density then leads to a reduced energy shift. As such, if the mass, and by extension the number density of the DM is known, the reduced energy splitting could serve as a tool to distinguish between spin-$\frac{1}{2}$ and spin-$\frac{3}{2}$ DM backgrounds. Although difficult to observe, we also note that the energy shifts of the individual spin states differ by an overall sign between $\mathcal{O}_{\Psi_2}$ and $\mathcal{O}_{\chi_2}$. The operator $\mathcal{O}_{\Psi_3}$ yields a similarly suppressed energy splitting

$$\Delta E_{\psi}^{\Psi_3} = \frac{7 g_{\psi\Psi}}{4\Lambda^2}\Big[\Big(n_\Psi(\Psi_{++}) - n_\Psi(\bar{\Psi}_{++}) - n_\Psi(\Psi_{--}) + n_\Psi(\bar{\Psi}_{--})\Big) + \frac{1}{3}\Big(n_\Psi(\Psi_{+-}) - n_\Psi(\bar{\Psi}_{+-}) - n_\Psi(\Psi_{-+}) + n_\Psi(\bar{\Psi}_{-+})\Big)\Big], \quad (5.3.45)$$

which is only non-zero in a background with both a fermion-antifermion and helicity asymmetry. In this case, we note the analogous lower spin operator is in fact bosonic, $\mathcal{O}_{X_2}$, which should result in a slightly larger splitting for the same background density. However, the biggest difference is in the generation of (5.3.31) and (5.3.45); as previously discussed, a helicity asymmetry cannot arise at the Lagrangian level for bosons, but are possible in chiral theories of fermions which, if relativistic at production, prefer a given helicity. Consequently, it is much easier to generate the DSE from $\mathcal{O}_{\Psi_3}$. The remaining three operators, $\mathcal{O}_{\Psi_4}$, $\mathcal{O}_{\Psi_5}$ and $\mathcal{O}_{\Psi_6}$ are analogous to $\mathcal{O}_{\chi_3}$, $\mathcal{O}_{X_3}$ and $\mathcal{O}_{\chi_4}$, respectively, such that only the first contributes a DSE for the experimental setup considered here. In the same way as (5.3.44), the energy shifts due to $\mathcal{O}_{\Psi_4}$ differ from their analogues by an overall sign and a small suppression factor from the Clebsch-Gordan coefficients. Finally, we have omitted the pseudoscalar analogues of $\mathcal{O}_{\Psi_3}$ and $\mathcal{O}_{\Psi_5}$, proportional to $\Psi_\mu \gamma^5 \Psi_\nu$, from Table 5.3 as the expectation values of their Hamiltonians vanish trivially using (5.3.6).

The discussion here is easily extended to higher spin states, which we naively expect will differ only in the overall sign and magnitude of their DSEs. In particular, the magnitude of the DSE for most operators should decrease with increasing spin, as progressively smaller Clebsch-Gordan coefficients will suppress the contribution from the intermediate helicity states.

5.4 Experimental Feasibility

Observing the tiny energy splittings induced by the DSE directly is a remarkable challenge due to their small magnitude. Take for example the splitting due to the

CνB, whose magnitude is expected to be of order

$$|\Delta E_\psi| \sim G_F \beta_\oplus n_{\nu,0} \approx 5 \times 10^{-39}\,\mathrm{eV}\,, \tag{5.4.1}$$

assuming maximal neutrino-antineutrino asymmetry, where we have used $\beta_\oplus \simeq 10^{-3}$ and $n_{\nu,0} = 56\,\mathrm{cm}^{-3}$ is the predicted relic neutrino density per degree of freedom. This is approximately thirty orders of magnitude smaller than the energy splitting due to the Zeeman effect in a 1 G magnetic field. Clearly then, this effect is nigh impossible to observe on the scale of a single target. To that end, we identify two methods utilising macroscopic targets through which the DSE may be observed. Both of these rely on the same property; as a result of the energy splitting due to the DM background, the SM fermion Hamiltonian H_ψ and spin operators orthogonal to the DM wind $S_\perp$ no longer commute, leading to a spin precession

$$\frac{\mathrm{d}S_\perp}{\mathrm{d}t} = i\left[H_\psi, S_\perp\right] \sim O(\Delta E_\psi)\,, \tag{5.4.2}$$

which can equivalently be interpreted as a torque. A ferromagnet with polarisation transverse to the DM wind will therefore experience a macroscopic acceleration as a result of the spin precession, which can be observed with a Cavendish-style torsion balance. Alternatively, a target initially polarised along an external magnetic field will develop some transverse magnetisation as a consequence of the DM background, which may measurable with a Superconducting Quantum Interference Device (SQUID) magnetometer. We will explore each of these methods in turn.

5.4.1 Torsion Balance

The possibility of using a torsion balance to observe the tiny energy splittings due to the CνB was first identified by Leo Stodolsky in [219] and has since been discussed in several works [220,225,226]. A single SM fermion interacting with the DM background will experience a torque $\tau_\psi \approx |\Delta E_\psi|$, such that a macroscopic target

consisting of N_ψ fermions with degree of polarisation P will experience a total torque

$$\tau_{\rm tot} \approx P N_\psi |\Delta E_\psi| = \frac{N_A}{m_A}\frac{P}{A} M \times \begin{cases} Z|\Delta E_e|\,, & \psi = e\,, \\ |\Delta E_N|\,, & \psi = N\,, \end{cases} \tag{5.4.3}$$

where N denotes an atomic nucleus, N_A is the Avogadro number, while M, A and Z denote the total mass, the mass number and atomic number of the target, respectively. We have additionally introduced the "Avogadro mass" $m_A = 1\,\mathrm{g/mol}$ as a conversion factor. To estimate the sensitivity of a torsion balance to this energy splitting, we consider the same setup as [220] using a torsion balance consisting of N_m spherical, uniformly dense ferromagnets a distance R away from some central axis. To maximise the sensitivity, we additionally assume that opposing ferromagnets are polarised antiparallel to one another. For this setup, the torsion balance will experience a linear acceleration

$$a \approx \frac{N_A}{m_A}\frac{P}{A}\frac{N_m}{R} \times \begin{cases} Z|\Delta E_e|\,, & \psi = e\,, \\ |\Delta E_N|\,, & \psi = N\,. \end{cases} \tag{5.4.4}$$

As such, if accelerations as small as a_0 can be measured, the experiment is sensitive to energy splittings

$$\begin{aligned} |\Delta E_\psi| &\gtrsim a_0 \frac{m_A}{N_A}\frac{A}{P}\frac{R}{N_m} \times \begin{cases} \frac{1}{Z}\,, & \psi = e\,, \\ 1\,, & \psi = N\,, \end{cases} \\ &= 5.8\times 10^{-28}\,\mathrm{eV}\left(\frac{a_0}{10^{-15}\,\mathrm{cm\,s^{-2}}}\right)\left(\frac{R}{1\,\mathrm{cm}}\right)\frac{2}{N_m}\frac{A}{P} \times \begin{cases} \frac{1}{Z}\,, & \psi = e\,, \\ 1\,, & \psi = N\,, \end{cases} \end{aligned} \tag{5.4.5}$$

where for our reference sensitivity we have used $a_0 = 10^{-15}\,\mathrm{cm\,s^{-2}}$, which has recently been achieved in torsion balance tests of the weak equivalence principle [253]. We highlight that this value has been achieved using an unpolarised target to eliminate strong errors due to induced magnetic fields. For polarised targets, [254] sets a reference acceleration $a_0 \approx 10^{-6}\,\mathrm{cm\,s^{-2}}$ comparing polarised and unpolarised targets, while [255] constrains preferred-frame interactions to $10^{-21}\,\mathrm{eV}$. By com-

parison with (5.4.1), we see that this torsion balance experiment is insensitive to the CνB, but may still be able to observe DM for which the background number density $n_{\rm DM} \gg n_{\nu,0}$. In particular, as the background DM number density scales as $n_{\rm DM} = \rho_{\rm DM}/m_{\rm DM}$, where $\rho_{\rm DM} \approx 0.4\,\text{GeV}\,\text{cm}^{-3}$ is the local dark matter energy density [256], low mass DM scenarios are ideal candidates for detection using this method. Finally, we note that a torsion balance consisting test masses suspended by superconducting magnets has been considered in [257], which has an estimated sensitivity to accelerations as small as $a_0 \approx 10^{-23}\,\text{cm}\,\text{s}^{-2}$. This, in turn, would allow us to probe energy splittings of the order $10^{-36}\,\text{eV}$.

5.4.2 SQUID Magnetometer

The DM wind resulting from the relative motion of the Earth through the background acts similarly to a magnetic field, leading to the spin precession (5.4.2). As such, if the target spins are initially aligned along some fixed external magnetic field $\boldsymbol{B}_{\rm ext}$ that is not collinear with the DM wind, the presence of the background will cause the spins to shift away from the axis of $\boldsymbol{B}_{\rm ext}$ and give rise to a small transverse magnetisation. The spins will then precess around the combined magnetic field and DM wind with some characteristic frequency, which can be detected using a highly sensitive SQUID magnetometer. This idea has previously been discussed in the context of axion DM in [258], and is the basis of the CASPEr experiment [259].

Following the calculations in Appendix D, we find that the transverse magnetisation of a target consisting of N_ψ spins evolves as

$$|M_\perp(t)| = \frac{2\rho N_A}{m_A}\frac{P}{A}\frac{\left|R\sin\left(\frac{\omega_{\psi,0}}{2}t\right)\right|}{1+R^2}\sqrt{1+R^2\cos^2\left(\frac{\omega_{\psi,0}}{2}t\right)} \times \begin{cases} Z\mu_e\,, & \psi = e\,, \\ \mu_N\,, & \psi = N\,, \end{cases} \tag{5.4.6}$$

where ρ is the mass density of the target, μ_ψ denotes the magnetic moment of species ψ, $R = \Delta E_\psi/\Delta E_B$ is the ratio of the DM and Zeeman energy splittings, and $\omega_{\psi,0} = \Delta E_B\sqrt{1+R^2}$. In (5.4.6) we have assumed that the DM wind is exactly

perpendicular to $\boldsymbol{B}_{\rm ext}$, which maximises the transverse magnetisation, and that both the external magnetic field and DM wind directions are constant in time[7]. We give the full expression for $|M_\perp(t)|$ and discuss the time dependence in Appendix D.

The transverse magnetisation has a maximum of

$$|M_\perp(t_{\rm max})| = \frac{2\rho N_A}{m_A}\frac{P}{A}\frac{|R|}{1+R^2} \times \begin{cases} Z\mu_e\,, & \psi = e\,, \\ \mu_N\,, & \psi = N\,, \end{cases} \tag{5.4.7}$$

for $R \leq 1$, at $t_{\rm max} = (2k+1)\pi/\omega_{\psi,0}$ with $k \in \mathbb{N}^0$. Supposing that a magnetometer can precisely measure transverse magnetic fields with magnitude B_0, we will have sensitivity to energy splittings with magnitude

$$\begin{aligned} |\Delta E_\psi| &\gtrsim B_0|\boldsymbol{B}_{\rm ext}|\frac{m_A}{\rho N_A}\frac{A}{P} \times \begin{cases} \frac{1}{Z}\,, & \psi = e\,, \\ 1\,, & \psi = N\,, \end{cases} \\ &= 1.0\times 10^{-32}\,{\rm eV}\left(\frac{B_0}{10^{-16}\,{\rm T}}\right)\left(\frac{|\boldsymbol{B}_{\rm ext}|}{10^{-10}\,{\rm T}}\right)\left(\frac{7.9\,{\rm g\,cm^{-3}}}{\rho}\right)\frac{A}{P} \times \begin{cases} \frac{1}{Z}\,, & \psi = e\,, \\ 1\,, & \psi = N\,, \end{cases} \end{aligned} \tag{5.4.8}$$

for $R \ll 1$, where we have used $\Delta E_B = 2\mu_\psi|\boldsymbol{B}_{\rm ext}|$. For our reference scenario we have chosen $B_0 = 10^{-16}\,{\rm T}$, corresponding to the SQUID magnetometer discussed in [260], and used the density of iron in place of ρ. It is clear that the SQUID magnetometer setup is at the very least as sensitive as the torsion balance setup discussed in Section 5.4.1, but can be made more sensitive by decreasing the applied magnetic field. The ideal setup would therefore be to initially apply a strong external magnetic field to align the target spins, and then steadily decrease the applied field to maximise the acquired transverse polarisation.

[7] For a given choice of axes, at least one of either the DM wind or magnetic field direction must have some time dependence due to the evolution of the relative velocity between the laboratory and DM reference frames.

5.4.3 A Scalar DM Model as a Case Study

To give a rough estimate of the constraints that can be placed on DM using this method, we consider the two component DM model given in [231], which features a heavy, leptophilic dark vector mediator Z'_μ and complex scalar ϕ with interaction Lagrangian

$$\mathcal{L}_{Z'} = g_\phi^2 Z'_\mu Z'^\mu |\phi|^2 - i g_\phi \phi^* \overset{\leftrightarrow}{\partial_\mu} \phi Z'^\mu - Z'_\mu \bar{\ell} \gamma^\mu (g_L P_L + g_R P_R) \ell \,, \tag{5.4.9}$$

where $\ell \in \{e, \mu, \tau\}$, g_ϕ, g_L and g_R are dimensionless couplings, and $P_{R/L} = (1 \pm \gamma^5)/2$ are the right and left chirality projection operators. Focusing on the case with $\ell = e$, and integrating out the heavy Z' leads to the effective low energy Lagrangian

$$\mathcal{L}_{Z'} = -i \frac{g_\phi (g_R + g_L)}{2 m_{Z'}^2} \left(\phi^* \overset{\leftrightarrow}{\partial_\mu} \phi \right) \bar{e} \gamma^\mu e - i \frac{g_\phi (g_R - g_L)}{2 m_{Z'}^2} \left(\phi^* \overset{\leftrightarrow}{\partial_\mu} \phi \right) \bar{e} \gamma^\mu \gamma^5 e + \dots \tag{5.4.10}$$

Of interest is the second term, which by comparison with (5.3.21) generates an electron energy splitting with magnitude

$$|\Delta E_e| = \frac{2 g_\phi |g_R - g_L|}{m_{Z'}^2} \beta_\oplus \left| n_\phi(\phi) - n_\phi(\phi^*) \right| . \tag{5.4.11}$$

Next, rewriting $|n_\phi(\phi) - n_\phi(\phi^*)| = |\delta_\phi| \rho_{\rm DM}/m_\phi$, where $\delta_\phi \in [-1, 1]$ parameterises the asymmetry between ϕ and ϕ^*, and considering purely axial couplings, $g_R = -g_L = g_A$, we find

$$\begin{aligned} |\Delta E_e| &= \frac{4}{\Lambda_{Z'}^2} \frac{\rho_{\rm DM}}{m_\phi} \beta_\oplus |\delta_\phi| \,, \\ &\approx 1.0 \times 10^{-34}\,\text{eV} \left(\frac{3\,\text{GeV}}{\Lambda_{Z'}} \right)^2 \left(\frac{10\,\text{MeV}}{m_\phi} \right) |\delta_\phi| \,, \end{aligned} \tag{5.4.12}$$

for $\beta_\oplus = 7.6 \times 10^{-4}$ [261], where we have defined the effective new physics scale $\Lambda_{Z'} = m_{Z'}/\sqrt{g_\phi |g_A|}$ and assumed that ϕ makes up the entire local relic density, $\rho_{\rm DM} \approx 0.4\,\text{GeV}\,\text{cm}^{-3}$.

The reference value of $\Lambda_{Z'} = 3\,\text{GeV}$ in (5.4.12) corresponds to the approximate value required to reproduce the relic density for $m_\phi = 10\,\text{MeV}$ via FO production. More

generally, we require

$$\Lambda_{Z'} \approx 3\,\mathrm{GeV}\left(\frac{m_\phi}{10\,\mathrm{MeV}}\right)^{1/2}. \tag{5.4.13}$$

If we now assume FO production of DM, we can estimate the local DM density in terms of $\Lambda_{Z'}$ and m_ϕ as $\rho_{\mathrm{DM}} \sim \Lambda_{Z'}^4/m_\phi^2$ for $m_{Z'}^2 \gg m_\phi^2 > m_e^2$ [231], and the energy shift has a different scaling to (5.4.12):

$$|\Delta E_e| \approx 1.0\times10^{-34}\,\mathrm{eV}\left(\frac{\Lambda_{Z'}}{3\,\mathrm{GeV}}\right)^2\left(\frac{10\,\mathrm{MeV}}{m_\phi}\right)^3|\delta_\phi|\,. \tag{5.4.14}$$

It is instructive to recast both (5.4.12) and (5.4.14) in terms of the constraints that can be placed on the effective new physics scale using the DSE. Given a sensitivity to energy shifts $|\Delta E_0| \gtrsim 10^{-32}\,\mathrm{eV}$, corresponding to the SQUID magnetometer considered in (5.4.8), we find the constraint on the effective new physics scale

$$\Lambda_{Z'} \lesssim 26\,\mathrm{GeV}\left(\frac{m_\phi}{10\,\mathrm{MeV}}\right)^{3/2}\left(\frac{|\Delta E_0|}{10^{-32}\,\mathrm{eV}}\right)^{1/2}\frac{1}{\sqrt{|\delta_\phi|}}\,, \tag{5.4.15}$$

assuming the energy splitting from FO production (5.4.14), which for $O(1)$ values of the asymmetry parameter, i.e. supposing that the dark sector matter-antimatter asymmetry follows that of the visible sector, is just one order of magnitude away from being able to probe $\Lambda_{Z'}$ that reproduces the measured relic density at $m_\phi = 10\,\mathrm{MeV}$. If we instead assume that ϕ makes up the entirety of DM independent of m_ϕ and $\Lambda_{Z'}$, corresponding to the energy splitting (5.4.12), we find the constraint

$$\Lambda_{Z'} \gtrsim 0.30\,\mathrm{GeV}\left(\frac{10\,\mathrm{MeV}}{m_\phi}\right)^{1/2}\left(\frac{10^{-32}\,\mathrm{eV}}{|\Delta E_0|}\right)^{1/2}\sqrt{|\delta_\phi|}\,, \tag{5.4.16}$$

which is once more roughly an order of magnitude away from the FO band (5.4.13).

We show the constraints that could be placed on $\Lambda_{Z'}$ using a SQUID magnetometer in Figure 5.1 as a function of m_ϕ for both the FO and unspecified production scenarios, and compare these with the existing constraints from direction detection experiments [263–265] and anomalous supernova cooling, computed following the method of [231] for the $18\,M_\odot$ progenitor discussed in [262]. As expected, this experiment significantly outperforms existing direct detection experiments for $m_\phi \lesssim 30\,\mathrm{MeV}$.

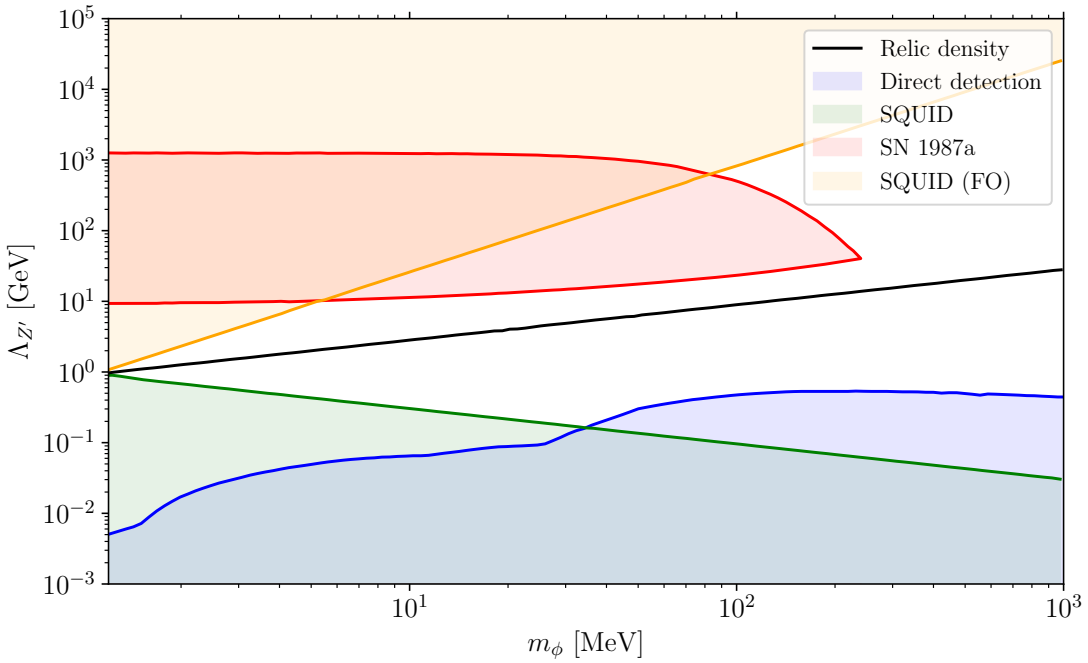

Figure 5.1: Constraint projections on the effective DM coupling, $\Lambda_{Z'} = m_{Z'}/\sqrt{g_\phi g_A}$, from the SQUID magnetometer for the generic (green) and FO (orange) production scenarios, where we assume $\delta_\phi = 1$. We compare these with the constraints from direct detection experiments (blue), and anomalous supernova cooling constraints (red), computed following the method of [231] for the $18\,M_\odot$ progenitor discussed in [262]. For comparison, we show the combination of parameters that reproduce the local relic density for a FO scenario with the black curve, corresponding to the saturation of (5.4.13).

Additionally, if FO is assumed, the SQUID magnetometer experiment is instead able to place constraints on the maximum value of $\Lambda_{Z'}$, owing to the linear scaling of the DSE with the effective coupling. Importantly, this includes regions that are currently unconstrained by SN1987a.

Aside, notice that the energy splitting due to ϕ backgrounds far exceeds that expected from the CνB for the parameter ranges considered here, assuming the same asymmetry for both. It is therefore entirely possible that the DSE completely washes out the νSE. One could also envisage scenarios in which the opposite is true, and the DSE is overwhelmed by the CνB, or those in which one acts as a significant background to the other. This should be taken into consideration when using this

technique, especially as it is difficult to distinguish between the operators responsible for the DSE. Nevertheless, the observation of either the DSE or νSE would be a strong indicator of as-yet-unobserved physics.

5.5 Summary

The key finding of this chapter is that the energy splittings due to the DSE scale linearly with the effective DM coupling, inversely with the DM mass, and are roughly independent of the DM kinematics. Importantly, this differs from traditional DM direct detection experiments, where the sensitivity typically decreases with decreasing DM mass. On the other hand, every operator discussed here requires either a particle-antiparticle or helicity asymmetry in the background to give a non-zero contribution to the DSE. This technique therefore favours chiral models and those with a sizeable chemical potential during production, however we note that either asymmetry may develop post-production through several mechanisms, e.g. DM reflection at surface of the Earth, scattering on polarised backgrounds.

In this work, we have identified two methods through which these tiny energy splittings can be observed. The first utilises an extremely sensitive, polarised torsion balance, which experiences a torque due to the energy splittings induced by the DM background. For a conservative setup, this experiment is sensitive to energy splittings of $\Delta E_\psi \simeq 10^{-28}\,\text{eV}$, but could have a sensitivity to splittings as small as $\Delta E_\psi \simeq 10^{-36}\,\text{eV}$ for a more optimistic setup. The second utilises a SQUID magnetometer to detect the time-varying magnetisation of a target due to the DM background, which acts similarly to an external magnetic field on the target. We estimate that this experiment will be sensitive to splittings of $\Delta E_\psi \simeq 10^{-32}\,\text{eV}$.

Finally, we have explored a scalar DM model, considering both the case where the new scalar constitutes the entire local DM density regardless of the model parameters, and the more realistic scenario where it is produced via the FO mechanism.

In both scenarios, we showed the SQUID magnetometer proposal is able to exclude regions of parameter space that are not already ruled out by direct detection experiments or SN1987a, provided that there is a sizeable asymmetry in the DM background. For the range of parameters considered, we also demonstrated that the DSE for the scalar DM model far exceeded the Stodolsky effect for neutrinos, provided that the asymmetry in both backgrounds was comparable. Overall, the DSE is a powerful tool to constrain DM models in otherwise difficult-to-test regions of parameter space.

Chapter 6

Conclusions

In this thesis, we have highlighted some methods to detect, or constrain, some of the hypothetical particles that could solve the dark matter problem. This involved considering several types of experiments in order to gain as wide a view as possible. Notably, we have introduced the concept of fifth forces experiments, in which one measures the effect of a supposed interaction potential resulting from the exchange of virtual particles. These techniques were considered in the context of effective theories, in which all high-energy behaviour in a theory is integrated out, leaving only numerical coefficients as parameters to measure. In particular, we examined the general effective theory of axion-like particles, revealing its properties at various scales, down from a high symmetry breaking scale to the energies occurring in bound systems.

In Chapter 3, we re-examined the low-energy potential for a macroscopic fifth force generated from the exchange of two axions. The shift symmetry of the linear axion interactions led to a potential falling off as $V(r) \sim 1/r^5$. We found that in the case of the QCD axion, higher-order terms in the Lagrangian were induced by non-perturbative effects occurring upon matching the theory to the chiral Lagrangian. These higher-order terms break the shift symmetry and lead to the dominant contribution to the potential scaling as $V(r) \sim 1/r^3$. These terms are generated by the same physics responsible for the axion mass, and therefore the new contributions to

the potential induce a different force for external nucleons and leptons. We demonstrated how this result affects the sensitivity of searches for new long-range forces, via the example of a particular experiment measuring the Casimir force between two objects, to find a substantial enhancement of the bound obtained using the shift symmetry breaking induced $V(r) \sim 1/r^3$ potential instead of the shift symmetry preserving interaction potential derived.

The focus of Chapter 4 was the phenomenology of the unique dimension-six operator respecting the shift symmetry: the axion-Higgs portal, with a scalar particle coupling quadratically to the Standard Model Higgs boson. We compared constraints from Higgs physics, flavour-violating and radiative meson decays, bounds from atomic spectroscopy searching for fifth forces, and astrophysical observables, and, as might have been expected, found the strongest bounds to be from tree-level Higgs decays. In contrast to the QCD axion, axions interacting through the axion-Higgs portal are stable and can provide a dark matter candidate for any axion mass. For comparison, we also derived Higgs, flavour, and spectroscopy constraints, and the parameter space for which the scalar Higgs portal without derivative interactions could explain dark matter.

Finally, in Chapter 5, we presented a comprehensive discussion of the Stodolsky effect for dark matter, and discussed two techniques to measure the effect and constrain the dark matter candidates parameter space. We generalised the Stodolsky effect, the spin-dependent shift in the energy of a Standard Model fermion sitting in a bath of neutrinos, to dark matter, and gave expressions for the induced energy shifts for candidates from spin-0 to spin-$\frac{3}{2}$, considering all effective operators up to mass dimension-6. In all cases, the effect scales inversely with the candidate mass, but requires an asymmetric background. We showed that a torsion balance experiment is sensitive to energy shifts of $\Delta E \gtrsim 10^{-28}\,\text{eV}$, whilst a more intricate setup using a SQUID magnetometer is sensitive to shifts of $\Delta E \gtrsim 10^{-32}\,\text{eV}$. Finally, we computed the energy shifts for a model of scalar dark matter, and demonstrated that the Stodolsky effect could be used to constrain regions of parameter space that

are not presently excluded.

In summary, in this thesis, we have provided a consistent framework to apply bounds from fifth-force type experiments to axions and ALPs, and other possible mediators, taking all running effects into account. We have also worked out the existing constraints on a new dark matter model, namely the axion-Higgs portal. Finally, we have proposed a new experimental approach to search for various dark matter candidates in a model independent way via the dark Stodolsky effect.

Building upon the work done in this thesis, [266] will set new bounds on the effective QCD axion model used throughout this work. There, a wide range of experiments and quantum sensors are reviewed and used to derive various bounds on this generic model, effectively combining several independent existing bounds consistently. We will then have demonstrated the power of an effective theory standpoint in searches for dark matter: by considering the phenomenology of a set of individual operators, we are able to place a wide set of bounds on a wide range of models at once.

Appendix A

Spinor Contractions

We give here a short overview of the NR spinor identities used throughout the computation of IPs. For convenience, we will use the chiral, or Weyl, basis. In this basis, the Dirac matrices are

$$\gamma^\mu = \begin{pmatrix} 0 & \sigma^\mu \\ \bar{\sigma}^\mu & 0 \end{pmatrix} \quad \text{and} \quad \gamma^5 = \begin{pmatrix} -\mathbb{1}_2 & 0 \\ 0 & \mathbb{1}_2 \end{pmatrix}, \tag{A.0.1}$$

where $\sigma^\mu \equiv (\mathbb{1}_2, \boldsymbol{\sigma})$ and $\bar{\sigma}^\mu \equiv (\mathbb{1}_2, -\boldsymbol{\sigma})$, with $\boldsymbol{\sigma}$ the Pauli vector and $\mathbb{1}_2$ the 2×2 identity matrix. For fermions of mass m and 4-momentum p^μ we have the spinors

$$u_s(p) = \begin{pmatrix} \sqrt{p \cdot \sigma}\xi_s \\ \sqrt{p \cdot \bar{\sigma}}\xi_s \end{pmatrix} \quad \text{and} \quad \bar{u}_s(p) \equiv u_s^\dagger(p)\gamma^0 = \begin{pmatrix} \xi_s^\dagger\sqrt{p \cdot \bar{\sigma}} & \xi_s^\dagger\sqrt{p \cdot \sigma} \end{pmatrix} \tag{A.0.2}$$

with ξ_s a two-component spinor, normalised such that $\xi_r^\dagger \xi_s = \delta_{rs}$.

Using the definitions above, and applying the NR limit $|\boldsymbol{p}| \to 0$ in the incoming particles CoM frame, we can derive the following identities:

$$\bar{u}_r(p_2)u_s(p_1) = 2m\delta_{rs} + O\left(|\boldsymbol{p}|\right) \tag{A.0.3a}$$

$$\bar{u}_r(p_2)\gamma^5 u_s(p_1) = (\boldsymbol{p}_1 - \boldsymbol{p}_2) \cdot \boldsymbol{\sigma}\delta_{rs} + O\left(|\boldsymbol{p}|^2\right) \tag{A.0.3b}$$

$$\bar{u}_r(p_2)\gamma^\mu u_s(p_1) = 2m\delta_0^\mu\delta_{rs} + O\left(|\boldsymbol{p}|\right) \tag{A.0.3c}$$

$$\bar{u}_r(p_2)\gamma^\mu\gamma^5 u_s(p_1) = 2m\delta_k^\mu\sigma^k\delta_{rs} + O\left(|\boldsymbol{p}|\right) \tag{A.0.3d}$$

For the identities involving γ^μ we have also used the decomposition $\gamma^\mu = \delta^\mu_0\gamma^0 + \delta^\mu_k\gamma^k$ with $k = 1, 2, 3$.

Appendix B

Kinematics and Angular Integrals

In this Appendix we give supplementary material useful for the calculation of fifth forces in Chapter 3, that is, kinematics and the solutions of angular integrals appearing in the computations of IPs.

B.1 Kinematics

From Figures 3.1 and 3.3, we have to consider the loop momenta k and k' of the exchange particles with masses m_i and m_j respectively, the momentum transfer q and the four external momenta $p_{1,2,3,4}$ of the fermions with masses M_1 and M_2. In the t rest frame used earlier, these are given by

$$q = \left(\sqrt{t},\, \mathbf{0}\right) , \tag{B.1.1a}$$

$$k = \left(\frac{t + 2\hat{m}\,\delta m}{2\sqrt{t}},\, \frac{1}{2}\frac{\sqrt{\tau_\delta}}{\sqrt{t}}\sqrt{\tau}\hat{\boldsymbol{k}}\right) , \tag{B.1.1b}$$

$$k' = \left(\frac{t - 2\hat{m}\,\delta m}{2\sqrt{t}},\, -\frac{1}{2}\frac{\sqrt{\tau_\delta}}{\sqrt{t}}\sqrt{\tau}\hat{\boldsymbol{k}}\right) , \tag{B.1.1c}$$

$$p_1 = \left(\frac{1}{2}\sqrt{t},\, \frac{1}{2}\sqrt{\tau_1}\hat{\boldsymbol{p}}\right) , \tag{B.1.1d}$$

$$p_2 = \left(-\frac{1}{2}\sqrt{t},\, \frac{1}{2}\sqrt{\tau_2}\hat{\boldsymbol{p}}'\right) , \tag{B.1.1e}$$

$$p_3 = \left(-\frac{1}{2}\sqrt{t},\, \frac{1}{2}\sqrt{\tau_1}\hat{\boldsymbol{p}}\right) , \tag{B.1.1f}$$

$$p_4 = \left(\frac{1}{2}\sqrt{t},\, \frac{1}{2}\sqrt{\tau_2}\hat{\boldsymbol{p}}'\right) , \tag{B.1.1g}$$

using the shorthand notations $\hat{m} = \frac{1}{2}(m_i + m_j)$, $\delta m = m_i - m_j$, and $\tau = t - 4\hat{m}^2$, $\tau_\delta = t - \delta m^2$, $\tau_1 = t - 4M_1^2$ and $\tau_2 = t - 4M_2^2$. Then we write the 28 possible momentum contractions:

$$q^2 = t \qquad k^2 = m_i^2 \qquad k'^2 = m_j^2 \qquad p_1^2 = p_3^2 = M_1^2 \qquad p_2^2 = p_4^2 = M_2^2$$

$$q \cdot k = \frac{1}{2}\left(t + 2\hat{m}\,\delta m\right) \qquad q \cdot k' = \frac{1}{2}\left(t - 2\hat{m}\,\delta m\right) \qquad k \cdot k' = \frac{1}{4}\left(t + \tau_\delta\right)$$

$$q \cdot p_1 = q \cdot p_4 = \frac{t}{2} \qquad q \cdot p_2 = q \cdot p_3 = -\frac{t}{2}$$

$$p_1 \cdot p_3 = -\frac{1}{4}(t + \tau_1) \qquad p_2 \cdot p_4 = -\frac{1}{4}(t + \tau_2)$$

$$p_1 \cdot p_2 = p_3 \cdot p_4 = \frac{1}{4}\left(-t - \sqrt{\tau_1}\sqrt{\tau_2}\hat{\boldsymbol{p}} \cdot \hat{\boldsymbol{p}}'\right) \qquad p_1 \cdot p_4 = p_2 \cdot p_3 = \frac{1}{4}\left(t - \sqrt{\tau_1}\sqrt{\tau_2}\hat{\boldsymbol{p}} \cdot \hat{\boldsymbol{p}}'\right)$$

$$k \cdot p_1 = \frac{1}{4}\left(t + 2\hat{m}\,\delta m - \frac{\sqrt{\tau_\delta}}{\sqrt{t}}\sqrt{\tau\tau_1}\hat{\boldsymbol{k}} \cdot \hat{\boldsymbol{p}}\right)$$
$$k \cdot p_2 = \frac{1}{4}\left(-t - 2\hat{m}\,\delta m - \frac{\sqrt{\tau_\delta}}{\sqrt{t}}\sqrt{\tau\tau_2}\hat{\boldsymbol{k}} \cdot \hat{\boldsymbol{p}}'\right)$$
$$k \cdot p_3 = \frac{1}{4}\left(-t - 2\hat{m}\,\delta m - \frac{\sqrt{\tau_\delta}}{\sqrt{t}}\sqrt{\tau\tau_1}\hat{\boldsymbol{k}} \cdot \hat{\boldsymbol{p}}\right)$$
$$k \cdot p_4 = \frac{1}{4}\left(t + 2\hat{m}\,\delta m - \frac{\sqrt{\tau_\delta}}{\sqrt{t}}\sqrt{\tau\tau_2}\hat{\boldsymbol{k}} \cdot \hat{\boldsymbol{p}}'\right)$$

$$k' \cdot p_1 = \frac{1}{4}\left(t - 2\hat{m}\,\delta m + \frac{\sqrt{\tau_\delta}}{\sqrt{t}}\sqrt{\tau\tau_1}\hat{\boldsymbol{k}} \cdot \hat{\boldsymbol{p}}\right)$$
$$k' \cdot p_2 = \frac{1}{4}\left(-t + 2\hat{m}\,\delta m + \frac{\sqrt{\tau_\delta}}{\sqrt{t}}\sqrt{\tau\tau_2}\hat{\boldsymbol{k}} \cdot \hat{\boldsymbol{p}}'\right)$$
$$k' \cdot p_3 = \frac{1}{4}\left(-t + 2\hat{m}\,\delta m + \frac{\sqrt{\tau_\delta}}{\sqrt{t}}\sqrt{\tau\tau_1}\hat{\boldsymbol{k}} \cdot \hat{\boldsymbol{p}}\right)$$
$$k' \cdot p_4 = \frac{1}{4}\left(t - 2\hat{m}\,\delta m + \frac{\sqrt{\tau_\delta}}{\sqrt{t}}\sqrt{\tau\tau_2}\hat{\boldsymbol{k}} \cdot \hat{\boldsymbol{p}}'\right)$$

We further define the combined momenta,

$$P_1 \equiv p_1 + p_3 = (0,\, \sqrt{\tau_1}\hat{\boldsymbol{p}}) , \tag{B.1.2a}$$

$$P_2 \equiv p_2 + p_4 = \left(0,\, \sqrt{\tau_2}\hat{\boldsymbol{p}}'\right) , \tag{B.1.2b}$$

$$W \equiv p_1 + p_2 = p_3 + p_4 \,. \tag{B.1.2c}$$

Immediately we can see that $P_1 \cdot q = P_2 \cdot q = 0$. We also have the contractions

$$P_1^2 = -\tau_1 \,, \qquad P_2^2 = -\tau_2 \quad \text{and} \quad P_1 \cdot P_2 = -y\sqrt{\tau_1}\sqrt{\tau_2} \,.$$

B.2 Angular Integrals

Adapting the basis used in [129], we parameterise the relevant dot products as

$$\hat{\boldsymbol{p}} \cdot \hat{\boldsymbol{p}}' = y \,, \qquad \hat{\boldsymbol{k}} \cdot \hat{\boldsymbol{p}} = \cos\theta \,, \qquad \hat{\boldsymbol{k}} \cdot \hat{\boldsymbol{p}}' = y\cos\theta + \sqrt{1-y^2}\sin\theta\cos\phi \,, \tag{B.2.1}$$

to define our own basis of functions in (3.1.13) as

$$\mathcal{I}^{(a,b)} = \int \frac{\mathrm{d}^2\Omega}{4\pi} \, \left(Y + Z\hat{\boldsymbol{k}} \cdot \hat{\boldsymbol{p}}\right)^a \left(Y' + Z'\hat{\boldsymbol{k}} \cdot \hat{\boldsymbol{p}}'\right)^b \,, \tag{B.2.2}$$

and perform the angular integration over $\mathrm{d}^2\Omega = \sin\theta \, \mathrm{d}\theta\mathrm{d}\phi$. Some of the solutions are given below:

$$\mathcal{I}^{(0,0)} = 1 \,, \tag{B.2.3a}$$

$$\mathcal{I}^{(-1,0)} = \frac{1}{Z} \operatorname{arctanh} \frac{Z}{Y} \,, \tag{B.2.3b}$$

$$\mathcal{I}^{(0,-1)} = \frac{1}{Z'} \operatorname{arctanh} \frac{Z'}{Y'} \,, \tag{B.2.3c}$$

$$\mathcal{I}^{(-1,-1)} = \frac{1}{\sqrt{X}} \operatorname{arctanh} \frac{\sqrt{X}}{YY' - yZZ'} \,, \tag{B.2.3d}$$

$$\mathcal{I}^{(1,0)} = Y \,, \tag{B.2.3e}$$

$$\mathcal{I}^{(0,1)} = Y' \,, \tag{B.2.3f}$$

$$\mathcal{I}^{(1,-1)} = y\frac{Z}{Z'} + \left(\frac{Y}{Y'} - y\frac{Z}{Z'}\right)\frac{Z'}{Y'} \,, \tag{B.2.3g}$$

$$\mathcal{I}^{(-1,1)} = y\frac{Z'}{Z} + \left(\frac{Y'}{Y} - y\frac{Z'}{Z}\right)\frac{Y}{Z} \operatorname{arctanh} \frac{Z}{Y} \,, \tag{B.2.3h}$$

$$\mathcal{I}^{(1,1)} = YY' + \frac{1}{3}yZZ' \,, \tag{B.2.3i}$$

with $X \equiv \left(YY' - yZZ'\right)^2 - \left(Y^2 - Z^2\right)\left(Y'^2 - Z'^2\right)$ and where arctanh designates the principal branch of the inverse hyperbolic tangent function.

The solutions involving negative coefficients a or b are strictly only valid for $Y, Z, Y', Z' \in \mathbb{R}$ when $|Y| > |Z|$ and $|Y'| > |Z'|$, since the integrand acquires poles otherwise. However, for the cases that are physically relevant in this work, this will never happen. To see this, let us consider one the triangle diagram in Figure 3.5 where the angular integrals involve terms of the form

$$\int \frac{\mathrm{d}^2\Omega}{4\pi} \frac{1}{(k-p_1)^2 - M_1^2} = \int \frac{\mathrm{d}^2\Omega}{4\pi} \frac{1}{m^2 - \frac{1}{2}t - \frac{1}{2}\sqrt{\tau}\sqrt{\tau_1}\hat{\boldsymbol{k}}\cdot\hat{\boldsymbol{p}}}\,, \tag{B.2.4}$$

where we recognise an $\mathcal{I}^{(-1,0)}$ type integral with $Y = m^2 - t/2$ and $Z = -\frac{1}{2}\sqrt{\tau}\sqrt{\tau_1}$. The integrand is analytic everywhere except at a pole when the denominator vanishes. Consider two cases:

- When $t < 4M^2$, τ_1 is negative and Z is imaginary. Since Y is real and strictly negative in the t integration region, we have $Y + Z\hat{\boldsymbol{k}}\cdot\hat{\boldsymbol{p}} \neq 0$.
- When $t \geq 4M^2$, τ_1 is positive and Z is real, and the denominator has a zero when $|Y| \leq |Z|$. This occurs when $t < 4m^2 - \frac{m^4}{M^2}$ which lies outside the t integration region, therefore the integrand has no poles in this region.

A similar reasoning applies to the $\mathcal{I}^{(-1,-1)}$ integral with Z or Z' real or imaginary.

Appendix C

Lab Frame Averaging of Energy Shifts

In this Appendix we will describe the averaging procedure used to compute the energy shifts in the lab frame. We begin by assuming that the DM is described by an isothermal spherical halo, with galaxy frame velocity distribution

$$f(\boldsymbol{p}) = \left(\frac{2\pi}{m_{\rm DM}^2\sigma^2}\right)^{\frac{3}{2}} e^{-\frac{|\boldsymbol{p}|^2}{2m_{\rm DM}^2\sigma^2}}\,, \tag{C.0.1}$$

where $\boldsymbol{p}$ is the DM momentum in the galactic reference frame, $m_{\rm DM}$ is its mass and σ is the velocity dispersion. The normalisation factor is found by requiring that $\int \frac{\mathrm{d}^3\boldsymbol{p}}{(2\pi)^3} f(\boldsymbol{p}) = 1$. As a result of the frame transformation, DM particles in the lab frame will not follow (C.0.1) but instead the transformed distribution function $f_{\rm lab}$, such that the average of some lab frame quantity $X_{\rm lab}$ will be given by

$$\langle X_{\rm lab}\rangle = \int \frac{d^3\boldsymbol{p}}{(2\pi)^3} X_{\rm lab} f_{\rm lab}(\boldsymbol{p})\,. \tag{C.0.2}$$

To find $f_{\rm lab}(\boldsymbol{p})$, we first note that since all velocities involved are small, the momentum of the DM particle in the lab frame $\boldsymbol{p}_{\rm lab}$ can be written in terms of the

relative frame velocity $\boldsymbol{\beta}_\oplus$ as

$$\boldsymbol{p}_{\rm lab} \simeq \boldsymbol{p} + m_{\rm DM}\boldsymbol{\beta}_\oplus = |\boldsymbol{p}| \begin{pmatrix} \cos\phi\sin\theta \\ \sin\phi\sin\theta \\ \cos\theta \end{pmatrix} + m_{\rm DM}\beta_\oplus \begin{pmatrix} 0 \\ 0 \\ 1 \end{pmatrix}, \tag{C.0.3}$$

where $\beta_\oplus \equiv |\boldsymbol{\beta}_\oplus|$, and we have chosen $\boldsymbol{\beta}_\oplus || z$ for simplicity. This choice makes no difference at the level of averaging, but becomes important when considering experimental setups. We will therefore write our final expressions for averaged quantities in terms of a general orientation of $\boldsymbol{\beta}_\oplus$. Next, since $f_{\rm lab}(\boldsymbol{p}_{\rm lab}) = f(\boldsymbol{p})$, the lab frame distribution function will satisfy

$$f_{\rm lab}(\boldsymbol{p}) = f(\boldsymbol{p} - m_{\rm DM}\boldsymbol{\beta}_\oplus) = \left(\frac{2\pi}{m_{\rm DM}^2\sigma^2}\right)^{\frac{3}{2}} e^{-\frac{|\boldsymbol{p}|^2 + m_{\rm DM}^2\beta_\oplus}{2m_{\rm DM}^2\sigma^2}} e^{\frac{|\boldsymbol{p}|\beta_\oplus\cos\theta}{m_{\rm DM}\sigma^2}}, \tag{C.0.4}$$

which can be readily plugged into (C.0.2) to compute averaged lab frame quantities.

In addition to the distribution function, we must also write the lab frame polarisation vectors in terms of DM reference frame quantities. To do so, we rotate the polarisation vectors (5.3.29) to point along an arbitrary axis, and then use $\boldsymbol{p}_{\rm lab}$ to rewrite angles in the lab frame in terms of those in the DM frame, yielding

$$\epsilon_+^\mu = (\epsilon_-^\mu)^* = \frac{1}{\sqrt{2}} \begin{pmatrix} 0 \\ \frac{1}{|\boldsymbol{p}_{\rm lab}|}\cos\phi\,(|\boldsymbol{p}|\cos\theta + \beta_\oplus m_{\rm DM}) - i\sin\phi \\ \frac{1}{|\boldsymbol{p}_{\rm lab}|}\sin\phi\,(|\boldsymbol{p}|\cos\theta + \beta_\oplus m_{\rm DM}) + i\cos\phi \\ -\frac{|\boldsymbol{p}|}{|\boldsymbol{p}_{\rm lab}|}\sin\theta \end{pmatrix}, \tag{C.0.5}$$

$$\epsilon_L^\mu = \begin{pmatrix} \frac{|\boldsymbol{p}_{\rm lab}|}{m_{\rm DM}} \\ \frac{|\boldsymbol{p}|}{|\boldsymbol{p}_{\rm lab}|}\cos\phi\sin\theta \\ \frac{|\boldsymbol{p}|}{|\boldsymbol{p}_{\rm lab}|}\sin\phi\sin\theta \\ \frac{1}{|\boldsymbol{p}_{\rm lab}|}\,(|\boldsymbol{p}|\cos\theta + \beta_\oplus m_{\rm DM}) \end{pmatrix}, \tag{C.0.6}$$

again assuming $\boldsymbol{\beta}_\oplus || z$.

Relaxing the assumption $\boldsymbol{\beta}_\oplus || z$, we find the averages relevant to the operators con-

sidered in this work .

$$
\begin{aligned}
\left\langle \frac{1}{E_{\rm DM}}(\boldsymbol{p}_{\rm DM}\cdot\boldsymbol{S}_\psi)\right\rangle &= 2\beta_\oplus s_{\psi,\parallel}\\
\left\langle \frac{1}{E_{\rm DM}}(p_{\rm DM}\cdot S_\psi)\right\rangle &= -2\beta_\oplus s_{\psi,\parallel}\\
\left\langle \frac{1}{E_{\rm DM}}(S_{\rm DM}\cdot S_\psi)\right\rangle &= \left[\frac{(1-8\beta_r^2)}{8\beta_r^2}\,\mathrm{erf}\,(2\beta_r)-\frac{1}{2\sqrt{\pi}\beta_r}e^{-4\beta_r^2}\right]\frac{s_{\psi,\parallel}}{m_{\rm DM}}\\
&\approx -\frac{7}{8}\frac{s_{\psi,\parallel}}{m_{\rm DM}}+O(1-\beta_r)\\
\left\langle \frac{1}{E_{\rm DM}}(p_{\rm DM}\cdot S_\psi)(S_{\rm DM}\cdot p_\psi)\right\rangle &= \left[\frac{(1-16\beta_r^2-64\beta_r^4)}{16\beta_r^4}\,\mathrm{erf}\,(2\beta_r)\right.\\
&\quad\left.-\frac{(1+8\beta_r^2)}{4\sqrt{\pi}\beta_r}e^{-4\beta_r^2}\right]\beta_c^2 m_\psi s_{\psi,\parallel}\\
&\approx -5\beta_c^2 m_\psi s_{\psi,\parallel}+O(1-\beta_r)\\
\left\langle \frac{1}{E_{\rm DM}}(p_{\rm DM}\cdot p_\psi)(S_{\rm DM}\cdot S_\psi)\right\rangle &= \left[\frac{(1-8\beta_r^2)}{8\beta_r^2}\,\mathrm{erf}\,(2\beta_r)-\frac{1}{2\sqrt{\pi}\beta_r}e^{-4\beta_r^2}\right]m_\psi s_{\psi,\parallel}\\
&\approx -\frac{7}{8}m_\psi s_{\psi,\parallel}+O(1-\beta_r)\\
\left\langle \frac{1}{E_{\rm DM}}\varepsilon_{\alpha\beta\mu\nu}p_{\rm DM}^\alpha p_\psi^\beta S_{\rm DM}^\mu S_\psi^\nu\right\rangle &= 0\\
\left\langle \frac{1}{E_{\rm DM}}\varepsilon_{\alpha\beta\mu\nu}p_\psi^\alpha S_\psi^\beta \epsilon_\pm^{*\mu}\epsilon_\pm^\nu\right\rangle &= \pm i\left[\frac{(1-8\beta_r^2)}{8\beta_r^2}\,\mathrm{erf}\,(2\beta_r)-\frac{1}{2\sqrt{\pi}\beta_r}e^{-4\beta_r^2}\right]\frac{m_\psi}{m_{\rm DM}}s_{\psi,\parallel}\\
&\approx \mp\frac{7i}{8}\frac{m_\psi}{m_{\rm DM}}s_{\psi,\parallel}+O(1-\beta_r)\\
\left\langle \frac{1}{E_{\rm DM}}\varepsilon_{\alpha\beta\mu\nu}p_\psi^\alpha S_\psi^\beta \epsilon_L^{*\mu}\epsilon_L^\nu\right\rangle &= 0\\
\left\langle \frac{1}{E_{\rm DM}}(p_\psi\cdot\epsilon_\pm)(S_\psi\cdot\epsilon_\pm^*)\right\rangle &= 0\\
\left\langle \frac{1}{E_{\rm DM}}(p_\psi\cdot\epsilon_L)(S_\psi\cdot\epsilon_L^*)\right\rangle &= -\frac{2m_\psi}{m_{\rm DM}}\beta_\oplus s_{\psi,\parallel}\\
\left\langle \frac{1}{E_{\rm DM}}(\boldsymbol{p}_X\cdot\boldsymbol{\epsilon}_\pm)(\epsilon_\pm^*\cdot S_\psi)\right\rangle &= 0\\
\left\langle \frac{1}{E_{\rm DM}}(\boldsymbol{p}_X\cdot\boldsymbol{\epsilon}_L)(\epsilon_L^*\cdot S_\psi)\right\rangle &= -2\beta_\oplus s_{\psi,\parallel}\\
\left\langle \frac{1}{E_{\rm DM}}\varepsilon_{\alpha\beta i\nu}\epsilon_\pm^{*\alpha}\epsilon_\pm^\beta \boldsymbol{p}_X^i S_\psi^\nu\right\rangle &= 0\\
\left\langle \frac{1}{E_{\rm DM}}\varepsilon_{\alpha\beta i\nu}\epsilon_L^{*\alpha}\epsilon_L^\beta \boldsymbol{p}_X^i S_\psi^\nu\right\rangle &= 0\,,
\end{aligned}
$$

with $s_{\psi,\parallel}=(\boldsymbol{\beta}_\oplus\cdot\boldsymbol{s}_\psi)/\beta_\oplus$ and $\beta_r=\beta_\oplus/\beta_c$, where $\beta_c=\sqrt{2}\sigma$ is the circular velocity

of the galaxy. The presence of $s_{\psi,\parallel}$ indicates that only the spin state directed along the DM wind experiences an energy shift. We will not include this factor explicitly in the main text.

Appendix D

Fermion spin precession

Here we derive the spin precession of an SM fermion in a combined magnetic and DM background field that gives rise to the transverse magnetisation (5.4.6) in Section 5.4.2. To do so, we need to set up the differential equation that governs the evolution of the SM fermion spin. There will be two components to this: the precession due to the DM background, and the precession due to an external magnetic field. Both of these are due to the same effect, a non-diagonal Hamiltonian resulting from the energy splittings due to background fields. We begin with the time-dependent Schrödinger equation, which for our system takes the form

$$i\frac{\partial}{\partial t}\psi(x,t) = \left(H_{\rm kin}(x) + V_{\rm DM} + V_B\right)\psi(x,t)\,, \tag{D.0.1}$$

where $\psi(x,t)$ is the fermion wavefunction, $H_{\rm kin}(x)$ is its kinetic Hamiltonian, which is spin and time-independent, whilst $V_{\rm DM}$ and V_B are the potentials due to the DM background and applied magnetic field $\boldsymbol{B}_{\rm ext}$ respectively, which are spin-dependent and we will treat as constant in time here[1]. This motivates the factorisation

$$\psi(x,t) = X(x)T(t)\,, \tag{D.0.2}$$

[1] In truth, at least one of these must be time-dependent. If we fix our coordinate system in the lab frame, then due to the relative motion of the Earth to the DM reference frame, the direction of the background wind will change in time. However, this can alternatively be accounted for by weighting the collected data by the projection of the relative velocity onto the magnetic field direction. See supplementary material S10.1 of [267] for details of the weighting, and [268] for a full parameterisation of the relevant coordinate systems.

where $X(x)$ is a scalar, containing the spatial components of the wavefunction, and $T(t)$ is an eigenspinor of the form

$$T(t) = \begin{pmatrix} T_+(t) \\ T_-(t) \end{pmatrix}, \qquad |T(t)|^2 = 1\,. \tag{D.0.3}$$

This factorisation makes (D.0.1) separable, but it is easier to note that

$$H_{\rm kin}(x)X(x) = E_{\rm kin}X(x)\,, \tag{D.0.4}$$

such that we can absorb $E_{\rm kin}$ as a time-independent, spin-diagonal contribution to the potential. The overall factor of $X(x)$ can then be factored out, allowing us to write

$$\left(i\frac{\partial}{\partial t} - H\right)T(t) = 0\,, \tag{D.0.5}$$

where H is the total Hamiltonian, including the spin-diagonal contribution from $H_{\rm kin}$. If the magnetic field is defined such that it points along z, then the z oriented spin state will experience an energy shift. Additionally, the up and down spin states should experience a shift of opposite sign. The potential due to the magnetic field should therefore be proportional to the spin operator along z, that is

$$V_B = \frac{\Delta E_B}{2}S_z = \frac{\Delta E_B}{2}\begin{pmatrix} 1 & 0 \\ 0 & -1 \end{pmatrix}, \tag{D.0.6}$$

where ΔE_B is the energy shift due to the magnetic field. We see that this has the desired properties, as if we act on an S_z eigenstate with eigenvalue[2] $s_z = \pm 1$, we get the eigenvalue $s_z\Delta E_B/2$. Next, we seek to do the same for the potential due to the DM, which should be directed along the DM wind. Explicitly,

$$V_{\rm DM} = \frac{\Delta E_\psi}{2}\left(\boldsymbol{\beta}_\oplus \cdot \boldsymbol{S}\right) = \frac{\Delta E_\psi}{2}\begin{pmatrix} \beta_z & \beta_x - i\beta_y \\ \beta_x + i\beta_y & -\beta_z \end{pmatrix}, \tag{D.0.7}$$

where $\beta_i = (\boldsymbol{\beta}_\oplus \cdot \hat{\boldsymbol{e}}_i)/\beta_\oplus \in [-1, 1]$ is the fraction of the relative frame velocity along the direction i. We should also include a diagonal term due to the spin-independent

[2]We adopt the convention $S_i = \sigma_i$, with $i \in \{x, y, z\}$ and σ denoting a Pauli matrix.

effects from the DM, however this can simply be absorbed into E_{kin}. The total Hamiltonian is then

$$H = \frac{1}{2}\begin{pmatrix} 2E_{\text{kin}} + \Delta E_B + \Delta E_\psi \beta_z & \Delta E_\psi \left(\beta_x - i\beta_y\right) \\ \Delta E_\psi \left(\beta_x + i\beta_y\right) & 2E_{\text{kin}} - \Delta E_B - \Delta E_\psi \beta_z \end{pmatrix}, \tag{D.0.8}$$

such that the solution to (D.0.5) is given by

$$T_\pm(t) = \left[s_\pm \cos\left(\frac{\omega}{2}t\right) - \frac{\left(\beta_x \mp i\beta_y\right) R s_\mp \pm (1 \pm \beta_z R)\, s_\pm}{\sqrt{1 + 2\beta_z R + R^2}} i \sin\left(\frac{\omega}{2}t\right) \right] e^{-iE_{\text{kin}}t}, \tag{D.0.9}$$

where $\omega \equiv \Delta E_B \sqrt{1 + 2\beta_z R + R^2}$ is the (angular) precession frequency of the system, proportional to the Larmor frequency, $s_\pm = T_\pm(0)$ are the initial values of the SM fermion eigenspinor, and $R \equiv \Delta E_\psi / \Delta E_B \in [-1, 1]$ is the ratio of the energy shifts due to each of the background potentials. We further note that s_+ is always real, while s_- may be complex.

To compute the spin precession using $T_\pm$, we note that the time derivative of some operator $\mathcal{O}$ is given by Heisenberg's equation of motion

$$\frac{\mathrm{d}\mathcal{O}}{\mathrm{d}t} = i[H, \mathcal{O}], \tag{D.0.10}$$

such that the time derivative of each of the expectation values, s_i, is

$$\frac{\mathrm{d}s_i}{\mathrm{d}t} = T(t)^\dagger \left(\frac{\mathrm{d}S_i}{\mathrm{d}t}\right) T(t). \tag{D.0.11}$$

Plugging in (D.0.9), we find

$$\frac{\mathrm{d}s_x}{\mathrm{d}t} = \left(\frac{\beta_x(1 + \beta_z R)}{\sqrt{1 + 2\beta_z R + R^2}} \sin(\omega t) + \beta_y \cos(\omega t) \right) \Delta E_\psi, \tag{D.0.12a}$$

$$\frac{\mathrm{d}s_y}{\mathrm{d}t} = \left(\frac{\beta_y(1 + \beta_z R)}{\sqrt{1 + 2\beta_z R + R^2}} \sin(\omega t) - \beta_x \cos(\omega t) \right) \Delta E_\psi, \tag{D.0.12b}$$

$$\frac{\mathrm{d}s_z}{\mathrm{d}t} = \left(-\frac{\left(1 - \beta_z^2\right) R}{\sqrt{1 + 2\beta_z R + R^2}} \sin(\omega t) \right) \Delta E_\psi, \tag{D.0.12c}$$

where we have related $s_\pm$ to the initial values of s_x, s_y and s_z, using

$$s_{x,0} = T(0)^\dagger S_x\, T(0) = 2s_+ \,\mathrm{Re}\,(s_-) = 0, \tag{D.0.13a}$$

$$s_{y,0} = T(0)^\dagger S_y \, T(0) = 2 s_+ \, \mathrm{Im}\,(s_-) = 0\,, \tag{D.0.13b}$$

$$s_{z,0} = T(0)^\dagger S_z \, T(0) = |s_+|^2 - |s_-|^2 = 1\,, \tag{D.0.13c}$$

and assumed that the spins are initially aligned with the external magnetic field. Notice that all three of (D.0.12), in particular those along x and y, are proportional to the energy splitting due to the background DM field, and so will vanish in its absence. These equations are readily solved to find the expectation values of the SM fermion spin as a function of time

$$s_x(t) = \frac{2R}{\sqrt{1+2\beta_z R + R^2}} \left[\frac{\beta_x(1+\beta_z R)}{\sqrt{1+2\beta_z R + R^2}} \sin^2\left(\frac{\omega}{2}t\right) + \frac{\beta_y}{2}\sin\left(\omega t\right) \right]\,, \tag{D.0.14a}$$

$$s_y(t) = \frac{2R}{\sqrt{1+2\beta_z R + R^2}} \left[\frac{\beta_y(1+\beta_z R)}{\sqrt{1+2\beta_z R + R^2}} \sin^2\left(\frac{\omega}{2}t\right) - \frac{\beta_x}{2}\sin\left(\omega t\right) \right]\,, \tag{D.0.14b}$$

$$s_z(t) = 1 - \frac{2R^2\left(1-\beta_z^2\right)}{1+2\beta_z R + R^2}\sin^2\left(\frac{\omega}{2}t\right)\,, \tag{D.0.14c}$$

such that the magnitude of the spin along the transverse direction evolves according to

$$\begin{aligned} |s_\perp(t)| &= \sqrt{s_x(t)^2 + s_y(t)^2} \\ &= \frac{2\left|R\sin\left(\frac{\omega}{2}t\right)\right|}{1+2\beta_z R + R^2}\sqrt{1-\beta_z^2}\sqrt{1+2\beta_z R + R^2\left[\cos^2\left(\frac{\omega}{2}t\right) + \beta_z^2\sin^2\left(\frac{\omega}{2}t\right)\right]}\,, \end{aligned} \tag{D.0.15}$$

which vanishes identically when $|\beta_z| = 1$, or equivalently when the DM wind is colinear with the magnetic field. Consequently, the expression equivalent to (D.0.15) for a general magnetic field orientation is found by making the replacement $\beta_z \to \beta_\parallel$, where $\beta_\parallel$ is the fraction of the relative frame velocity along the external magnetic field direction. The corresponding transverse magnetisation is simply

$$|M_\perp(t)| = n_\psi \mu_\psi |s_\perp(t)|\,, \tag{D.0.16}$$

where n_ψ is the number density of SM fermions in the target, and μ_ψ is their magnetic moment. In the case of a perfectly DM exactly perpendicular to $\boldsymbol{B}_{\rm ext}$, that is $\beta_\parallel = 0$,

we have $\omega_0 = \Delta E_B \sqrt{1+R^2}$ and (D.0.15) reduces to (5.4.6). For completeness, we note that (D.0.15) has a maximum of

$$|s_\perp(t_{\max})| = \frac{2|R|\sqrt{1-\beta_\parallel^2}\sqrt{1+\beta_\parallel R+\beta_\parallel^2 R^2}}{1+\beta_\parallel R+R^2} \quad \text{at} \quad t_{\max} = \frac{(2k+1)\pi}{\omega_\psi}\,, \tag{D.0.17}$$

where $k \in \mathbb{N}^0$. This recovers (5.4.7) for $\beta_\parallel = 0$.

Bibliography

[1] M. Bauer and G. Rostagni, *Fifth forces from QCD axions scale differently*, *Phys. Rev. Lett.* **132** (2024) 101802, [2307.09516].

[2] M. Bauer, G. Rostagni and J. Spinner, *Axion-Higgs portal*, *Phys. Rev. D* **107** (2023) 015007, [2207.05762].

[3] G. Rostagni and J. D. Shergold, *The dark Stodolsky effect: constraining effective dark matter operators with spin-dependent interactions*, *JCAP* **07** (2023) 018, [2304.06750].

[4] M. E. Peskin and D. V. Schroeder, *An Introduction to quantum field theory*. Addison-Wesley, Reading, USA, 1995.

[5] M. D. Schwartz, *Quantum Field Theory and the Standard Model*. Cambridge University Press, 3, 2014.

[6] Particle Data Group collaboration, R. L. Workman et al., *Review of Particle Physics*, *PTEP* **2022** (2022) 083C01.

[7] R. V. Harlander, S. Y. Klein and M. Lipp, *FeynGame*, *Comput. Phys. Commun.* **256** (2020) 107465, [2003.00896].

[8] R. Harlander, S. Y. Klein and M. C. Schaaf, *FeynGame-2.1 – Feynman diagrams made easy*, *PoS* **EPS-HEP2023** (2024) 657, [2401.12778].

[9] R. P. Feynman, *Space - time approach to quantum electrodynamics*, *Phys. Rev.* **76** (1949) 769–789.

[10] J. C. Romao and J. P. Silva, *A resource for signs and Feynman diagrams of the Standard Model*, *Int. J. Mod. Phys. A* **27** (2012) 1230025, [1209.6213].

[11] C. Burgard, "Example: Standard model of physics." https://texample.net/tikz/examples/model-physics/. Accessed: 2024-03-14.

[12] Super-Kamiokande collaboration, Y. Fukuda et al., *Evidence for oscillation of atmospheric neutrinos*, *Phys. Rev. Lett.* **81** (1998) 1562–1567, [hep-ex/9807003].

[13] SNO collaboration, Q. R. Ahmad et al., *Direct evidence for neutrino flavor transformation from neutral current interactions in the Sudbury Neutrino Observatory*, *Phys. Rev. Lett.* **89** (2002) 011301, [nucl-ex/0204008].

[14] M. E. Machacek and M. T. Vaughn, *Two Loop Renormalization Group Equations in a General Quantum Field Theory. 1. Wave Function Renormalization*, *Nucl. Phys. B* **222** (1983) 83–103.

[15] M. E. Machacek and M. T. Vaughn, *Two Loop Renormalization Group Equations in a General Quantum Field Theory. 2. Yukawa Couplings*, *Nucl. Phys. B* **236** (1984) 221–232.

[16] M. E. Machacek and M. T. Vaughn, *Two Loop Renormalization Group Equations in a General Quantum Field Theory. 3. Scalar Quartic Couplings*, *Nucl. Phys. B* **249** (1985) 70–92.

[17] M. Bauer, M. Neubert, S. Renner, M. Schnubel and A. Thamm, *The Low-Energy Effective Theory of Axions and ALPs*, *JHEP* **04** (2021) 063, [2012.12272].

[18] B. Pendleton and G. G. Ross, *Mass and Mixing Angle Predictions from Infrared Fixed Points*, *Phys. Lett. B* **98** (1981) 291–294.

[19] C. Abel et al., *Measurement of the Permanent Electric Dipole Moment of the Neutron*, *Phys. Rev. Lett.* **124** (2020) 081803, [2001.11966].

[20] A. Keshavarzi, K. S. Khaw and T. Yoshioka, *Muon g−2: A review*, *Nucl. Phys. B* **975** (2022) 115675, [2106.06723].

[21] CDF collaboration, T. Aaltonen et al., *High-precision measurement of the W boson mass with the CDF II detector*, *Science* **376** (2022) 170–176.

[22] N. Bezginov, T. Valdez, M. Horbatsch, A. Marsman, A. C. Vutha and E. A. Hessels, *A measurement of the atomic hydrogen Lamb shift and the proton charge radius*, *Science* **365** (2019) 1007–1012.

[23] F. Zwicky, *Die Rotverschiebung von extragalaktischen Nebeln*, *Helvetica Physica Acta* **6** (Jan., 1933) 110–127.

[24] V. C. Rubin and W. K. Ford, Jr., *Rotation of the Andromeda Nebula from a Spectroscopic Survey of Emission Regions*, *Astrophys. J.* **159** (1970) 379–403.

[25] M. S. Roberts and A. H. Rots, *Comparison of Rotation Curves of Different Galaxy Types*, *Astronomy and Astrophysics* **26** (Aug., 1973) 483–485.

[26] V. C. Rubin, N. Thonnard and W. K. Ford, Jr., *Rotational properties of 21 SC galaxies with a large range of luminosities and radii, from NGC 4605 /R = 4kpc/ to UGC 2885 /R = 122 kpc/*, *Astrophys. J.* **238** (1980) 471.

[27] M. Persic, P. Salucci and F. Stel, *The Universal rotation curve of spiral galaxies: 1. The Dark matter connection*, *Mon. Not. Roy. Astron. Soc.* **281** (1996) 27, [astro-ph/9506004].

[28] F. Lelli, S. S. McGaugh and J. M. Schombert, *SPARC: Mass Models for 175 Disk Galaxies with Spitzer Photometry and Accurate Rotation Curves*, *Astron. J.* **152** (2016) 157, [1606.09251].

[29] H. Poincaré, *La Voie lactée et la théorie des gaz*, *Bulletin de la société astronomique de France* **20** (1906) 153–165.

[30] G. Bertone and D. Hooper, *History of dark matter*, *Rev. Mod. Phys.* **90** (2018) 045002, [1605.04909].

[31] T. Clifton, P. G. Ferreira, A. Padilla and C. Skordis, *Modified Gravity and Cosmology*, *Phys. Rept.* **513** (2012) 1–189, [1106.2476].

[32] M. Milgrom, *A Modification of the Newtonian dynamics as a possible alternative to the hidden mass hypothesis*, *Astrophys. J.* **270** (1983) 365–370.

[33] D. Clowe, M. Bradac, A. H. Gonzalez, M. Markevitch, S. W. Randall, C. Jones et al., *A direct empirical proof of the existence of dark matter*, *Astrophys. J. Lett.* **648** (2006) L109–L113, [astro-ph/0608407].

[34] LIGO Scientific, Virgo collaboration, B. P. Abbott et al., *Tests of general relativity with GW150914*, *Phys. Rev. Lett.* **116** (2016) 221101, [1602.03841].

[35] S. Boran, S. Desai, E. O. Kahya and R. P. Woodard, *GW170817 Falsifies Dark Matter Emulators*, *Phys. Rev. D* **97** (2018) 041501, [1710.06168].

[36] I. Banik, C. Pittordis, W. Sutherland, B. Famaey, R. Ibata, S. Mieske et al., *Strong constraints on the gravitational law from gaia dr3 wide binaries*, *Monthly Notices of the Royal Astronomical Society* **527** (Nov., 2023) 45734615.

[37] R. Gavazzi, T. Treu, J. D. Rhodes, L. V. Koopmans, A. S. Bolton, S. Burles et al., *The Sloan Lens ACS Survey. 4. The mass density profile of early-type galaxies out to 100 effective radii*, *Astrophys. J.* **667** (2007) 176–190, [astro-ph/0701589].

[38] BOSS collaboration, S. Alam et al., *The clustering of galaxies in the completed SDSS-III Baryon Oscillation Spectroscopic Survey: cosmological analysis of the DR12 galaxy sample*, *Mon. Not. Roy. Astron. Soc.* **470** (2017) 2617–2652, [1607.03155].

[39] DES collaboration, T. M. C. Abbott et al., *Dark Energy Survey Year 3 results: Cosmological constraints from galaxy clustering and weak lensing*, *Phys. Rev. D* **105** (2022) 023520, [2105.13549].

[40] Planck collaboration, N. Aghanim et al., *Planck 2018 results. VI. Cosmological parameters*, *Astron. Astrophys.* **641** (2020) A6, [1807.06209].

[41] B. D. Fields, K. A. Olive, T.-H. Yeh and C. Young, *Big-Bang Nucleosynthesis after Planck*, *JCAP* **03** (2020) 010, [1912.01132].

[42] L. Perivolaropoulos and F. Skara, *Challenges for ΛCDM: An update*, *New Astron. Rev.* **95** (2022) 101659, [2105.05208].

[43] W. J. G. de Blok, *The Core-Cusp Problem*, *Advances in Astronomy* **2010** (Jan., 2010) 789293, [0910.3538].

[44] A. Del Popolo and M. Le Delliou, *Review of Solutions to the Cusp-Core Problem of the ΛCDM Model*, *Galaxies* **9** (2021) 123, [2209.14151].

[45] J. L. Feng, *Dark Matter Candidates from Particle Physics and Methods of Detection*, *Ann. Rev. Astron. Astrophys.* **48** (2010) 495–545, [1003.0904].

[46] L. J. Hall, K. Jedamzik, J. March-Russell and S. M. West, *Freeze-In Production of FIMP Dark Matter*, *JHEP* **03** (2010) 080, [0911.1120].

[47] SuperCDMS collaboration, R. Agnese et al., *Search for Low-Mass Weakly Interacting Massive Particles with SuperCDMS*, *Phys. Rev. Lett.* **112** (2014) 241302, [1402.7137].

[48] SuperCDMS collaboration, S. Zatschler, *Status and prospects of the SuperCDMS Dark Matter experiment at SNOLAB*, *PoS* **TAUP2023** (2024) 076.

[49] XENON collaboration, E. Aprile et al., *First Dark Matter Search with Nuclear Recoils from the XENONnT Experiment*, *Phys. Rev. Lett.* **131** (2023) 041003, [2303.14729].

[50] LZ collaboration, J. Aalbers et al., *First Dark Matter Search Results from the LUX-ZEPLIN (LZ) Experiment*, *Phys. Rev. Lett.* **131** (2023) 041002, [2207.03764].

[51] ADMX collaboration, T. Braine et al., *Extended Search for the Invisible Axion with the Axion Dark Matter Experiment*, *Phys. Rev. Lett.* **124** (2020) 101303, [1910.08638].

[52] ADMX collaboration, C. Bartram et al., *Search for Invisible Axion Dark Matter in the 3.3–4.2 μeV Mass Range*, *Phys. Rev. Lett.* **127** (2021) 261803, [2110.06096].

[53] MADMAX collaboration, P. Brun et al., *A new experimental approach to probe QCD axion dark matter in the mass range above 40 μeV*, *Eur. Phys. J. C* **79** (2019) 186, [1901.07401].

[54] L. Badurina et al., *AION: An Atom Interferometer Observatory and Network*, *JCAP* **05** (2020) 011, [1911.11755].

[55] AEDGE collaboration, Y. A. El-Neaj et al., *AEDGE: Atomic Experiment for Dark Matter and Gravity Exploration in Space*, *EPJ Quant. Technol.* **7** (2020) 6, [1908.00802].

[56] MAGIS-100 collaboration, J. Coleman, *Matter-wave Atomic Gradiometer InterferometricSensor (MAGIS-100) at Fermilab*, *PoS* **ICHEP2018** (2019) 021, [1812.00482].

[57] T. Marrodán Undagoitia and L. Rauch, *Dark matter direct-detection experiments*, *J. Phys. G* **43** (2016) 013001, [1509.08767].

[58] AMS collaboration, M. Aguilar et al., *The Alpha Magnetic Spectrometer (AMS) on the international space station: Part II — Results from the first seven years*, *Phys. Rept.* **894** (2021) 1–116.

[59] M. C. Weisskopf, H. D. Tananbaum, L. P. van Speybroeck and S. L. O'Dell, *Chandra x-ray observatory (cxo):overview*, *Proc. SPIE Int. Soc. Opt. Eng.* **4012** (2000) 2, [astro-ph/0004127].

[60] L. Struder et al., *The European Photon Imaging Camera on XMM-Newton: The pn-CCD camera*, *Astron. Astrophys.* **365** (2001) L18–26.

[61] VERITAS collaboration, S. Archambault et al., *Dark Matter Constraints from a Joint Analysis of Dwarf Spheroidal Galaxy Observations with VERITAS*, *Phys. Rev. D* **95** (2017) 082001, [1703.04937].

[62] MAGIC collaboration, V. A. Acciari et al., *Combined searches for dark matter in dwarf spheroidal galaxies observed with the MAGIC telescopes, including new data from Coma Berenices and Draco*, *Phys. Dark Univ.* **35** (2022) 100912, [2111.15009].

[63] H.E.S.S. collaboration, H. Abdallah et al., *Search for dark matter signals towards a selection of recently detected DES dwarf galaxy satellites of the Milky Way with H.E.S.S.*, *Phys. Rev. D* **102** (2020) 062001, [2008.00688].

[64] WMAP collaboration, G. Hinshaw et al., *Nine-Year Wilkinson Microwave Anisotropy Probe (WMAP) Observations: Cosmological Parameter Results*, *Astrophys. J. Suppl.* **208** (2013) 19, [1212.5226].

[65] F. Beutler, C. Blake, M. Colless, D. H. Jones, L. Staveley-Smith, L. Campbell et al., *The 6dF Galaxy Survey: Baryon Acoustic Oscillations and the Local Hubble Constant*, *Mon. Not. Roy. Astron. Soc.* **416** (2011) 3017–3032, [1106.3366].

[66] P. deNiverville, M. Pospelov and A. Ritz, *Observing a light dark matter beam with neutrino experiments*, *Phys. Rev. D* **84** (2011) 075020, [1107.4580].

[67] P. deNiverville, D. McKeen and A. Ritz, *Signatures of sub-GeV dark matter beams at neutrino experiments*, *Phys. Rev. D* **86** (2012) 035022, [1205.3499].

[68] IceCube collaboration, M. G. Aartsen et al., *Search for dark matter annihilations in the Sun with the 79-string IceCube detector*, *Phys. Rev. Lett.* **110** (2013) 131302, [1212.4097].

[69] Super-Kamiokande collaboration, K. Choi et al., *Search for neutrinos from annihilation of captured low-mass dark matter particles in the Sun by Super-Kamiokande*, *Phys. Rev. Lett.* **114** (2015) 141301, [1503.04858].

[70] J. M. Gaskins, *A review of indirect searches for particle dark matter*, *Contemp. Phys.* **57** (2016) 496–525, [1604.00014].

[71] T. R. Slatyer, *Indirect Detection of Dark Matter*, in *Theoretical Advanced Study Institute in Elementary Particle Physics: Anticipating the Next Discoveries in Particle Physics*, pp. 297–353, 2018, 1710.05137, DOI.

[72] ATLAS collaboration, M. Aaboud et al., *Search for new phenomena in final states with an energetic jet and large missing transverse momentum in pp collisions at $\sqrt{s} = 13$ TeV using the ATLAS detector*, *Phys. Rev. D* **94** (2016) 032005, [1604.07773].

[73] ATLAS collaboration, G. Aad et al., *Search for Heavy Neutral Leptons in Decays of W Bosons Using a Dilepton Displaced Vertex in s=13 TeV pp Collisions with the ATLAS Detector*, *Phys. Rev. Lett.* **131** (2023) 061803, [2204.11988].

[74] CMS collaboration, A. M. Sirunyan et al., *Search for dijet resonances in proton–proton collisions at $\sqrt{s} = 13$ TeV and constraints on dark matter and other models*, *Phys. Lett. B* **769** (2017) 520–542, [1611.03568].

[75] CMS collaboration, A. M. Sirunyan et al., *Search for dark matter produced with an energetic jet or a hadronically decaying W or Z boson at $\sqrt{s} = 13$ TeV*, *JHEP* **07** (2017) 014, [1703.01651].

[76] A. Boveia and C. Doglioni, *Dark Matter Searches at Colliders*, *Ann. Rev. Nucl. Part. Sci.* **68** (2018) 429–459, [1810.12238].

[77] M. Pospelov and A. Ritz, *Theta induced electric dipole moment of the neutron via QCD sum rules*, *Phys. Rev. Lett.* **83** (1999) 2526–2529, [hep-ph/9904483].

[78] K. Fujikawa, *Path Integral Measure for Gauge Invariant Fermion Theories*, *Phys. Rev. Lett.* **42** (1979) 1195–1198.

[79] K. Fujikawa, *Path Integral for Gauge Theories with Fermions*, *Phys. Rev. D* **21** (1980) 2848.

[80] S. L. Adler, *Axial vector vertex in spinor electrodynamics*, *Phys. Rev.* **177** (1969) 2426–2438.

[81] J. S. Bell and R. Jackiw, *A PCAC puzzle: $\pi^0 \to \gamma\gamma$ in the σ model*, *Nuovo Cim. A* **60** (1969) 47–61.

[82] M. Dine, *TASI lectures on the strong CP problem*, in *Theoretical Advanced Study Institute in Elementary Particle Physics (TASI 2000): Flavor Physics for the Millennium*, pp. 349–369, 6, 2000, hep-ph/0011376.

[83] J. E. Kim and G. Carosi, *Axions and the Strong CP Problem*, *Rev. Mod. Phys.* **82** (2010) 557–602, [0807.3125].

[84] A. Hook, *TASI Lectures on the Strong CP Problem and Axions*, *PoS* **TASI2018** (2019) 004, [1812.02669].

[85] J. M. Alarcon, J. Martin Camalich and J. A. Oller, *Improved description of the πN-scattering phenomenology in covariant baryon chiral perturbation theory*, *Annals Phys.* **336** (2013) 413–461, [1210.4450].

[86] C. A. Baker et al., *An Improved experimental limit on the electric dipole moment of the neutron*, *Phys. Rev. Lett.* **97** (2006) 131801, [hep-ex/0602020].

[87] J. M. Pendlebury et al., *Revised experimental upper limit on the electric dipole moment of the neutron*, *Phys. Rev. D* **92** (2015) 092003, [1509.04411].

[88] A. E. Nelson, *Naturally Weak CP Violation*, *Phys. Lett. B* **136** (1984) 387–391.

[89] S. M. Barr, *Solving the Strong CP Problem Without the Peccei-Quinn Symmetry*, *Phys. Rev. Lett.* **53** (1984) 329.

[90] R. D. Peccei and H. R. Quinn, *CP Conservation in the Presence of Instantons*, *Phys. Rev. Lett.* **38** (1977) 1440–1443.

[91] R. D. Peccei and H. R. Quinn, *Constraints Imposed by CP Conservation in the Presence of Instantons*, *Phys. Rev. D* **16** (1977) 1791–1797.

[92] F. Wilczek, *Problem of Strong P and T Invariance in the Presence of Instantons*, *Phys. Rev. Lett.* **40** (1978) 279–282.

[93] S. Weinberg, *A New Light Boson?*, *Phys. Rev. Lett.* **40** (1978) 223–226.

[94] S. Ghigna, M. Lusignoli and M. Roncadelli, *Instability of the invisible axion*, *Phys. Lett. B* **283** (1992) 278–281.

[95] M. Kamionkowski and J. March-Russell, *Planck scale physics and the Peccei-Quinn mechanism*, *Phys. Lett. B* **282** (1992) 137–141, [hep-th/9202003].

[96] R. Holman, S. D. H. Hsu, T. W. Kephart, E. W. Kolb, R. Watkins and L. M. Widrow, *Solutions to the strong CP problem in a world with gravity*, *Phys. Lett. B* **282** (1992) 132–136, [hep-ph/9203206].

[97] S. M. Barr and D. Seckel, *Planck scale corrections to axion models*, *Phys. Rev. D* **46** (1992) 539–549.

[98] T. W. Donnelly, S. J. Freedman, R. S. Lytel, R. D. Peccei and M. Schwartz, *Do Axions Exist?*, *Phys. Rev. D* **18** (1978) 1607.

[99] L. D. Duffy and K. van Bibber, *Axions as Dark Matter Particles*, *New J. Phys.* **11** (2009) 105008, [0904.3346].

[100] J. E. Kim, *Weak Interaction Singlet and Strong CP Invariance*, *Phys. Rev. Lett.* **43** (1979) 103.

[101] M. A. Shifman, A. I. Vainshtein and V. I. Zakharov, *Can Confinement Ensure Natural CP Invariance of Strong Interactions?*, *Nucl. Phys. B* **166** (1980) 493–506.

[102] M. Dine, W. Fischler and M. Srednicki, *A Simple Solution to the Strong CP Problem with a Harmless Axion*, *Phys. Lett. B* **104** (1981) 199–202.

[103] A. R. Zhitnitsky, *On Possible Suppression of the Axion Hadron Interactions. (In Russian)*, *Sov. J. Nucl. Phys.* **31** (1980) 260.

[104] L. Di Luzio, M. Giannotti, E. Nardi and L. Visinelli, *The landscape of QCD axion models*, *Phys. Rept.* **870** (2020) 1–117, [2003.01100].

[105] I. Brivio and M. Trott, *The Standard Model as an Effective Field Theory*, *Phys. Rept.* **793** (2019) 1–98, [1706.08945].

[106] C. N. Leung, S. T. Love and S. Rao, *Low-Energy Manifestations of a New Interaction Scale: Operator Analysis*, *Z. Phys. C* **31** (1986) 433.

[107] W. Buchmuller and D. Wyler, *Effective Lagrangian Analysis of New Interactions and Flavor Conservation*, *Nucl. Phys. B* **268** (1986) 621–653.

[108] B. Grzadkowski, M. Iskrzynski, M. Misiak and J. Rosiek, *Dimension-Six Terms in the Standard Model Lagrangian*, *JHEP* **10** (2010) 085, [1008.4884].

[109] M. Bauer, M. Neubert and A. Thamm, *Collider Probes of Axion-Like Particles*, *JHEP* **12** (2017) 044, [1708.00443].

[110] H. Georgi, D. B. Kaplan and L. Randall, *Manifesting the Invisible Axion at Low-energies*, *Phys. Lett. B* **169** (1986) 73–78.

[111] K. G. Chetyrkin, B. A. Kniehl, M. Steinhauser and W. A. Bardeen, *Effective QCD interactions of CP odd Higgs bosons at three loops*, *Nucl. Phys. B* **535** (1998) 3–18, [hep-ph/9807241].

[112] W. A. Bardeen, S. H. H. Tye and J. A. M. Vermaseren, *Phenomenology of the New Light Higgs Boson Search*, *Phys. Lett. B* **76** (1978) 580–584.

[113] P. Di Vecchia and G. Veneziano, *Chiral Dynamics in the Large n Limit*, *Nucl. Phys. B* **171** (1980) 253–272.

[114] M. Bauer, M. Neubert, S. Renner, M. Schnubel and A. Thamm, *Flavor probes of axion-like particles*, *JHEP* **09** (2022) 056, [2110.10698].

[115] J. Liang, Y.-B. Yang, T. Draper, M. Gong and K.-F. Liu, *Quark spins and Anomalous Ward Identity*, *Phys. Rev. D* **98** (2018) 074505, [1806.08366].

[116] Flavour Lattice Averaging Group collaboration, S. Aoki et al., *FLAG Review 2019: Flavour Lattice Averaging Group (FLAG)*, *Eur. Phys. J. C* **80** (2020) 113, [1902.08191].

[117] M. Ghosh, Y. Grossman, W. Tangarife, X.-J. Xu and B. Yu, *Neutrino forces in neutrino backgrounds*, 2209.07082.

[118] D. Blas, I. Esteban, M. C. Gonzalez-Garcia and J. Salvado, *On neutrino-mediated potentials in a neutrino background*, 2212.03889.

[119] S. Barbosa and S. Fichet, *Background-Induced Forces from Dark Relics*, 2403.13894.

[120] R. B. Wiringa, V. G. J. Stoks and R. Schiavilla, *An Accurate nucleon-nucleon potential with charge independence breaking*, *Phys. Rev. C* **51** (1995) 38–51, [nucl-th/9408016].

[121] B. A. Dobrescu and I. Mocioiu, *Spin-dependent macroscopic forces from new particle exchange*, *JHEP* **11** (2006) 005, [hep-ph/0605342].

[122] G. Feinberg and J. Sucher, *Long-range electromagnetic forces on neutral particles*, *Phys. Rev.* **139** (Sep, 1965) B1619–B1633.

[123] G. Feinberg, J. Sucher and C. K. Au, *The Dispersion Theory of Dispersion Forces*, *Phys. Rept.* **180** (1989) 83.

[124] S. Fichet, *Quantum Forces from Dark Matter and Where to Find Them*, *Phys. Rev. Lett.* **120** (2018) 131801, [1705.10331].

[125] P. Brax, S. Fichet and G. Pignol, *Bounding Quantum Dark Forces*, *Phys. Rev. D* **97** (2018) 115034, [1710.00850].

[126] A. Costantino, S. Fichet and P. Tanedo, *Exotic Spin-Dependent Forces from a Hidden Sector*, *JHEP* **03** (2020) 148, [1910.02972].

[127] H. Banks and M. Mccullough, *Charting the Fifth Force Landscape*, *Phys. Rev. D* **103** (2021) 075018, [2009.12399].

[128] R. E. Cutkosky, *Singularities and discontinuities of Feynman amplitudes*, *J. Math. Phys.* **1** (1960) 429–433.

[129] W. Beenakker, H. Kuijf, W. L. van Neerven and J. Smith, *QCD Corrections to Heavy Quark Production in p anti-p Collisions*, *Phys. Rev. D* **40** (1989) 54–82.

[130] G. Passarino and M. J. G. Veltman, *One Loop Corrections for e+ e- Annihilation Into mu+ mu- in the Weinberg Model*, *Nucl. Phys. B* **160** (1979) 151–207.

[131] "*NIST Digital Library of Mathematical Functions*." https://dlmf.nist.gov/, Release 1.1.12 of 2023-12-15. F. W. J. Olver, A. B. Olde Daalhuis, D. W. Lozier, B. I. Schneider, R. F. Boisvert, C. W. Clark, B. R. Miller, B. V. Saunders, H. S. Cohl, and M. A. McClain, eds.

[132] G. Feinberg and J. Sucher, *Long-Range Forces from Neutrino-Pair Exchange*, *Phys. Rev.* **166** (1968) 1638–1644.

[133] S. D. H. Hsu and P. Sikivie, *Long range forces from two neutrino exchange revisited*, *Phys. Rev. D* **49** (1994) 4951–4953, [hep-ph/9211301].

[134] A. Costantino and S. Fichet, *The Neutrino Casimir Force*, *JHEP* **09** (2020) 122, [2003.11032].

[135] J. E. Moody and F. Wilczek, *NEW MACROSCOPIC FORCES?*, *Phys. Rev. D* **30** (1984) 130.

[136] J. A. Grifols and S. Tortosa, *Residual long range pseudoscalar forces between unpolarized macroscopic bodies*, *Phys. Lett. B* **328** (1994) 98–102, [hep-ph/9404249].

[137] F. Ferrer, J. A. Grifols and M. Nowakowski, *Long range forces induced by neutrinos at finite temperature*, *Phys. Lett. B* **446** (1999) 111–116, [hep-ph/9806438].

[138] F. Ferrer and M. Nowakowski, *Higgs and Goldstone bosons mediated long range forces*, *Phys. Rev. D* **59** (1999) 075009, [hep-ph/9810550].

[139] F. J. Dyson, *The interactions of nucleons with meson fields*, *Phys. Rev.* **73** (Apr, 1948) 929–930.

[140] J. V. Lepore, *Symmetrical pseudoscalar meson theory of nuclear forces*, *Phys. Rev.* **88** (Nov, 1952) 750–751.

[141] S. D. Drell and E. M. Henley, *Pseudoscalar mesons with applications to meson-nucleon scattering and photoproduction*, *Phys. Rev.* **88** (Dec, 1952) 1053–1064.

[142] S. D. Drell and K. Huang, *Many-body forces and nuclear saturation*, *Phys. Rev.* **91** (Sep, 1953) 1527–1542.

[143] F. Ferrer and J. A. Grifols, *Long range forces from pseudoscalar exchange*, *Phys. Rev. D* **58** (1998) 096006, [hep-ph/9805477].

[144] J. Gasser, M. E. Sainio and A. Svarc, *Nucleons with chiral loops*, *Nucl. Phys. B* **307** (1988) 779–853.

[145] M. Gell-Mann, R. J. Oakes and B. Renner, *Behavior of current divergences under SU(3) x SU(3)*, *Phys. Rev.* **175** (1968) 2195–2199.

[146] C. Vafa and E. Witten, *Parity Conservation in QCD*, *Phys. Rev. Lett.* **53** (1984) 535.

[147] A. Hook and J. Huang, *Probing axions with neutron star inspirals and other stellar processes*, *JHEP* **06** (2018) 036, [1708.08464].

[148] R. Balkin, J. Serra, K. Springmann and A. Weiler, *The QCD axion at finite density*, *JHEP* **07** (2020) 221, [2003.04903].

[149] D. Chang, R. N. Mohapatra and S. Nussinov, *COULD GOLDSTONE BOSONS GENERATE AN OBSERVABLE 1/R POTENTIAL?*, *Phys. Rev. Lett.* **55** (1985) 2835.

[150] H. E. Haber and M. Sher, *AXION MEDIATED FORCES IN THE EARLY UNIVERSE*, *Phys. Lett. B* **196** (1987) 33–38.

[151] S. Mantry, M. Pitschmann and M. J. Ramsey-Musolf, *Differences between Axions and Generic Light Scalars in Laboratory Experiments*, in *10th Patras Workshop on Axions, WIMPs and WISPs*, pp. 102–107, 2014, 1411.2162, DOI.

[152] H. Fukuda and S. Shirai, *Detection of QCD axion dark matter by coherent scattering*, *Phys. Rev. D* **105** (2022) 095030, [2112.13536].

[153] E. G. Adelberger, B. R. Heckel, S. A. Hoedl, C. D. Hoyle, D. J. Kapner and A. Upadhye, *Particle Physics Implications of a Recent Test of the Gravitational Inverse Sqaure Law*, *Phys. Rev. Lett.* **98** (2007) 131104, [hep-ph/0611223].

[154] M. S. Safronova, D. Budker, D. DeMille, D. F. J. Kimball, A. Derevianko and C. W. Clark, *Search for New Physics with Atoms and Molecules*, *Rev. Mod. Phys.* **90** (2018) 025008, [1710.01833].

[155] H. C. Chiu, G. L. Klimchitskaya, V. N. Marachevsky, V. M. Mostepanenko and U. Mohideen, *Lateral Casimir force between sinusoidally corrugated surfaces: Asymmetric profiles, deviations from the proximity force approximation and comparison with exact theory*, *Phys. Rev. B* **81** (2010) 115417, [1002.3936].

[156] V. B. Bezerra, G. L. Klimchitskaya, V. M. Mostepanenko and C. Romero, *Constraining axion-nucleon coupling constants from measurements of effective Casimir pressure by means of micromachined oscillator*, *Eur. Phys. J. C* **74** (2014) 2859, [1402.3228].

[157] Y. J. Chen, W. K. Tham, D. E. Krause, D. Lopez, E. Fischbach and R. S. Decca, *Stronger Limits on Hypothetical Yukawa Interactions in the 30–8000 nm Range*, *Phys. Rev. Lett.* **116** (2016) 221102, [1410.7267].

[158] G. L. Klimchitskaya and V. M. Mostepanenko, *Improved constraints on the coupling constants of axion-like particles to nucleons from recent Casimir-less experiment*, *Eur. Phys. J. C* **75** (2015) 164, [1503.04982].

[159] G. L. Klimchitskaya and V. M. Mostepanenko, *Dark Matter Axions, Non-Newtonian Gravity and Constraints on Them from Recent Measurements of the Casimir Force in the Micrometer Separation Range*, *Universe* **7** (2021) 343, [2109.06534].

[160] S. Weinberg, *Goldstone Bosons as Fractional Cosmic Neutrinos*, *Phys. Rev. Lett.* **110** (2013) 241301, [1305.1971].

[161] C. P. Burgess, M. Pospelov and T. ter Veldhuis, *The Minimal model of nonbaryonic dark matter: A Singlet scalar*, *Nucl. Phys. B* **619** (2001) 709–728, [hep-ph/0011335].

[162] S. Dawson, P. P. Giardino and S. Homiller, *Uncovering the High Scale Higgs Singlet Model*, *Phys. Rev. D* **103** (2021) 075016, [2102.02823].

[163] ATLAS collaboration, G. Aad et al., *Combined measurements of Higgs boson production and decay using up to* 80 fb^{-1} *of proton-proton collision data at* $\sqrt{s}$ *= 13 TeV collected with the ATLAS experiment*, *Phys. Rev. D* **101** (2020) 012002, [1909.02845].

[164] CMS collaboration, *Combined Higgs boson production and decay measurements with up to 137* fb^{-1} *of proton-proton collision data at* $\sqrt{s}$ *= 13 TeV*, .

[165] M. Gonderinger, H. Lim and M. J. Ramsey-Musolf, *Complex Scalar Singlet Dark Matter: Vacuum Stability and Phenomenology*, *Phys. Rev. D* **86** (2012) 043511, [1202.1316].

[166] B. A. Kniehl and M. Spira, *Low-energy theorems in Higgs physics*, *Z. Phys. C* **69** (1995) 77–88, [hep-ph/9505225].

[167] B. Grzadkowski and P. Krawczyk, *HIGGS PARTICLE EFFECTS IN FLAVOR CHANGING TRANSITIONS*, *Z. Phys. C* **18** (1983) 43–45.

[168] A. Dedes, *The Higgs penguin and its applications: An Overview*, *Mod. Phys. Lett. A* **18** (2003) 2627–2644, [hep-ph/0309233].

[169] A. Kachanovich, U. Nierste and I. Nišandžić, *Higgs portal to dark matter and* $B \to K^{(*)}$ *decays*, *Eur. Phys. J. C* **80** (2020) 669, [2003.01788].

[170] M. Bauer, M. Neubert, S. Renner, M. Schnubel and A. Thamm, *Consistent Treatment of Axions in the Weak Chiral Lagrangian*, *Phys. Rev. Lett.* **127** (2021) 081803, [2102.13112].

[171] M. A. Shifman, A. I. Vainshtein and V. I. Zakharov, *Remarks on Higgs Boson Interactions with Nucleons*, *Phys. Lett. B* **78** (1978) 443–446.

[172] J. M. Alarcon, J. Martin Camalich and J. A. Oller, *The chiral representation of the πN scattering amplitude and the pion-nucleon sigma term*, *Phys. Rev. D* **85** (2012) 051503, [1110.3797].

[173] A. Crivellin, M. Hoferichter and M. Procura, *Accurate evaluation of hadronic uncertainties in spin-independent WIMP-nucleon scattering: Disentangling two- and three-flavor effects*, *Phys. Rev. D* **89** (2014) 054021, [1312.4951].

[174] M. Hoferichter, J. Ruiz de Elvira, B. Kubis and U.-G. Meißner, *High-Precision Determination of the Pion-Nucleon σ Term from Roy-Steiner Equations*, *Phys. Rev. Lett.* **115** (2015) 092301, [1506.04142].

[175] G. Arcadi, A. Djouadi and M. Raidal, *Dark Matter through the Higgs portal*, *Phys. Rept.* **842** (2020) 1–180, [1903.03616].

[176] J. Jaeckel and M. Spannowsky, *Probing MeV to 90 GeV axion-like particles with LEP and LHC*, *Phys. Lett. B* **753** (2016) 482–487, [1509.00476].

[177] G. Alonso-Álvarez, M. B. Gavela and P. Quilez, *Axion couplings to electroweak gauge bosons*, *Eur. Phys. J. C* **79** (2019) 223, [1811.05466].

[178] J. Redondo and A. Ringwald, *Light shining through walls*, *Contemp. Phys.* **52** (2011) 211–236, [1011.3741].

[179] OSQAR collaboration, R. Ballou et al., *New exclusion limits on scalar and pseudoscalar axionlike particles from light shining through a wall*, *Phys. Rev. D* **92** (2015) 092002, [1506.08082].

[180] C. Hagmann, P. Sikivie, N. Sullivan, D. B. Tanner and S. I. Cho, *Cavity Design for a Cosmic Axion Detector*, *Rev. Sci. Instrum.* **61** (1990) 1076–1085.

[181] G. G. Raffelt, *Astrophysical axion bounds*, *Lect. Notes Phys.* **741** (2008) 51–71, [hep-ph/0611350].

[182] ATLAS collaboration, G. Aad et al., *Search for invisible Higgs-boson decays in events with vector-boson fusion signatures using 139 fb^{-1} of proton-proton data recorded by the ATLAS experiment*, *JHEP* **08** (2022) 104, [2202.07953].

[183] CMS collaboration, A. Tumasyan et al., *Search for invisible decays of the Higgs boson produced via vector boson fusion in proton-proton collisions at s=13 TeV*, *Phys. Rev. D* **105** (2022) 092007, [2201.11585].

[184] ATLAS collaboration, G. Aad et al., *A detailed map of Higgs boson interactions by the ATLAS experiment ten years after the discovery*, *Nature* **607** (2022) 52–59, [2207.00092].

[185] CMS collaboration, A. Tumasyan et al., *A portrait of the Higgs boson by the CMS experiment ten years after the discovery.*, *Nature* **607** (2022) 60–68, [2207.00043].

[186] M. Cepeda et al., *Report from Working Group 2: Higgs Physics at the HL-LHC and HE-LHC*, *CERN Yellow Rep. Monogr.* **7** (2019) 221–584, [1902.00134].

[187] ILC collaboration, *The International Linear Collider Technical Design Report - Volume 2: Physics*, 1306.6352.

[188] FCC collaboration, A. Abada et al., *FCC-hh: The Hadron Collider: Future Circular Collider Conceptual Design Report Volume 3*, *Eur. Phys. J. ST* **228** (2019) 755–1107.

[189] E. Goudzovski et al., *New physics searches at kaon and hyperon factories*, *Rept. Prog. Phys.* **86** (2023) 016201, [2201.07805].

[190] BaBar collaboration, J. P. Lees et al., *Improved Limits on B^0 Decays to Invisible Final States and to $\nu\bar{\nu}\gamma$*, *Phys. Rev. D* **86** (2012) 051105, [1206.2543].

[191] TUMQCD, Fermilab Lattice, MILC collaboration, A. Bazavov et al., *B- and D-meson leptonic decay constants and quark masses from four-flavor lattice QCD*, in *13th Conference on the Intersections of Particle and Nuclear Physics*, 9, 2018, 1810.00250.

[192] NA62 collaboration, E. Cortina Gil et al., *Search for π^0 decays to invisible particles*, *JHEP* **02** (2021) 201, [2010.07644].

[193] NA62 collaboration, E. Cortina Gil et al., *Measurement of the very rare $K^+ \to \pi^+ \nu\bar{\nu}$ decay*, *JHEP* **06** (2021) 093, [2103.15389].

[194] BaBar collaboration, J. P. Lees et al., *Search for $B \to K^{(*)} \nu\bar{\nu}$ and invisible quarkonium decays*, *Phys. Rev. D* **87** (2013) 112005, [1303.7465].

[195] Belle collaboration, J. Grygier et al., *Search for $\boldsymbol{B \to h\nu\bar{\nu}}$ decays with semileptonic tagging at Belle*, *Phys. Rev. D* **96** (2017) 091101, [1702.03224].

[196] Belle collaboration, I. S. Seong et al., *Search for a light CP-odd Higgs boson and low-mass dark matter at the Belle experiment*, *Phys. Rev. Lett.* **122** (2019) 011801, [1809.05222].

[197] F. Wilczek, *Decays of Heavy Vector Mesons Into Higgs Particles*, *Phys. Rev. Lett.* **39** (1977) 1304.

[198] P. Nason, *QCD Radiative Corrections to Υ Decay Into Scalar Plus γ and Pseudoscalar Plus γ*, *Phys. Lett. B* **175** (1986) 223–226.

[199] BESIII collaboration, K. Liu, *Search for invisible decays at BESIII*, *PoS* **PANIC2021** (2022) 437.

[200] M. Bauer, P. Foldenauer, P. Reimitz and T. Plehn, *Light Dark Matter Annihilation and Scattering in LHC Detectors*, *SciPost Phys.* **10** (2021) 030, [2005.13551].

[201] M. P. A. Jones, R. M. Potvliege and M. Spannowsky, *Probing new physics using Rydberg states of atomic hydrogen*, *Phys. Rev. Res.* **2** (2020) 013244, [1909.09194].

[202] D. J. Griffiths and D. F. Schroeter, *Introduction to quantum mechanics*. Cambridge University Press, Cambridge ; New York, NY, third edition ed., 2018.

[203] V. A. Yerokhin, K. Pachucki and V. Patkos, *Theory of the Lamb Shift in Hydrogen and Light Hydrogen-Like Ions*, *Annalen Phys.* **531** (2019) 1800324, [1809.00462].

[204] E. Tiesinga, P. J. Mohr, D. B. Newell and B. N. Taylor, *CODATA recommended values of the fundamental physical constants: 2018**, *Rev. Mod. Phys.* **93** (2021) 025010.

[205] M. Endo, K. Hamaguchi and G. Mishima, *Constraints on Hidden Photon Models from Electron g-2 and Hydrogen Spectroscopy*, *Phys. Rev. D* **86** (2012) 095029, [1209.2558].

[206] X.-j. Xu and B. Yu, *On the short-range behavior of neutrino forces beyond the Standard Model: from $1/r^5$ to $1/r^4$, $1/r^2$, and $1/r$*, *JHEP* **02** (2022) 008, [2112.03060].

[207] V. A. Dzuba, V. V. Flambaum, P. Munro-Laylim and Y. V. Stadnik, *Probing Long-Range Neutrino-Mediated Forces with Atomic and Nuclear Spectroscopy*, *Phys. Rev. Lett.* **120** (2018) 223202, [1711.03700].

[208] U. Jentschura, S. Kotochigova, E. LeBigot, P. Mohr and B. Taylor, *The energy levels of hydrogen and deuterium*, .

[209] G. W. F. Drake and R. A. Swainson, *Bethe logarithms for hydrogen up to n=20, and approximations for two-electron atoms*, *Phys. Rev. A* **41** (1990) 1243–1246.

[210] A. Kramida, Y. Ralchenko, J. Reader and N. A. Team, *NIST atomic spectra database*, .

[211] W. Greiner, *Relativistic Quantum Mechanics. Wave Equations*. Springer, 2000.

[212] M. Ruhdorfer, E. Salvioni and A. Weiler, *A Global View of the Off-Shell Higgs Portal*, *SciPost Phys.* **8** (2020) 027, [1910.04170].

[213] S. Argyropoulos, O. Brandt and U. Haisch, *Collider Searches for Dark Matter through the Higgs Lens*, *Symmetry* **13** (2021) 2406, [2109.13597].

[214] U. Haisch, G. Polesello and S. Schulte, *Searching for pseudo Nambu-Goldstone boson dark matter production in association with top quarks*, *JHEP* **09** (2021) 206, [2107.12389].

[215] S. Liem, G. Bertone, F. Calore, R. Ruiz de Austri, T. M. P. Tait, R. Trotta et al., *Effective field theory of dark matter: a global analysis*, *JHEP* **09** (2016) 077, [1603.05994].

[216] U. Banerjee, J. Chakrabortty, S. Prakash, S. U. Rahaman and M. Spannowsky, *Effective Operator Bases for Beyond Standard Model Scenarios: An EFT compendium for discoveries*, *JHEP* **01** (2021) 028, [2008.11512].

[217] J. C. Criado, A. Djouadi, M. Perez-Victoria and J. Santiago, *A complete effective field theory for dark matter*, *JHEP* **07** (2021) 081, [2104.14443].

[218] J. Aebischer, W. Altmannshofer, E. E. Jenkins and A. V. Manohar, *Dark matter effective field theory and an application to vector dark matter*, *JHEP* **06** (2022) 086, [2202.06968].

[219] L. Stodolsky, *Speculations on Detection of the Neutrino Sea*, *Phys. Rev. Lett.* **34** (1975) 110.

[220] M. Bauer and J. D. Shergold, *Limits on the cosmic neutrino background*, 2207.12413.

[221] A. J. Long, C. Lunardini and E. Sabancilar, *Detecting non-relativistic cosmic neutrinos by capture on tritium: phenomenology and physics potential*, *JCAP* **08** (2014) 038, [1405.7654].

[222] K. Petraki and R. R. Volkas, *Review of asymmetric dark matter*, *Int. J. Mod. Phys. A* **28** (2013) 1330028, [1305.4939].

[223] A. Arvanitaki and S. Dimopoulos, *The Cosmic Neutrino Background on the Surface of the Earth*, 2212.00036.

[224] G. Baym and J.-C. Peng, *Evolution of primordial neutrino helicities in cosmic gravitational inhomogeneities*, *Phys. Rev. D* **103** (2021) 123019, [2103.11209].

[225] G. Duda, G. Gelmini and S. Nussinov, *Expected signals in relic neutrino detectors*, *Phys. Rev. D* **64** (2001) 122001, [hep-ph/0107027].

[226] V. Domcke and M. Spinrath, *Detection prospects for the Cosmic Neutrino Background using laser interferometers*, *JCAP* **06** (2017) 055, [1703.08629].

[227] A. Y. Smirnov and X.-J. Xu, *Neutrino bound states and bound systems*, *JHEP* **08** (2022) 170, [2201.00939].

[228] R. Ding and Y. Liao, *Spin 3/2 Particle as a Dark Matter Candidate: an Effective Field Theory Approach*, *JHEP* **04** (2012) 054, [1201.0506].

[229] X.-G. He, X.-D. Ma and G. Valencia, *FCNC B and K meson decays with light bosonic Dark Matter*, *JHEP* **03** (2023) 037, [2209.05223].

[230] C. Boehm and P. Fayet, *Scalar dark matter candidates*, *Nucl. Phys. B* **683** (2004) 219–263, [hep-ph/0305261].

[231] C. Boehm, X. Chu, J.-L. Kuo and J. Pradler, *Scalar dark matter candidates revisited*, *Phys. Rev. D* **103** (2021) 075005, [2010.02954].

[232] S. Dodelson and L. M. Widrow, *Sterile-neutrinos as dark matter*, *Phys. Rev. Lett.* **72** (1994) 17–20, [hep-ph/9303287].

[233] A. Kusenko, *Sterile neutrinos, dark matter, and the pulsar velocities in models with a Higgs singlet*, *Phys. Rev. Lett.* **97** (2006) 241301, [hep-ph/0609081].

[234] K. Petraki and A. Kusenko, *Dark-matter sterile neutrinos in models with a gauge singlet in the Higgs sector*, *Phys. Rev. D* **77** (2008) 065014, [0711.4646].

[235] K. N. Abazajian et al., *Light Sterile Neutrinos: A White Paper*, 1204.5379.

[236] G. Jungman, M. Kamionkowski and K. Griest, *Supersymmetric dark matter*, *Phys. Rept.* **267** (1996) 195–373, [hep-ph/9506380].

[237] P. Langacker, *The Physics of Heavy Z' Gauge Bosons*, *Rev. Mod. Phys.* **81** (2009) 1199–1228, [0801.1345].

[238] M. Bauer, P. Foldenauer and J. Jaeckel, *Hunting All the Hidden Photons*, *JHEP* **07** (2018) 094, [1803.05466].

[239] M. Fabbrichesi, E. Gabrielli and G. Lanfranchi, *The Dark Photon*, 2005.01515.

[240] A. Caputo, A. J. Millar, C. A. J. O'Hare and E. Vitagliano, *Dark photon limits: A handbook*, *Phys. Rev. D* **104** (2021) 095029, [2105.04565].

[241] G. Servant and T. M. P. Tait, *Is the lightest Kaluza-Klein particle a viable dark matter candidate?*, *Nucl. Phys. B* **650** (2003) 391–419, [hep-ph/0206071].

[242] H.-C. Cheng, J. L. Feng and K. T. Matchev, *Kaluza-Klein dark matter*, *Phys. Rev. Lett.* **89** (2002) 211301, [hep-ph/0207125].

[243] R. Garani, M. Redi and A. Tesi, *Dark QCD matters*, *JHEP* **12** (2021) 139, [2105.03429].

[244] W. Rarita and J. Schwinger, *On a theory of particles with half integral spin*, *Phys. Rev.* **60** (1941) 61.

[245] M. Kirchbach and D. V. Ahluwalia, *A Critique on the supplementary conditions of Rarita-Schwinger framework*, hep-th/0108030.

[246] P. Böer, M. Bordone, E. Graverini, P. Owen, M. Rotondo and D. Van Dyk, *Testing lepton flavour universality in semileptonic $\Lambda_b \to \Lambda_c^*$ decays*, *JHEP* **06** (2018) 155, [1801.08367].

[247] A. K. Das and D. Z. Freedman, *Gauge Quantization for Spin 3/2 Fields*, *Nucl. Phys. B* **114** (1976) 271–296.

[248] R. Casalbuoni, S. De Curtis, D. Dominici, F. Feruglio and R. Gatto, *A GRAVITINO - GOLDSTINO HIGH-ENERGY EQUIVALENCE THEOREM*, *Phys. Lett. B* **215** (1988) 313–316.

[249] R. Casalbuoni, S. De Curtis, D. Dominici, F. Feruglio and R. Gatto, *High-Energy Equivalence Theorem in Spontaneously Broken Supergravity*, *Phys. Rev. D* **39** (1989) 2281.

[250] A. L. Maroto and J. R. Pelaez, *The Equivalence theorem and the production of gravitinos after inflation*, *Phys. Rev. D* **62** (2000) 023518, [hep-ph/9912212].

[251] M. A. G. Garcia, Y. Mambrini, K. A. Olive and S. Verner, *Case for decaying spin- 3/2 dark matter*, *Phys. Rev. D* **102** (2020) 083533, [2006.03325].

[252] O. Antipin, M. Redi, A. Strumia and E. Vigiani, *Accidental Composite Dark Matter*, *JHEP* **07** (2015) 039, [1503.08749].

[253] T. A. Wagner, S. Schlamminger, J. H. Gundlach and E. G. Adelberger, *Torsion-balance tests of the weak equivalence principle*, *Class. Quant. Grav.* **29** (2012) 184002, [1207.2442].

[254] L.-S. Hou and W.-T. Ni, *Rotatable-Torsion Equivalence Principle Experiment for the Spin-Polarized HoFe3*, *Modern Physics Letters A* **16** (Apr., 2001) 763–773, [physics/0009013].

[255] B. R. Heckel, E. G. Adelberger, C. E. Cramer, T. S. Cook, S. Schlamminger and U. Schmidt, *Preferred-Frame and CP-Violation Tests with Polarized Electrons*, *Phys. Rev. D* **78** (2008) 092006, [0808.2673].

[256] J. I. Read, *The Local Dark Matter Density*, *J. Phys. G* **41** (2014) 063101, [1404.1938].

[257] C. Hagmann, *Cosmic neutrinos and their detection*, in *American Physical Society (APS) Meeting of the Division of Particles and Fields (DPF 99)*, 1, 1999, astro-ph/9905258.

[258] P. W. Graham and S. Rajendran, *New Observables for Direct Detection of Axion Dark Matter*, *Phys. Rev. D* **88** (2013) 035023, [1306.6088].

[259] D. Budker, P. W. Graham, M. Ledbetter, S. Rajendran and A. Sushkov, *Proposal for a Cosmic Axion Spin Precession Experiment (CASPEr)*, *Phys. Rev. X* **4** (2014) 021030, [1306.6089].

[260] S. K. Lamoreaux, *Solid state systems for electron electric dipole moment and other fundamental measurements*, *Phys. Rev. A* **66** (2002) 022109, [nucl-ex/0109014].

[261] VERA collaboration, T. Hirota et al., *The first VERA astrometry catalog*, *Publ. Astron. Soc. Jpn.* **72** (2020) 50, [2002.03089].

[262] T. Fischer, S. Chakraborty, M. Giannotti, A. Mirizzi, A. Payez and A. Ringwald, *Probing axions with the neutrino signal from the next galactic supernova*, *Phys. Rev. D* **94** (2016) 085012, [1605.08780].

[263] SENSEI collaboration, L. Barak et al., *SENSEI: Direct-Detection Results on sub-GeV Dark Matter from a New Skipper-CCD*, *Phys. Rev. Lett.* **125** (2020) 171802, [2004.11378].

[264] R. Essig, T. Volansky and T.-T. Yu, *New Constraints and Prospects for sub-GeV Dark Matter Scattering off Electrons in Xenon*, *Phys. Rev. D* **96** (2017) 043017, [1703.00910].

[265] XENON collaboration, E. Aprile et al., *Light Dark Matter Search with Ionization Signals in XENON1T*, *Phys. Rev. Lett.* **123** (2019) 251801, [1907.11485].

[266] M. Bauer, S. Chakraborti and G. Rostagni, "Axion bounds from quantum technology." Manuscript in preparation.

[267] A. Garcon et al., *Constraints on bosonic dark matter from ultralow-field nuclear magnetic resonance*, *Sci. Adv.* **5** (2019) eaax4539, [1902.04644].

[268] A. Bandyopadhyay and D. Majumdar, *On Diurnal and Annual Variations of Directional Detection Rates of Dark Matter*, *Astrophys. J.* **746** (2012) 107, [1006.3231].